UNDERSTANDING THE STAR-FORMING ENVIRONMENT IN STELLAR CLUSTERS

BY

SHIYA WANG

B.S., National Tsing-Hua University, 2000
M.S., National Tsing-Hua University, 2002

DISSERTATION

Submitted in partial fulfillment of the requirements
for the degree of Doctor of Philosophy in Astronomy
in the Graduate College of the
University of Illinois at Urbana-Champaign, 2008

Urbana, Illinois

Doctoral Committee:

Assistant Professor Leslie W. Looney, Chair
Professor You-Hua Chu
Professor Richard M. Crutcher
Associate Professor Brian Fields

Abstract

The main goal of this thesis is to investigate the physical conditions of the star-forming environment in stellar clusters, especially for the formation of low-mass cluster members. Embedded, young, and intermediate-mass stellar clusters around Herbig Ae/Be stars are sampled. Mid- and near-infrared observations identifying young stars and millimeter interferometric observations probing dense molecular gas and dust continuum are presented. These observations are used to reveal the large-scale young stellar population around the vicinity where the sampled clusters form, probe the physical conditions of dense molecular clumps which are capable of forming individual low-mass cluster members, and examine the influence of the most massive star in the cluster on its siblings and natal cluster-forming cloud. This study shows that stars within the cluster tend to seem younger than those outside the cluster, suggesting a higher and continuous star-forming rate within the cluster than outside, or massive stars are initiated later than low-mass stars within the same cloud. A thorough investigation of young stars and dense gas toward the MWC 1080 cluster further suggests a domination of the most massive star in the cluster on both the natal cloud dispersal and its low-mass cluster members. As active outflows and winds from the Herbig Ae/Be stars increase the non-thermal motion in the cloud, low-mass cluster members are formed within denser and more turbulent cores, than isolated low-mass star-forming cores. In addition, the strong gas dispersal from the Herbig Ae/Be stars also helps the removal of the circumstellar material around nearby low-mass stars. This makes these low-mass cluster members appear older. In summary, this thesis provides the observational evidence showing how the most massive star in the cluster affects the formation and evolution of low-mass cluster members and the physical conditions of star formation in the cluster.

Acknowledgments

I would not have finished this thesis without the help and support of many people. First of all, I would like to thank my advisor, Leslie Looney, for his advice, patience, encouragement, and all the valuable discussion. I especially appreciate his patience to listen to and always try to understand my thoughts and ideas all these years. I also appreciate him for always giving me enough time to finish my work, without giving me any pressure, and allowing me to work at home all the time. He once said that I have to lead my own way, which I think is a very important guidance for a PhD student learning to become a scientist. His way of advising students has been very helpful to me, and I appreciate that very much.

There are several professors I would like to thank: You-Hua Chu for being my thesis committee, writing job recommendation letters for me, giving me a lot of advice all these years, and being every Taiwanese student's Mom here; John Dickel for being my first-year's advisor and also very kind and patience to me, especially when I just arrived in the US at that time; Dick Crutcher for being my thesis committee who gave many valuable scientific suggestions, and writing job recommendation letters for me; and Brian Fields for being my thesis committee and a very supportive graduate student advisor during my first three years here.

I would also like to thank my collaborators, Murad Hamidouche, Wolfgang Brandner, Randolf Klein, and Laird Close, for their help with my papers and various observing proposals. I also want to thank Martin Guerrero for teaching me Chandra Xray data reduction and analysis and Robert Gruendl for Infrared data reduction and analysis. I would especially like to thank Rosie Chen, who has been a big sister and great friend to me and helped me with everything in science and life.

And a big thank you to the Astronomy Department staff: Jeri Cochran, Sandie Osterbur, Mary Margaret O'Connor, Bryan Dunne, and Kevin Pointer, with their help on everything. Also to all my classmates: Scott, Shweta, Jerry, Po Kin, Amit, Zarija, Xiaoyue, and Modhurita.

To all my friends, especially the "original Friday shopping group"– Rosie, Tai-Lin, Shu-Ning, and Sen-Lin, and many other dear friends I met here all these years. And to my best friends, Zara, Bobola, and Sophie, who have been there for me. I also want to thank my cousin James who looked out for me during my first years here.

Finally, to my family– Mom, Dad, Shijin, and Shihyao, for your love and support. And grandpa and grandma, who will always be with me.

Table of Contents

Chapter 1

Introduction

The main thrust of this thesis is to investigate the physical conditions of the star-forming environment in young embedded stellar clusters with infrared and millimeter interferometric observations. Infrared observations reveal the dust morphology and the circumstellar properties of young stars, while millimeter observations provide the dynamical and kinematic information of natal molecular gas of forming stars. Indeed, with the capability of high-resolution millimeter interferometry, individual dense molecular clumps capable of forming single star can be well distinguished.

In this thesis, I focus on observing clusters around one to a few Herbig Ae/Be stars (HAeBes, Herbig 1960) (3 - 20 $M_{\odot}$) with age $<$ a few Myr and a few tens to a hundred companion low mass stars. These systems are still embedded or at least partially embedded within molecular clouds (Fuente et al. 1998a). With these observations, two primary questions to be addressed are:

- How does a solar-type low-mass star form and evolve in a cluster environment, compared with the well established picture of isolated star formation?
- What are the roles of clustering and massive stars in the natal molecular cloud and the formation and evolution of low-mass cluster members?

1.1 Stars are Born Deep Within Molecular Clouds

Over the last few decades, a picture of isolated solar-like star formation has been well established (e.g., Shu et al. 1993). The basic idea is that the forming low mass star gathers mass via active infalling and circumstellar accretion after the onset of gravitational collapse. Therefore, the star will experience an envelope phase (Class 0/I protostar) when there exists an optically thick envelope with heavily infalling matter, a disk phase (Class II protostar, also known as T-Tauri star, CTT)

when the envelope has been mostly evaporated but a massive disk is still accreting, and then a pre-main sequence phase (Class III, also known as weak-line T-Tauri star, WTT) when most material in the disk has disappeared but a solar-like planetary system may be developing.

As the star is forming, it also effectively disperses the surrounding molecular gas via outflows and jets (see review, Arce et al. 2007). Molecular outflows have been suggested to be the main sources clearing the circumstellar material around a forming low mass star. Highly collimated CO flows are ubiquitous with low mass protostars of age $< 10^5$ yrs, having velocities of 10-100 km s^{-1} and typical mass loss rates of 10^{-6} $M_{\odot}yr^{-1}$. However, there has been increasing evidence showing that the outflow characteristics, especially the collimation, and even the mechanisms, actually evolve with the low mass protostar (e.g. Tobin et al. 2007). Nevertheless, the star forming environment is dramatically impacted by the evolution of the forming star.

The formation of an intermediate-mass star (3 - 20 $M_{\odot}$) is probably similar to low-mass star formation. For example, Herbig Ae/Be stars are thought to be the intermediate-mass classical T-Tauri stars (see review, Waters & Waelkens 1998). However, more and more observational evidence suggests that the formation of massive stars, especially with spectral types of early B to O, is not simply a scaled-up version of low-mass star formation (see review, Zinnecker & Yorke 2007). Nevertheless, like a low mass star, gas dispersal is also expected for a HAeBe. Fuente et al. (1998a, 2002) mapped the molecular gas around HAeBes with different evolutionary stages and showed that the material around HAeBes are usually continuously swept out by outflows to form cavities as the HAeBes evolve. This also implies an alternative classification to characterize the evolutionary stage of HAeBes, in addition to the near-infrared scheme (Hillenbrand et al. 1992). Indeed, outflows associated with intermediate mass to massive protostars have started to be identified (e.g. Wu et al. 2005). It is suggested that the outflows of B stars have higher mass loss rates of 10^{-5} to 10^{-3} $M_{\odot}yr^{-1}$ with less collimation (e.g. Wu et al. 2005), compared to outflows from low-mass protostars.

1.2 The Majority of Stars in the Galaxy Form in Clusters

However, the majority of stars in the Galaxy form in clusters, rather than in isolation (e.g. Carpenter 2000; Lada & Lada 2003). Such clusters normally contain one or many massive stars

accompanied by a large number of lower mass stars. This should not be too surprising, as there has been growing evidence showing that even the Sun was born in a cluster. Isotopic studies of the short-lived radionuclide in the early solar system suggest the contamination from a nearby supernova ($\sim$ 0.02-1.6 pc distance, e.g. Looney et al. 2007), which implies that the Sun formed in a cluster environment with at least one cluster member that was massive enough to undergo a supernova explosion while the Sun was still forming.

Although clusters are the major mode of star formation, it is still poorly understood whether there is any fundamentally discrepancy between stars forming in isolation and clusters. Recently, more and more studies have started to focus on cluster systems. For example, Ridge et al. (2003) mapped the dense gas around young clusters within 1 kpc and also suggested a similar classification of cloud evolution, as seen in HAeBe systems (Fuente et al. 1998a, 2002). Nevertheless, examining the star-forming environment is crucial to understand the major mode of star formation. Therefore, based on the knowledge of isolated star formation, it is the aim of this thesis to provide insights in star formation in the cluster mode, by comparing to the isolated mode.

Furthermore, one would expect that clusters might complicate the star-forming processes. For example, both the initial clustering and the the continuous interaction between cluster members could contribute to the complexity. The initial clustering dominates the initial mass function (IMF), which might be determined by the turbulent fragmentation in clouds or competitive accretion between star forming cores (Pudritz 2002). On the other hand, the dynamical interaction between cluster members includes the close encounter between forming stars (Pfalzner et al. 2006) and impacts from massive stars on the natal cloud, such as strong outflows, stellar winds, and UV radiation. These factors are probably significant enough to modify the star forming processes in clusters from the standard isolated star formation picture, as stars form with much higher efficiencies and form much more closely in clusters than in isolation.

For example, disk truncations of young stars by UV radiation from massive stars have been suggested both theoretically and observationally. Studies on how EUV and FUV photons truncate the circumstellar disk and affect the formation of planets are increasing to date, especially theoretically. It is predicted that the disk mass loss decreases with the FUV flux, thus the distance to the massive star, so that the disk size would increase with the distance to the massive star within the

FUV dominated regime (Störzer & Hollenbach 1999). In addition, the star-disk encounter model (Pfalzner et al. 2006) also suggests a dependence between the disk mass loss and the distance to the cluster center, and further predicts that high and low mass stars are actually affected more seriously than intermediate mass stars. In fact, the discrepancy of the disk fraction between different spectral types of stars has been observed toward a nearby cluster, IC 348 (Lada et al. 2006). Moreover, direct observational evidence of truncated disks is also found in nearby clusters, such as the Proplyds in Orion (e.g., Vicente & Alves 2005).

Indeed, clusters host much more active and rapidly changing environments than isolated stars. Examining the star formation and evolution in clusters and comparing with isolated stars will help extend our understanding of the formation of most stars in the Galaxy, including the Sun.

1.3 Young Stellar Clusters around Herbig Ae/Be Stars

Although star formation can be simply characterized into two modes, isolation and cluster, there actually exist various star forming systems that probably result from different mechanisms. In particular, for cluster mode, there are (1) low mass clusters with a loose distribution of numbers of low mass stars, (2) intermediate mass clusters containing one to a few intermediate to high mass stars accompanied by 10's to 100's low mass stars, and (3) massive clusters including O stars or even OB associations surrounding a large number of low mass stars. Hillenbrand et al. (1995a) suggests that the number of cluster members seems to show a positive correspondence to the mass of the most massive stars in the cluster. Adams et al. (2006) even derives a relationship between the size of clusters and the number of cluster members, based on an infrared survey of nearby embedded clusters (Lada & Lada 2003).

In this thesis, I study the second type, the intermediate mass clusters around one to a few Herbig Ae/Be stars, for the following reasons. First of all, they are the simplest clusters that contain intermediate mass to massive stars. Indeed, massive clusters have higher probability to host more massive stars, which produce more feedback on the environment. These clusters, therefore, increase the ability to detect environmental effects on young cluster members observationally, but also increase the observational complexity. On the contrary, intermediate mass clusters, as the simplest clusters, can simplify the physical conditions and avoid the complexity due to the coupling

effects from multiple massive stars.

Secondly, they can be treated as basic units of star formation in clusters. Spitzer observations of young massive clusters revealed the existence of sub-structures (Allen et al. 2006). Wang & Looney (2007) further indicates that the sizes of these intermediate mass clusters are actually comparable to those sub-structures seen in massive clusters. Thirdly, the majority of cluster members of these intermediate mass clusters are all Sun-like low mass stars. This gives us a relatively smaller mass spread than that in massive clusters, so that we can approximatively waive the mass dependence while examining the age distribution in clusters.

Finally, with the ages of HAeBes less than a few Myrs, these intermediate mass clusters are still forming and embedded within their molecular clouds. This indicates that they are old enough for low-mass cluster members to have been born but young enough for natal molecular gas to be dispersing. Therefore, not only can young stars to be revealed and examined, but also can gas removal processes be investigated.

Chapter 2

Samples

I sample eleven nearby young stellar clusters around HAeBes with a few Myr within 2 kpc. The distance criteria is required so that it increases the sensitivity to detect lower mass cluster members as completely as possible. Table 1 lists the stellar parameters of the most massive star or stars in clusters. Short description of each cluster is also summarized as follows:

- **BD40** contains three HAEBE stars, BD + 40° 4124 , V1686 Cyg, and the southern star of V1318 Cyg binary, with age $\sim$ 1 Myr at 1 kpc. Molecular clumps have been detected centered on the southern star of V1318 Cyg, which is therefore believed to be the youngest and most actively forming star (e.g. Looney et al. 2006a). Moreover, more than 80% of the group members show near infrared excess (Hillenbrand et al. 1995a), which implies the youthfulness of this group. The fact that both massive and low mass stars form simultaneously within such a small scale provides us an excellent environment to study the star formation in the cluster.

- **NGC 7129** is a reflection nebula that contains three Herbig Be stars, LkHα 234, BD + 65° 1637, and BD + 65° 1638. A number of young stars have been found in this system, along with molecular outflows (Edwards & Snell 1983; Fuente et al. 2001) and dense molecular clumps centered on LkHα 234 (Wang & Looney 2007). It has been suggested LkHα 234 is the youngest among the three Be stars (Hillenbrand et al. 1992). Several authors have published the Spitzer photometric and spectroscopic results for this system (e.g. Megeath et al. 2004; Morris et al. 2004; Gutermuth et al. 2004). It is included as one of our sources for completeness.

- **MWC 297** is an O9e star at 450 pc (Hillenbrand et al. 1992). B1.5V at 250 pc is also suggested by other authors (e.g. Drew et al. 1997). We use the former in this paper. Dense

molecular emission, such as ^{13}CO and $C^{18}O$ (Fuente et al. 2002; Ridge et al. 2003), and molecular outflows (e.g. Drew et al. 1997) have been detected around MWC 297, which suggests an active star forming environment.

- **VY Mon** is a B8e star with age $\sim$ 0.1 Myrs, surrounded by $\sim$ 25 stars (Testi et al. 1998). ^{13}CO and $C^{18}O$ observations show that the dense molecular gas is distributed along an extended ridge around VY Mon (Ridge et al. 2003). Two 10 μm companions were detected (Habart et al. 2003).

- **VV Ser** is a B9e star with age $\sim$ 0.6 Myrs, surrounded by $\sim$ 24 stars (Testi et al. 1998). ^{13}CO and $C^{18}O$ observations show that the dense molecular gas is extended and VV Ser is located within a cavity of this dense gas (Ridge et al. 2003).

- **HD 97048** is an A0e star surrounded by a few stars.

- **BD46** system is embedded within a molecular cloud that includes the Herbig A0e star, BD + 46° 3471, and the B0 star, BD + 46° 3474. BD + 46° 3474 illuminates an emission nebula, IC 5146, that contains more than 100 stars, including four other late B stars; while $\sim$ 3.5 pc away, BD + 46° 3471 illuminates another emission nebula including more than 10 stars with an average age of 0.2 Myrs (Herbig & Dahm 2002). How two clusters with such different sizes form closely in the same cloud is still unsolved and it also makes this system interesting for the study of star formation.

- **V921 Sco** is an Be star away from the HII region, GAL 343.49-00.03, at the distance of $\sim$ 2 pc. This HII region contains the IR source, IRAS 16558-4228, and several radio sources. Four 10 μm companions around V921 Sco were detected (Habart et al. 2003).

- **MWC 1080** (V628 Cas) has been classified as a B0e star (Cohen & Kuhi 1979), with 20.6 $M_\odot$, 10^4 $L_\odot$ (Hillenbrand et al. 1992, 1995a), and a flat optically thick circumstellar disk (Hillenbrand Class I object for Herbig Ae/Be stars). See more details in Chapter 5.

- **HD 200775**, a B3 star, is the oldest system in my sample (8 Myr, Fuente et al. 2002) and has illuminated the reflection nebula, NGC 7023. A large biconical outflow cavity with a size $\sim$ 1.5 pc $\times$ 0.8 pc has been constructed (Fuente et al. 1998b).

Table 2.1. Stellar Paremeters of the Sources

Target[a]	Distance (kpc)	Massive[b] Star	M ($M_\odot$)	Spectral Type	Age (Myrs)	Refs.
BD40	1.00	BD + 40° 4124	13.0	B2e	0.06	1,2
		V1686 Cyg	4.5	B5e	0.6	1,2
		V1318 Cyg-S	-	mid A-Fe	0.6	1,2
NGC 7129	1.00	BD + 65° 1637	9.2	B3e	-	1
		LkHa 234	8.5	B3e	0.1	1
		BD + 65° 1638	-	B2	-	3
MWC 297	0.45	MWC 297	26.5	O9e	0.1-1.0	1,4
VY Mon	0.80	VY Mon	-	B8e	0.1	4
VV Ser	0.44	VV Ser	3.3	B9e	0.6	1,4
HD 97048	0.16	HD 97048	3.4	A0e	> 5.0	1,4
BD46	0.90	BD + 46° 3471	7.3	A0e	0.1-0.3	1,5
		BD + 46° 3474	-	B0	1.0	5
V921 Sco	0.8	V921 Sco	-	B0e	0.1-1.0	4
		GAL343.49-00.03	-	-	-	6

[a]Name of the cluster system used here.

[b]Massive stars that are included within the same cluster system or within the same molecular cloud.

References. — (1) Hillenbrand et al. (1992) (2) Hillenbrand et al. (1995a) (3) Harvey et al. (1984) (4) Habart et al. (2003) (5) Herbig & Dahm (2002) (6) Caswell & Haynes (1987)

- **Z CMa** is a close (< 100 AU) binary including a optically bright FU Orionis star, which is probably a 3 $M_\odot$ T-Tauri star undergoing an active disk accretion, and a 16 $M_\odot$ Herbig B0e star (Covino et al. 1984; Koresko et al. 1991; Hartmann et al. 1989; Polomski et al. 2005; van den Ancker et al. 2004). This system is still young as CO outflows, jets, and numbers of HH objects have been identified (Evans et al. 1994; Velázquez & Rodríguez 2001).

Chapter 3

Identifying Low-Mass Young Stellar Objects

Infrared color-color diagram is one of the most common way to separate young stars from normal stars. Recent studies in nearby embedded clusters have shown that photometry of Spitzer mid-infrared observations is efficient to identify young stars, especially to distinguish between stars with disks and envelopes (e.g. Allen et al. 2004; Megeath et al. 2004; Allen et al. 2006). For example, Hartmann et al. (2005) plots Taurus young stars with known classes (i.e. WTTs, CTTs, and Class I protostars), and shows that all of them are well separated in the color-color diagram, [3.6] - [4.5] vs. [5.8] - [8.0]. In addition, the color-color diagrams that combine IRAC and MIPS bands, for example [3.6] - [8.0] vs. [8.0] - [24] and [3.6] - [5.8] vs [8.0] - [24], are also efficiently used to identify young stars, especially for highly embedded stars and stars with significant inner holes (e.g. Rho et al. 2006; Lada et al. 2006). [3.6], [4.5], [5.8], [8.0], and [24] are Spitzer IRAC and MIPS bands at 3.6, 4.5, 5.8, 8.0, and 24 μm. Indeed, unlike the near infrared (e.g. JHK) emission from young stars, the IRAC ([3.6], [4.5], [5.8], and [8.0]) and MIPS [24] channels contain a significant fraction of emission from circumstellar material (disk or envelope) over the stellar photosphere, so these channels are more sensitive to probe the circumstellar characteristics than the near-infrared.

However, although technique using Spitzer observations has been proven useful to identify young stars, not all sources can be simultaneously detected at all bands, especially for low-mass protostars. This is because the [3.6] and [4.5] are much more sensitive than others (Fazio et al. 2004). On the other hand, [5.8] and [8.0] contain strong PAH emission that easily confuse the detection and photometry of point sources. Since the infrared data in this thesis are not deep and the majority of the young stellar population in sampled clusters are low-mass, photometry using only the IRAC bands is not reliable to identify young stars. Therefore, due to the intrinsic difficulties of nebulosity confusion and sensitivity at [5.8] and [8.0], only the [3.6] and [4.5] IRAC bands are used in this thesis and combined with J, H, and Ks to identify young stellar objects. In

fact, the J to [4.5] colors have been used in some studies of embedded clusters (e.g. Gutermuth et al. 2004).

Therefore, the main goal of this chapter is to investigate how the Class I/II protostars and Class III/normal stars can be best separated by using only J, H, Ks, and IRAC [3.6] and [4.5] band. In order to understand the infrared emission of low-mass young stars in these bands, I examine the colors of one of the most well studied and nearby young clusters IC 348 using the published infrared data (Luhman et al. 2003; Lada et al. 2006), and apply the results to my sample.

3.1 Case Study of IC 348

IC 348 is a partially embedded young cluster with age $\sim$ 2 Myrs at 260 pc, which contains $\sim$ 300 cluster members with spectral types from early B down to M (Muench et al. 2003). It is a cluster with an age and number of cluster members larger than sampled clusters in this thesis. I simply assume that the young stars in IC 348 are generally similar to those in my sample, so that I can compare techniques to identify young stars. Published NIR and Spitzer data of IC 348 are used, including the colors at J, H, Ks (Luhman et al. 2003), [3.6] and [4.5], SED-derived A_V, and classes of protostars (Lada et al. 2006). In order to obtain the intrinsic colors, the interstellar extinctions are corrected by applying the extinction laws from Rieke & Lebofsky (1985) for J, H, and Ks and Indebetouw et al. (2005) for the IRAC bands, which corresponds to $R_V = 5.5$. Moreover, in the paper of Lada et al. (2006), stars are classified as stars with pure stellar photospheres (star, hereafter called normal star), optically thick disks (thick), and anemic disks (anemic). Those stars with optically thick disks are most likely CTTs that have primordial disks while those with anemic disks are more like transition ones with mostly depleted disks. Here I only include stars with thick disks as young stars, in order to identify the primordial disk populations.

Figure 3.1 plots the absolute magnitude at [4.5] of normal and thick disk stars by applying the extinction and distance corrections. Using this figure, the range of spectral types of identified young stars at an assumed distance can be estimated. Figure 3.2 plots the dereddened color-color diagrams of H - [3.6] vs. [3.6] - [4.5] and Ks - [3.6] vs. [3.6] - [4.5] for IC 348, which are the methods often suggested by other authors (e.g. Hartmann et al. 2005; Allen et al. 2006). For example, Hartmann et al. (2005) showed that Taurus Class I/II protostars are clearly distinguished from

Class III sources in both diagrams, especially in the diagram of H - [3.6] vs. [3.6] - [4.5]. In Figure 3.2, normal and thick disk stars in IC 348 are indeed distributed as two groups in the color-color diagrams. However, normal stars will mix with thick disk stars when they are highly extincted; extinction is usually significant in embedded clusters. In addition, the solid lines in Figure 3.2, which were arrows drawn in the Taurus study (Figure 3 in Hartmann et al. 2005), can not separate thick disk stars from normal stars in IC 348 as well as those in Taurus.

Figure 3.3(a) and 3.3(b) plot two dereddened color-color J to [4.5] diagrams for normal and thick disk stars in IC 348. They are the best color-color diagrams to separate normal and thick disk stars. I derive lines that divide the normal and thick disk stars,

$$J - [3.6] = \frac{E(J - [3.6])}{E(Ks - [4.5])} \times (Ks - [4.5]) - 0.36 \tag{3.1}$$

(solid line in Figure 3.3(a) and 3.3(c)) and

$$H - [3.6] = \frac{E(H - [3.6])}{E(Ks - [4.5])} \times (Ks - [4.5]) - 0.2, \tag{3.2}$$

(solid line in Figure 3.3(b) and 3.3(d)), which are both along the direction of extinction with $E(J - [3.6]) = 0.219 \times A_V$, $E(H - [3.6]) = 0.112 \times A_V$, and $E(Ks - [4.5]) = 0.064 \times A_V$ (Rieke & Lebofsky 1985; Indebetouw et al. 2005). Because Equation (3.1) and (3.2) are along the direction of extinction, normal and thick disk stars can be still separated no matter how large the extinction. I also compare these two diagrams to Taurus' results (Hartmann et al. 2005). Figure 3.3(c) and 3.3(d) plot the colors of Class I-III protostars in Taurus in the same color-color diagrams as 3.3(a) and 3.3(b). They show that Equation (3.1) and (3.2) can also discriminate most stars with circumstellar material (CTTs and Class I) from stars without disks (WTTs). According to the results of IC 348 and Taurus, it can be concluded that at least 90% of young stars will be identified using Equation (3.1) and (3.2), and at most 10% of them are normal star contamination.

In summary, the color-color diagrams of J - [3.6] vs. Ks - [4.5] and H - [3.6] vs. Ks - [4.5] can best separate young stars from normal stars when using J to [4.5] colors only. These methods are especially useful for those low-mass clusters similar to Taurus and intermediate-sized clusters similar to IC 348. Methods of identifying young stars in different environments may be different

due to the environmental impacts on the young stars. Therefore, in the future, this should be tested in other environments, such as massive clusters.

3.2 YSO Loci and Circumstellar Parameters

From Figure 3.3, not only can the thick disk stars in IC 348 be identified in Figure 3.3(a) and 3.3(b), they are also distributed within narrow bands. Therefore, I obtain two loci (dashed lines in Figure 3.3) via least-square fittings,

$$J - [3.6] = (1.01 \pm 0.04) \times (Ks - [4.5]) + 0.79 \pm 0.04; \tag{3.3}$$

$$H - [3.6] = (0.95 \pm 0.04) \times (Ks - [4.5]) + 0.12 \pm 0.04, \tag{3.4}$$

which are called YSO loci here.

Meyer et al. (1997) first showed that the intrinsic near-infrared colors of CTTs in Taurus are distributed within narrow bands in the color-color diagrams of J - H vs. H - K and H - K vs. K - L, so called CTTs loci. It is suggested that young stars having accretion disks with disk accretion rates of 10^{-8} - 10^{-6} $M_{\odot}$ yr^{-1}, inner disk holes with sizes of 1 - 6 $R_{\star}$, and random inclinations, can explain the CTTs loci. Moreover, Figure 3.4 shows that thick disk stars in IC 348 also roughly locate along the CTTs loci. This means that those thick disk stars in IC 348 are probably just typical CTTs. In addition, Figure 3.3 and Equation (3.3) and (3.4) further suggest that this characteristic that young stars distribute within narrow bands in near-infrared color-color diagrams, is also valid in the mid-infrared. Indeed, the YSO loci could be treated as the extension of CTTs loci.

In order to understand the physical parameters of those thick disk stars in IC 348 and how they relate to the YSO loci, I obtain their stellar and circumstellar parameters by fitting their colors at J, H, Ks, and the four bands of IRAC with young stellar models (Robitaille et al. 2006, 2007). I choose the model with a best fit (with the least χ^2) for each star. Although the best-fit models do not necessarily provide the true values of stellar and circumstellar parameters of young stars, the fitting results can still provide some indications, such as ranges of these parameters.

Figure 3.5 plots the histogram of some parameters of these stars from the fitting, including the

age, the stellar mass, the disk mass, and the disk accretion rate. This figure suggests a parameter range for those stars along the YSO loci. I also obtain the parameters for Class II protostars (CTTs) in Taurus, for comparison (Figure 3.5). The fitting results and the Figure 3.5 show that low-mass stars with typical accretion disks having disk accretion rates of 10^{-14} - 10^{-6} $M_{\odot}$ yr^{-1}, disk inner holes with sizes of 0.01 - 10 AU, and random disk inclinations can have colors along the YSO loci.

Furthermore, in order to understand the relation between colors and circumstellar parameters for those stars along the YSO loci, their ages and disk accretion rates vs. dereddened H - K and K - [4.5] are also plotted in Figure 3.6 and 3.7. Trends showing positive correlations are shown in these figures, especially between colors and the disk accretion rate.

In summary, these results have shown that the intrinsic near- to mid-infrared colors of stars with disks with a wild range of circumstellar parameters can still distribute within narrow bands in the color-color diagrams, and stars in the low-mass cluster (like Taurus) and in the intermediate-size cluster (like IC 348) are actually along the same loci. This also implies that not only can the color-color diagrams of J - [3.6] vs. Ks - [4.5] and H - [3.6] vs. Ks - [4.5] be used to separate young stars from normal stars, they can also be used to estimate a range of interstellar extinctions in the cluster by applying the YSO loci, for different clusters.

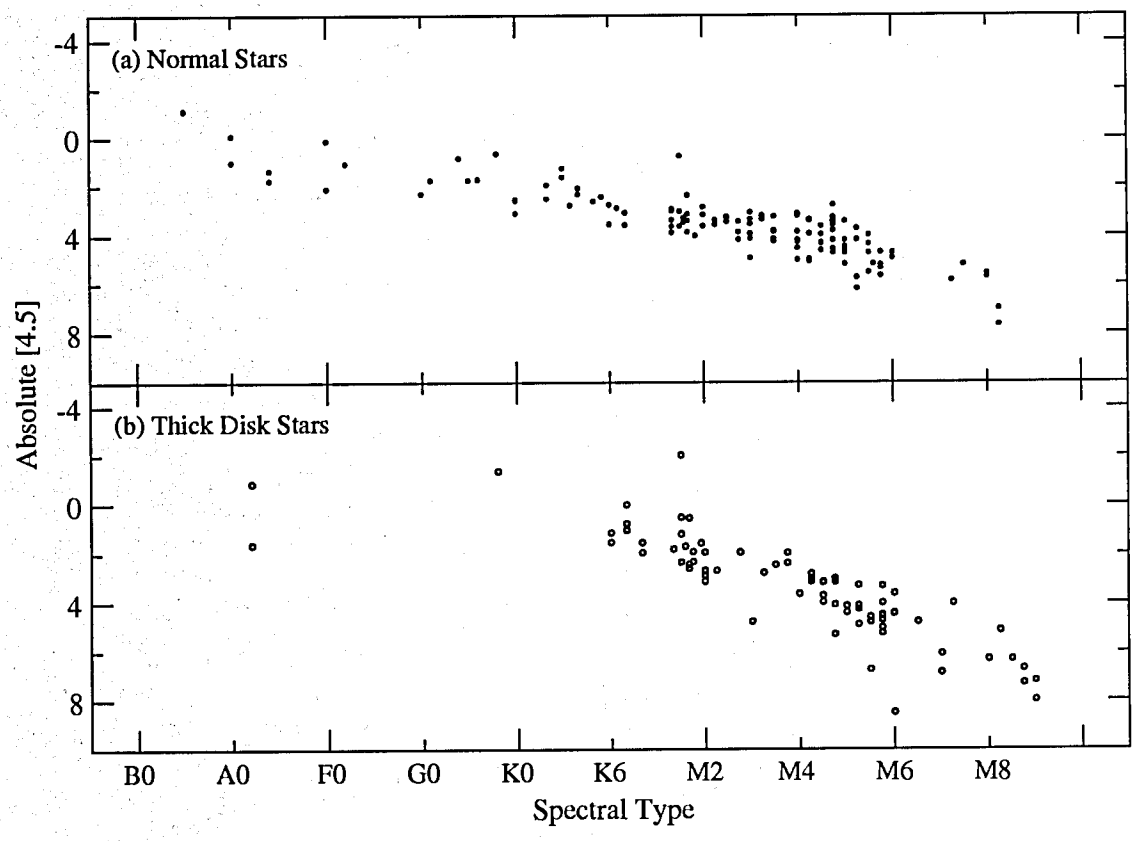

Figure 3.1 The absolute magnitude at [4.5] vs. the spectral type for normal (small dot) and thick disk (open circle) stars in IC 348 using the published data in Luhman et al. (2003) and Lada et al. (2006).

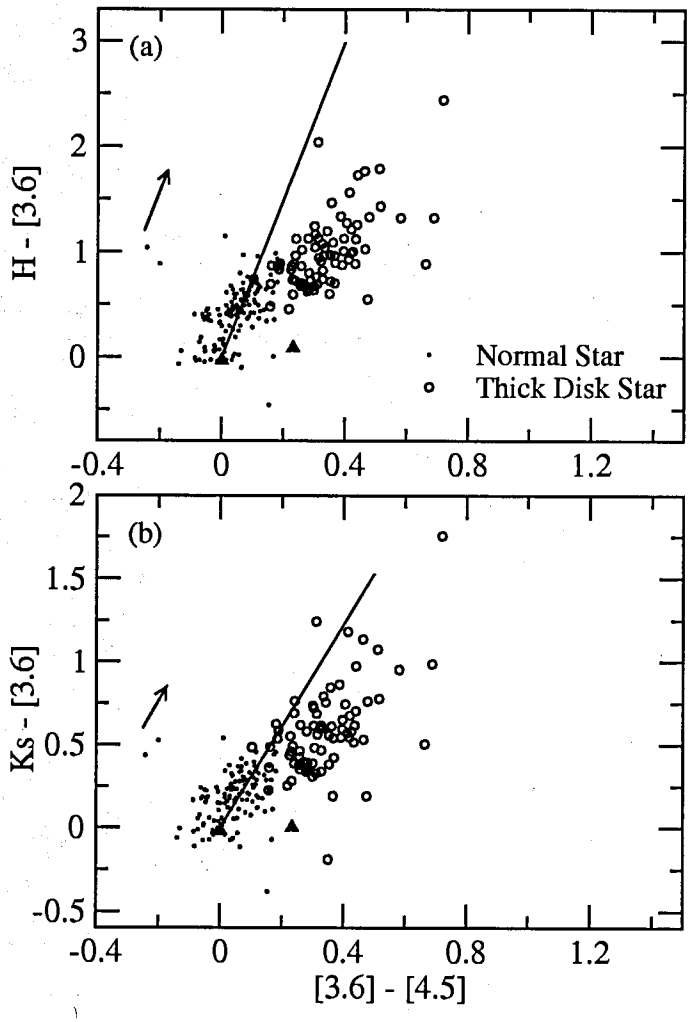

Figure 3.2 The dereddened color-color diagrams of H - [3.6] vs. [3.6] - [4.5] and Ks - [3.6] vs. [3.6] - [4.5] for normal and thick disk stars in IC 348. The small dot and open circle label the normal and thick disk stars (from G0 to M9), respectively. Two solid triangles are A type thick disk stars (thus, Herbig Ae stars). The solid lines are from the arrows that separate between Class I/II and Class III protostars in Taurus in Hartmann et al. (2005). The small arrows on the left side are the extinction vectors for $A_V = 5$.

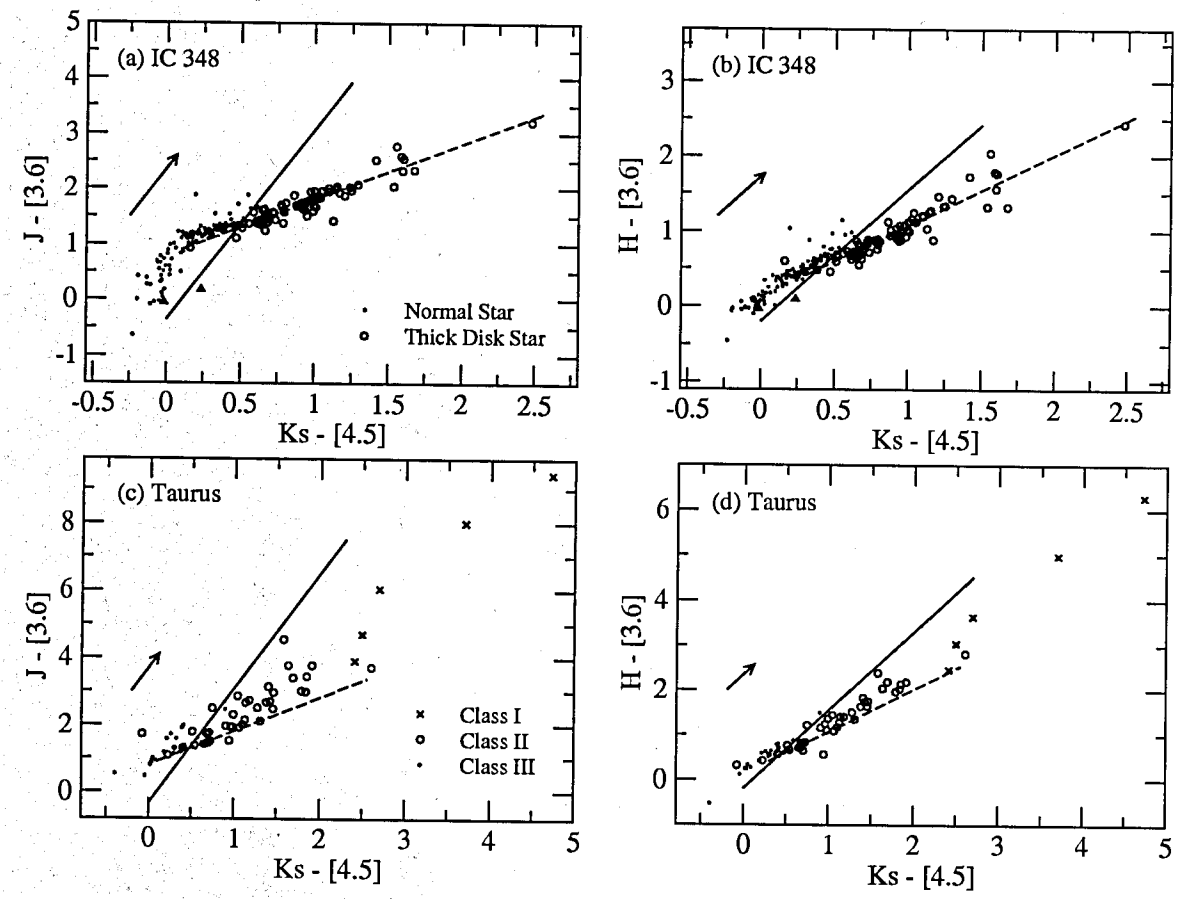

Figure 3.3 (a) and (b) are the color-color diagrams of J - [3.6] vs. Ks - [4.5] and H - [3.6] vs. Ks - [4.5] for dereddened normal and thick disk stars in IC 348; while (c) and (d) are those (not dereddened) for protostars in Taurus. In addition to the labels described in the figure, the solid triangles are Herbig Ae stars. The solid lines are Equation (3.1) for (a) and (c), and Equation (3.2) for (b) and (d). The arrows show $A_V = 5$. The dashed lines are YSO loci, Equation (3.3) and (3.4) (see Ch. 3.2).

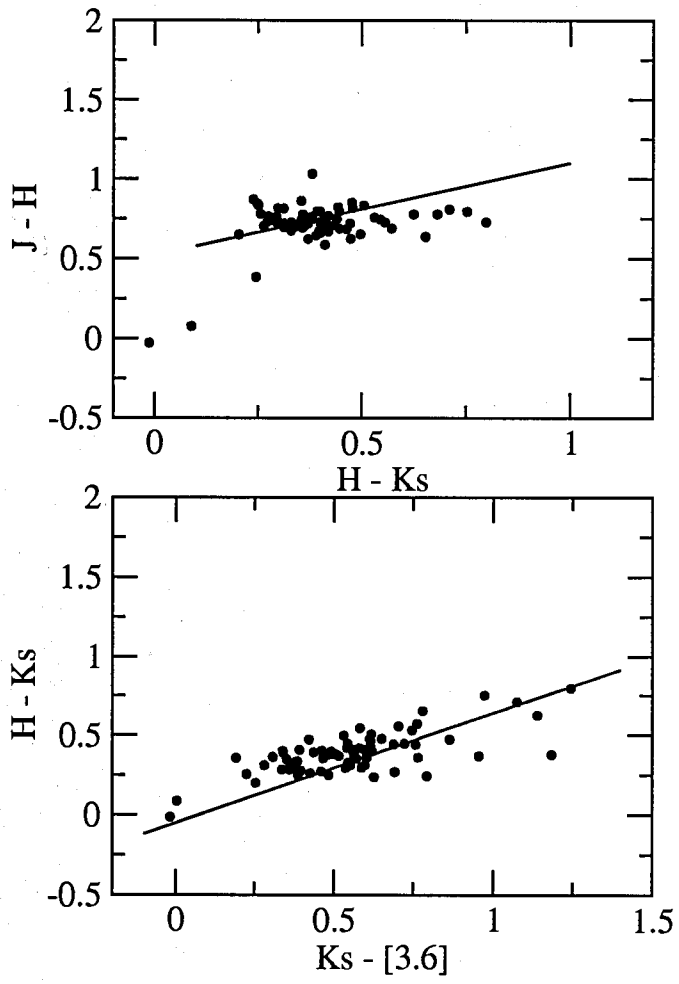

Figure 3.4 Color-color diagrams for thick disk stars in IC 348. Most of these stars distribute along the CTTs loci (the solid lines, Meyer et al. 1997), which are derived based on the intrinsic colors of CTTs in Taurus. This indicates that these thick disk stars in IC 348 have similar circumstellar properties as CTTs in Taurus.

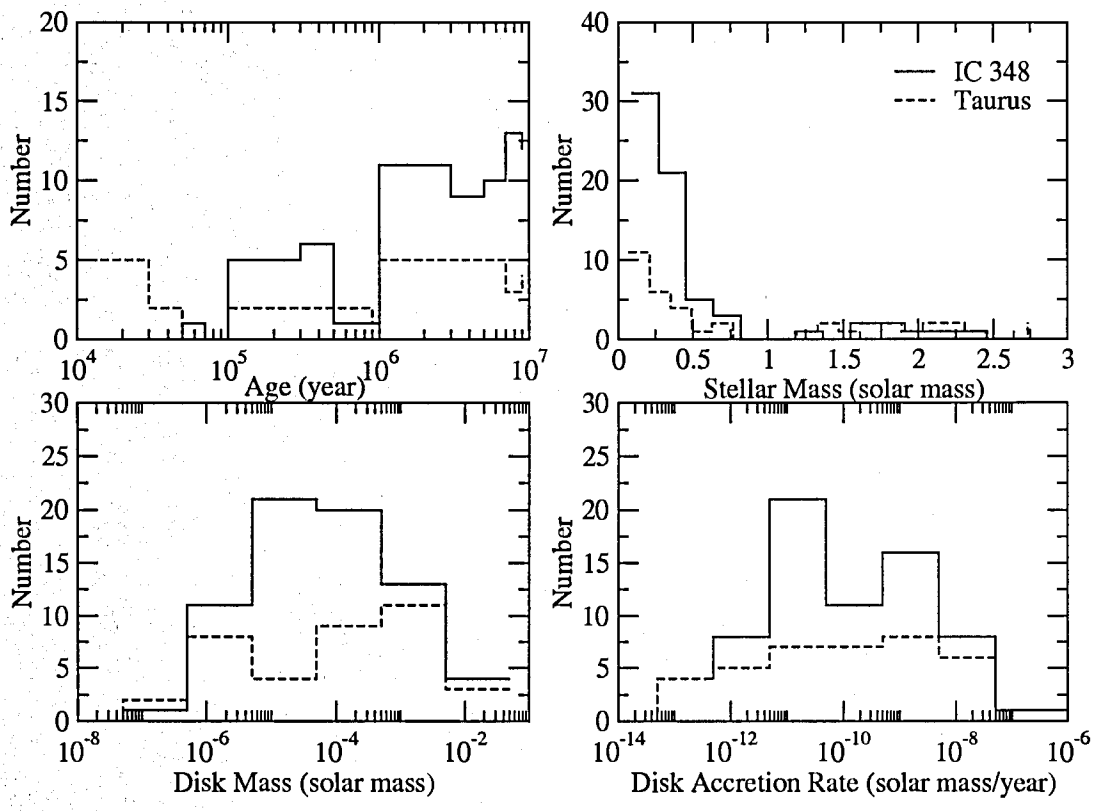

Figure 3.5 Histograms of fitted parameters of thick disk stars in IC 348 (solid lines) and Class II protostars in Taurus (dashed lines). This plot gives a range of the fitted age, stellar mass, disk mass, and disk accretion rate of those stars along the CTTs and YSO loci (Equation (3.3) and (3.4)).

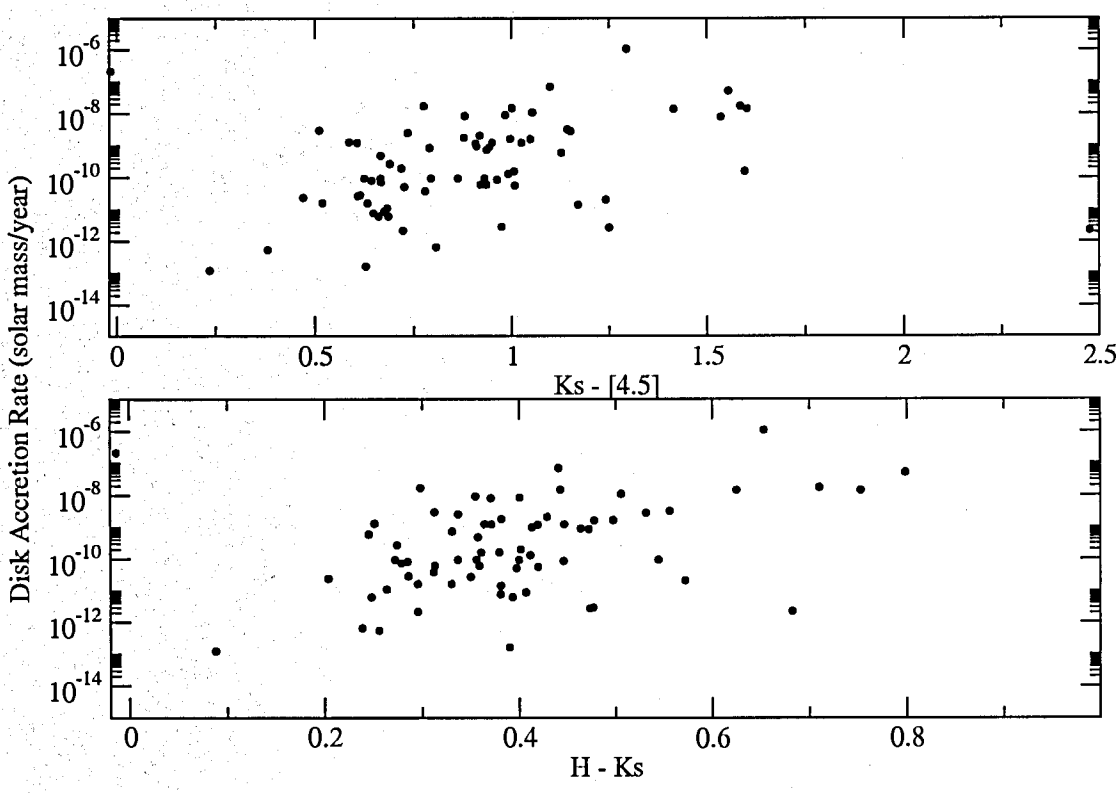

Figure 3.6 This figure plots the relation between colors and the fitted disk accretion rate for thick disk stars in IC 348. It is shown here that the redder stars show, the higher disk accretion rates stars are experiencing, for stars along the CTTs and YSO loci.

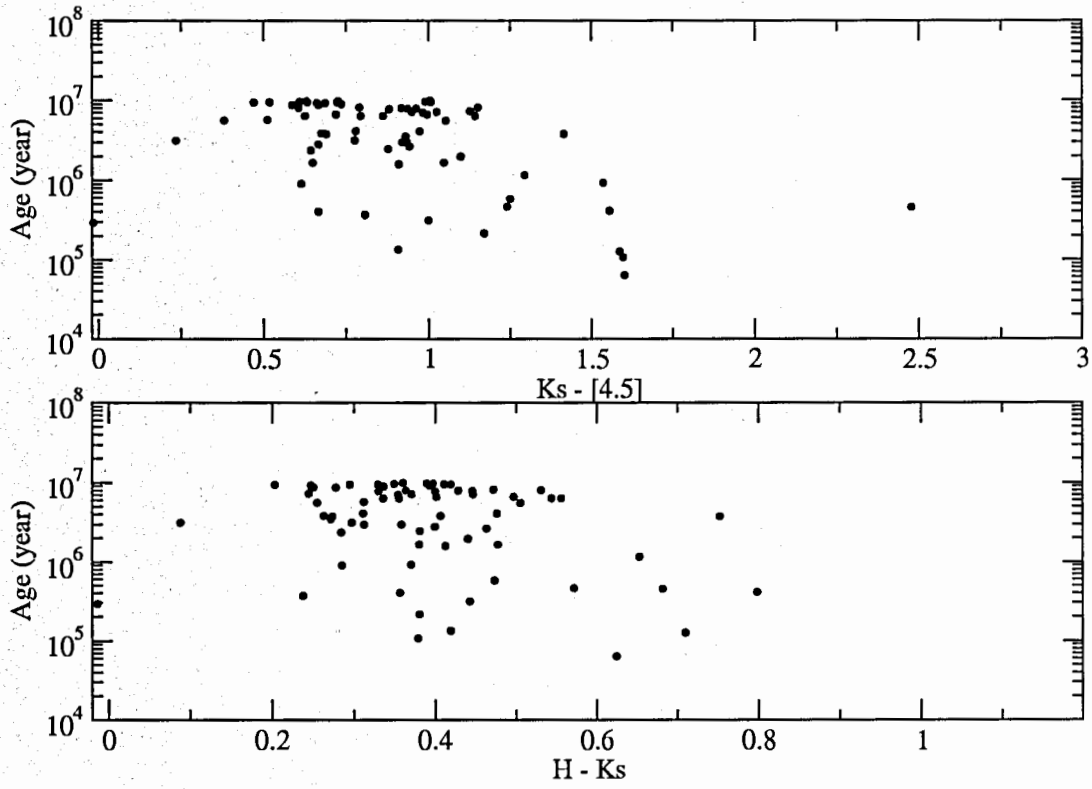

Figure 3.7 This figure plots the relation between colors and the fitted age for thick disk stars in IC 348.

Chapter 4

Large-Scale Young Stellar Population around Herbig Ae/Be Stars: A Low-Mass YSO Census

In order to understand the star-forming environment around HAeBes, the first step is to reveal the young stellar population and clustering around these systems. In this chapter, I present near- and mid-infrared observations of eight embedded young stellar clusters around HAeBes using archived Spitzer IRAC data and the 2MASS point source catalog. With Spitzer and 2MASS's spatial resolution ($\sim$ 2 arcseconds) and Spitzer's wide field of view, young stars from as close as $\sim$ 0.3 pc to a few pc radius from the HAeBes can be identified in my sample. Therefore, I can probe the young stellar distribution (1) around HAeBes to determine the sizes of clustering and (2) outside clusters to display the large-scale star-forming environments within which clusters form. This is a scale which is dominated by the initial clustering of stars in the natal molecular cloud. In addition, with Spitzer's high sensitivity, I can identify low-mass stars with mass down to early M drawfs. This gives 10 - 100 cluster members per cluster– enough to be studied statistically.

Main questions to be investigated are: (1) How are low-mass young stars distributed compared to the HAeBes; (2) Is there any clustering or environmental effects; and (3) What are the IR properties of identified young stars compared to isolated stars.

The majority of this chapter was published as "Young Stellar Groups Around Herbig Ae/Be Stars: A Low-Mass YSO Census", Wang & Looney, 2007, ApJ, 659, 1360.

4.1 Observations

Young stars are normally detected at infrared bands because their circumstellar dust re-emits the stellar light into the infrared regime and enhances the infrared luminosity (so called infrared excess).

I use data from the 2MASS (Skrutskie et al. 2006) point source catalog and the Spitzer Archive to obtain the photometry at near- (2MASS: J, H, and Ks) and mid- (Spitzer IRAC: [3.6], [4.5],

[5.8], and [8.0]) (Fazio et al. 2004) infrared bands. Table 4.1 summarizes the observational details of my sample from the Spitzer Archive. The source position and photometry of JHKs were obtained directly from the 2MASS point source catalog; the point source detection and photometry of IRAC data, which are PBCD in the Spitzer Archive, were accomplished using IRAF APPHOT package (daofind and phot tasks). Only sources above 5 σ are considered. I use an aperture radius of 3 pixel (3.6″) and sky annulus from 3 (3.6″) to 7 (8.4″) pixels for all point sources. I also use the zero magnitude of 21.108, 20.635, 20.1667, and 19.5 for IRAC [3.6], [4.5], [5.8], and [8.0], respectively (Fazio et al. 2004). The uncertainty of IRAC magnitudes is less than 0.05 mag for each channel of all sources. The detection limit at J band, J = 17, is applied, which corresponds to the 0.2 mag uncertainty. Table 4.2 list the detection limit at each band of the identified YSO candidates in this study. The last column in Table 4.2 is the spectral type whose color is the detection limit at [4.5] using Figure 3.1(b) (more details about Figure 3.1 in Ch. 3).

4.2 Spitzer Images and YSO Candidates

4.2.1 Dust Morphology

RGB color composite images of all sources are plotted in Figure 4.1, where [3.6], [4.5], and [8.0] are displayed as blue, green, and red, respectively. This figure shows the distribution of dust in red, which contributes significantly at [8.0]. The emission comes from thermal dust continuum illuminated by the massive HAeBes and the PAHs, that often trace the star forming regions. From this figure, we can see that all but two of my sources show bright diffuse emission in channel [8.0]. However, the most massive star in the system, the HAeBe, is not always at the center of the dust. For example, the BD40 system is in a dust-rich environment and located right at the intersection of two branches of dust with different position angles. This is consistent with the two systemic velocities of dense gas that suggests that the high star forming activity is due to the collision of clouds. (Looney et al. 2006a). Unlike MWC 297, which has a basically centered symmetric dust nebula, the VY Mon and NGC 7129 systems are located at the edge of dust structures. These one-side structures may result from the disruption of the natal cloud by the massive star in one direction. However, we can not exclude the possibility that massive stars may not primordially

form in the center of a dense cloud. Two of our systems, HD 97048 and VV Ser, show very little dust emission. This might be because they are both at the lower mass end of HAeBe stars (3.4 and 3.3 M$\odot$, respectively)– not energetic enough to illuminate their environments.

Interestingly, the bright dust structures in two systems, BD46 and V921 Sco, are actually not associated with the HAeBes, BD + 46° 3471 and V921 Sco, respectively. In the BD46 system, a symmetric morphology of dust with radius $\sim$ 2 pc is centered on the B0 star, BD + 46° 3474, while no obvious dust is detected around the A0e star, BD + 46° 3471. Again, this might be because BD + 46° 3471 is not massive enough, as it is an A0e star. On the other hand, in the V921 Sco system, there are multiple dust accumulations. The brightest dust feature is centered on the HII region, GAL 343.49-00.03, with radius $\sim$ 1 pc and $\sim$ 2 pc away from the B0e star V921 Sco. The Spitzer image also shows there is a large group of optically invisible stars deeply embedded within this HII region, that might suggest it is the most active star forming region in the area. Two other small dust clumps with radius $<$ 0.5 pc are centered on two IRAS sources, IRAS 16566-4229 and IRAS 16570-4227, $\sim$ 2 and 2.5 pc away from the HII region, respectively. As shown in Fig. 4, there is also some dust around the B0e star, V921 Sco. How the small groups of stars around BD+46° 3471 and V921 Sco form so closely to the large clusters around BD+46° 3474 and the HII region is interesting and still unknown. For the BD46 system, the BD+46° 3471 cluster might form and escape while the gas within the BD + 46° 3474 cluster was dispersing, because BD + 46° 3471 seems to be isolated without any diffuse dust connected to the BD + 46° 3474 nebula. However, for the V921 Sco system, the V921 Sco cluster might form due to the collision of turbulent clouds near the actively forming cluster (the HII region), because both of them are surrounded by a large scale diffuse dust.

Table 4 lists the estimated spatial radial scales for the dust around the massive stars, defined as R_d. We briefly conclude that clusters around the HAeBes whose spectral types are earlier than B8 are usually associated with bright dust and PAH emissions, although the formation mechanisms of my sample may be varied due to their different morphologies.

4.2.2 Color-Color Diagrams

As shown in Ch. 3, after examining the intrinsic colors of young stars in IC 348 and comparing them to the results in Taurus, I decide to use the color-color diagram of J - [3.6] vs. Ks - [4.5] as the tool of identifying young stars in this thesis. All stars with colors redder than Equation (3.1) in this color-color diagram are young stellar candidates (hereafter called YSO candidates).

Figure 4.2 shows the color-color diagrams of J - [3.6] vs. Ks - [4.5] for all sources. The solid and dashed line are Equation (3.1) and (3.3), respectively. Stars redder (rightward) than the solid lines are characterized as YSO candidates; while those YSO candidates above the dashed lines are most likely thick disk stars (CTTs). From this figure, we can see that most of YSO candidates are indeed CTT-like. Those YSO candidates below the dashed lines and with large Ks - [4.5] may be young A or F stars, similar to those in the color-color diagram of J - H vs. H - K in Figure 15 of Hillenbrand et al. (1992).

Table 4.3 also summarizes the total number of identified YSO candidates for each source in the whole data field and inside the cluster, respectively. I simply define that the stars within the dust region (R_d, estimated in the Ch. 4.2.1) are inside the cluster. Adams et al. (2006) derived the relationship between the number of cluster members (N) and radius of the cluster (R), $R = \sqrt{3}$ pc $(N/300)^{1/2}$. Based on this equation, I calculate the cluster radius (R in Table 4.3) assuming that the entire population consists of the YSO candidates. The result that R is comparable or less than R_d (see Table 4.3) shows that the number of detected YSO candidates in clusters is actually close to or less than the number of cluster members. Based on the number of YSO candidates, my sample can be sorted into three divisions: (1) $\sim$ 10 YSO candidates for HAeBes later than B9: BD + 46° 3471 and HD 97048; (2) 20-50 for single HAeBes earlier than B9: MWC 297, VY Mon, VV Ser, and V 921 Sco; (3) > 50 for multiple HAeBes or B stars: BD40, NGC 7129, and BD + 46° 3474. The HII region in the V921 Sco system is not included because it is actually not a HAeBe cluster. This categorization implies a positive trend between the mass and number of massive stars and the number of young stars in clusters, just as suggested by other authors (e.g. Hillenbrand et al. 1995a; Palla et al. 1995). Despite the categorization, we can simply conclude that there are normally 10 - 50 young stars distributed centered at or close to the HAeBes.

Moreover, according to Figure 4.2, the interstellar extinction for each CTT-like YSO candidate

can be estimated using the offset from the YSO locus (Equation (3.3)). Except the V921 Sco system, which shows a relatively high extinction ($A_V \sim 10$ - 20 in average), the majority of the extinction is < 10 (peak at ~ 5) for YSO candidates in my sample.

Figure 4.3 plots those YSO candidates in my sample with the identification of all four IRAC bands in the color-color diagram of [3.6] - [4.5] vs. [5.8] - [8.0]. We use the classification scheme proposed in Megeath et al. (2004) to characterize these YSO candidates: 10 %, 3 %, 80 %, 1 %, and 6 % of them are Class 0/I, Class I/II, Class II, reddened Class II, and normal stars, respectively. This is consistent with the conclusion that more than 90 % of YSO candidates are most likely young stars, from the case study of IC 348 in Ch. 3.

There is the possibility of contamination from background galaxies in our YSO candidate sample. Harvey et al. (2006) use the Spitzer Wide-Area Infrared Extragalactic Survey (SWIRE) Elais N1 data (Surace et al. 2004) to determine the extragalactic contaminates; they find that ~ 25 of the 591 sources (assuming they are all extragalactic) within 0.89 degree^2 meet their YSO selection criteria. In other words, on average ~ 25 extragalactic sources are misidentified as YSO candidates within 0.89 degree^2. Although our YSO selection criteria are different (see Section 3), my results can be compared numerically, as most of the sources are foreground or background sources. For example, in sampled clusters, $\sim$ 5 - 15 % of identified point sources are YSO candidates, only slightly larger than the $\sim$ 5 % in Harvey et al. (2006). This is not surprising as it is expected to have more YSOs in my sample of pointed star formation observations compared to the large-scale survey. In other words, the YSO selection criteria are consistent with each other. Moreover, the detection limit at [8.0] in my sample, < 14.0 (Table 4.2), is higher than that of the 25 extragalactic sources. Therefore, I adopt their value of 25 extragalactic sources in 0.89 degree^2 as an upper limit to extragalactic contamination of my YSO candidates. For my sources, with small fields of view, it is unlikely that there will be more than a few extragalactic sources in each of sampled fields. Therefore, I can conclude that the contamination from background galaxies should be negligible.

4.2.3 Spatial Distribution of YSO Candidates

One of the most basic questions when studying star formation in clusters is the location of the young stellar population. Two elements determine the distribution of young stars in the cluster, the initial

cloud condition and the interaction of cluster members. Clusters form through the fragmentation of the molecular cloud, which is determined by the initial conditions, such as the gravitational potential, velocity field of the gas, magnetic field, and turbulence (see review, Meyer et al. 2000). However, after the onset of individual collapse in the cluster, the forming stars will continue being affected by the dynamical evolution of the cluster, for example, the removal of gas, feedback of stars, and collision between cluster members. With the continuous modification of the dynamical state in the cluster, the distribution of stars might change dramatically. Adams et al. (2006) modelled the early evolution (within 10 Myr) of clusters with 100 - 1000 members with respect to the boundness, cluster size, virial ratio, and number of cluster members with time. Their results showed that the gas dispersal plays a primary role in the evolution of these parameters. For example, in their Figure 3, the fraction of bounded cluster members is decreased from 1 to 0.2 within 5 Myrs after the gas dispersed for the virial initial condition. Although this depends on the real gas dispersal processes dramatically, it implies that there is a significant fraction of cluster members that will escape the cluster eventually; there should be a significant fraction of isolated stars actually formed in clusters. Moreover, Allen et al. (2006) studied several embedded clusters from the Spitzer survey and showed that protostars tend to distribute in elongated morphologies around massive stars, along with some sub-clustered structures. They suggested that the distribution of protostars may still appear as the primordial structure of the natal cloud. Indeed, studying the spatial distribution of young stars in clusters will allow us to assess not only the cluster formation but its history.

Figure 4.4 plots the number density of YSO candidates vs. the distance to massive stars. For example, in the BD46 system, it is centered on BD + 46° 3471, instead of BD + 46° 3474. The number density defines the number of YSO candidates per surface area (number pc^{-2}). From this figure, we can see that there are indeed clusters of YSO candidates around the massive stars as expected, but also a young stellar population throughout the whole field outside the cluster. Those YSO candidates outside the cluster are mostly distributed uniformly. However, there are some clumps of young stars outside the clusters around HAeBes, for example, MWC 297 and BD46. The young stellar cluster around HAeBes, the clumps of young stars outside the cluster, and the overall distributed young population may be formed as a part of sub-clustered structures of a big dispersed cluster. The fact that there exists a young population outside the cluster is reasonable as the cluster

is actually embedded in a large-scale molecular cloud. The Spitzer observations of several young stellar clusters, including NGC 7129, show a similar picture (Megeath et al. 2004; Gutermuth et al. 2004) – a significant fraction of identified young stars distributed outside the cluster core. Their results also show that these young stars outside the cluster are actually well associated with the large scale dense molecular gas. They also suggest that the cluster forming environment plays an important role in determining the morphology of the young stellar population.

From Figure 4.4, we also can estimate the spatial size of the young stellar cluster around HAeBes (R_n in Table 4.3) and the clumps of young stars outside the cluster. These clusters and clumps have the sizes $\sim$ 0.5 - 1 pc, which are similar to the sizes of those sub-cluster structures in massive clusters (Allen et al. 2006). This further supports the suggestion in Section 1 that these clusters can be treated as basic units of studying the star formation in clusters. In addition, Table 4.3 shows R_d and R_n are basically consistent, as R_d shows the range of the dust distribution and R_n probes the spatial clustering of the YSO candidates.

In summary, my results suggest that the clusters around HAeBes usually contain 10 - 50 young stars within the dust emission and form relatively isolated clusters separated from the other regions in the large scale molecular cloud. The HAeBes are normally located near the center of the cluster of young stars. These clusters can be treated as sub-structures of the large scale young stellar population within the molecular cloud, as the clumpness of YSOs throughout the whole fields are seen. Each clump and group can also be compared to those sub-cluster structures found in massive clusters.

4.3 SED Slopes vs. Distance to the HAeBes

The slope of the spectral energy distribution (SED) is often used as the parameter indicating the youthfulness of a young star (e.g. Wilking et al. 1989). The SED slopes of the YSO candidates in my sample are also derived, using Ks, [3.6], and [4.5]. However, the SED slope is modified by the interstellar extinction. I derive the SED slopes of YSO candidates in the BD40 system with A_V = 0, 5, 10, 15, and 20, and conclude that the SED slope will change $\sim$ +0.4 per increasing A_V = 5. This provides an uncertainty to the SED slope derivation, along with the estimated A_V from Figure 4.2, for each of our sample.

4.3.1 Environmental Impact from Massive Star and Clustering

Not only are the position and mass of young stars affected by either the massive star or clustering, but the evolutionary stages of the clustering stars may also be affected. During the formation of massive stars, the molecular gas is actively disrupted by their strong stellar winds and UV radiation fields. These two factors might effectively alter the formation and evolution of protoplanetary disks, too. Studies on how EUV and FUV photons truncate the circumstellar disk and affect the formation of planets are increasing, especially theoretically. It is predicted that the mass loss decreases with the FUV flux, thus the distance to the massive star, so that the disk size would increase with distance to the massive star within the FUV dominated regime (Störzer & Hollenbach 1999). In addition, alternative models about how close encounters of cluster members affect the size and mass loss of circumstellar disks are also studied. Pfalzner et al. (2006) suggested that the mass loss on the disks decreases with the distance from the cluster center due to the star-disk encounter, and high and low mass stars are affected more seriously than intermediate mass stars by the cluster environment. The recent observational result of the cluster IC 348 (Lada et al. 2006) also showed a dependence between the disk fraction and the mass and spectral type of stars. Direct observational evidence of truncated disks is also found in nearby massive clusters, such as Orion. Vicente & Alves (2005) probed the disk size distribution in the Trapezium cluster. However, they found no correlation between disk size and the distance to the massive star or between disk size and the mass of the star, as theories predict (e.g. Störzer & Hollenbach 1999). They suggest that there might be various mechanisms of disk destruction happening so that no obvious correlation is shown.

In order to investigate the relationship between massive stars and low mass young stars, I plot the SED slope of YSO candidates vs. radial distance from HAeBes (Figure 4.5 and 4.6). The normal stars are also ploted as comparison. If the massive star truncates the circumstellar disks of its companions, stars closer to the massive star might reveal themselves earlier than they would normally. Therefore, these stars might look older than those further away, so there might be a correlation between the youthfulness (SED slope) and the distance to the massive stars. From Figure 4.5 and 4.6, we can see that there is a young population near the HAeBe star differing from the large-scale, uniform distribution, especially for BD40, VV Ser, and BD46. However, there is no obvious trend between the SED slope (youthfulness of young stars) and the distance from massive

star. This confirms that at the scale of my study, the clustering of young stars dominates over the effect of massive stars on the low-mass stars. Indeed, the range showing the existence of proplyds in Orion is $\sim$ 0.3 pc (Vicente & Alves 2005). Because Orion is a much more massive cluster than my sample, any similar effect from HAeBes would probably occur on scales much less than 0.3 pc. However, for my sample, within this range, there are typically < 5 YSO candidates because of the resolution of Spitzer and the saturation of the HAeBes, so it is unlikely to detect any effect from massive stars.

4.3.2 YSOs in Group vs. Isolation Within the Same Cloud

Although there is no obvious trend between the SED slope and the distance to HAeBe of the YSO candidates in groups, Figure 4.5 and 4.6 shows a possible age dispersion of YSO candidates throughout the molecular clouds, especially between inside and outside the cluster. Indeed, from Figure 4.5 and 4.6, the YSO candidates in clusters around HAeBes tend to have larger SED slopes than those outside. This means that there is an enhancement of not only number but also the youthfulness of YSOs within clusters compared to those outside. Actually, this is not unexpected, especially for low mass clusters, which often show hierarchical structures within the natal molecular cloud. Previous observations of the giant molecular cloud, Lynds 1641, suggest that there exist not only aggregates of mainly low mass protostars, but also a distributed population of young stars throughout the whole cloud (e.g, Strom et al. 1993; Allen 1995). Strom et al. (1993) found more young stars are within the aggregates than distributed. Allen (1995) found stars within the aggregates have average ages less than those distributed. In my sample, a similar picture to Lynds 1641 is seen. Allen (1995) suggested that this is because there is a constant star forming rate within the aggregates that constantly disperses forming stars outward, that produce those isolated young stars. Another explanation for isolated young stars outside the aggregates is that they formed isolated within the cloud initially so that the observational result is showing a primordial age dispersion throughout the cloud.

However, these results may be biased by the extinction, which would redden stars to make them seem younger, especially in the regions near the cluster center. According to the extinction estimation, extinction would affect the SED slopes by 1 at most with $A_V \sim 10$. This is still less

than the difference (~ 2) of SED slopes between the majority of YSO candidates inside and outside the cluster. Therefore, we can conclude that the deviation of SED slopes due to extinction is not significant so that there is indeed a trend showing YSOs in the clusters are younger.

As a cluster of young stars can be defined using the surface number density (R_n from Figure 4.4), it can alternatively be defined by the aggregates on the age dispersion from Figure 4.5 and 4.6. They do not necessary have to be the same as the spatial distribution can be different from the age distribution of young stars. For example, assuming a single star forming epoch, if R_n is smaller than the aggregates on the age dispersion, some stars formed together in the beginning may have escaped out of the boundary of clusters; on the contrary, if R_n is larger than the aggregates on the age dispersion, the impact from massive stars may have dominated the inner region of clusters. Applying the estimated R_n into Figure 4.5 and 4.6 shows that the sizes of the clusters around HAeBes based on Figure 4.5 and 4.6 are consistent with R_n. This consistency may suggest that the escape of YSOs from the cluster is not yet significant for my sample. In other words, the primordial fragmentation of the molecular cloud may still dominate the young stellar population outside the cluster in my sample.

Again, there is a cluster of YSO candidates around the HAeBe younger than those outside the cluster, especially for BD + 40° 4124 , NGC 7129, VY Mon, VV Ser, BD + 46° 3471, and BD + 46° 3474. Possible explanations of this trend are: there is a higher star forming rate and continuous star formation within the cluster than outside the cluster (as suggested in the Lynds 1641 study, Allen 1995), clusters tend to form after isolated low mass stars because they need more time to collect enough material to initial the formation, or stars in clusters form slower than isolation due to the competition of material with cluster members that delay the collapse of clumps in the beginning. Similar studies are needed for massive clusters or low mass clusters for further investigation.

4.4 Summary

In this chapter, I present the NIR and MIR observations of eight embedded young stellar clusters around Herbig Ae/Be stars (3-20 M$\odot$ at age $\sim$ a few Myrs) using the 2MASS point source catalog and the Spitzer archive. I use the color-color diagram of J - [3.6] vs. Ks - [4.5]. I do not use colors

of [5.8] and [8.0] because of their intrinsic difficulties at nebulosity confusion and sensitivity. With identified YSO candidates, I can study the cluster environment and cluster formation by examining their spatial distribution and infrared properties (such as SED slopes), compared with the position and mass of the HAeBes. Some results are summarized as follows.

- Six of the sources show bright diffuse emission at [8.0], which traces the dust illuminated by the HAeBes. The other two are the lowest mass clusters, VV Ser and HD 97048, which may not be energetic enough to illuminate the surroundings.
- The HAeBes are not always located at the center of the dust emission. BD + 40° 4124 is at the intersection of two branches of dust. VY Mon and NGC 7129 are at the edge of the dust nebulae. Others are located at the center of symmetric dust nebulae.
- There are indeed young clusters, containing 10-50 young stars, around HAeBes to form a relatively isolated system separated from the other regions within the large-scale molecular cloud. The HAeBes are always near the center of young stars.
- The clusters around HAeBes seem to be the sub-structure of a large young population within the cloud. The sizes of clusters based on the spatial population of young stars are similar to sub-cluster structures found in more massive clusters. Further comparison between these small clusters and massive clusters are needed.
- There is no obvious trend between SED slopes and the distance to the HAeBes, that suggests that the effect of clustering on young stars dominates over the effect of massive stars, at the scale of my study in this chapter.
- Young stars in clusters around HAeBes tend to show larger SED slopes than those outside the clusters. It suggests that young stars in clusters are even younger than those outside. Some possible explanations are: (1) there is a higher star forming rate and a continuous star formation rate within the cluster than outside the cluster (2) massive stars form later than low mass stars within the large-scale molecular cloud, or (3) low mass stars in the cluster form slower than isolated ones due to the effect of clustering or the massive stars. Comparisons with more massive clusters are needed in the future.

Table 4.1. Spitzer Archives of the IRAC Observations

Target	Program ID.	Exp. Time (Sec. / Frame)	No. of Frames	FOV[a] (′) × (′)	Refs.
BD40	6	10.4	4	12.4 × 14.5	1
NGC 7129	6	10.4	4	12.4 × 14.0	1
MWC 297	6	10.4	3	12.6 × 14.5	1
VY Mon	6	10.4	4	12.4 × 14.5	1
VV Ser	174	10.4	2	08.6 × 23.4	2
HD 97048	36	96.8	10	13.0 × 15.0	3
BD46	6	10.4	2	26.4 × 28.0	1
V921 Sco	192	1.2	2	19.5 × 37.8	4

[a]Final field of view of the data set used for each source.

References. — (1) GTO young embedded cluster survey by Fazio et al. (2) C2D legacy program by Evans et al. (Evans et al. 2003) (3) GTO deep IRAC imaging for brown dwarfs by Fazio et al. (4) GLIMPSE legacy program by Churchwell et al. (Benjamin et al. 2003).

Table 4.2. Detection Limits of the Sources

Target	J	H	Ks	[3.6][a]	[4.5][a]	[5.8][a]	[8.0][a]	Spectral Type[b]
BD40	17.00	15.85	15.95	15.11	15.06	13.20	12.37	M4
NGC 7129	16.99	16.09	16.99	15.62	15.72	14.00	12.88	M4
MWC 297	16.99	16.13	15.51	14.68	14.60	13.59	12.34	M5
VY Mon	16.87	15.84	14.99	13.98	13.53	13.43	12.53	M4
VV Ser	16.97	16.06	16.66	15.21	15.16	13.24	12.32	M6
HD 97048	16.73	16.08	15.10	14.89	14.17	14.09	13.83	M9
BD46	16.97	16.28	16.78	15.72	15.76	13.44	12.46	M5
V921 Sco	16.00	15.34	14.95	13.31	12.73	11.11	10.29	M2

[a]The lower limits at magnitude when the uncertainty criterion is 0.05 mag.

[b]The spectral type of the dimest detected YSO candidates, estimated based on [4.5] from Figure 3.

Table 4.3. YSO Detection of the Sources

Target	Num. of YSOs (whole field)	Num. of YSOs[a] (in groups)	R[b] (pc)	R_d (pc)	R_n (pc)
BD40	134	74	0.9	1.5[c]	0.6
NGC 7129	106	53	0.7	1.0	1.0
MWC 297	92	24	0.5	0.6	0.5
VY Mon	42	26	0.5	0.8	0.75
VV Ser	148	22	0.5	0.4	0.5
HD 97048	16	~ 10	-	-	-
BD + 46° 3471	500	~ 10	-	-	1.3[d]
BD + 46° 3474	500	238	1.5	2.4	1.5
V921 Sco	1271	33	0.6	0.7	-
GAL343.49-00.03	1271	160	1.3	1.2	-

[a]Number of YSO candidates within R_d.

[b]The radius calculated by $R = \sqrt{3}$ pc $(N/300)^{1/2}$ (Adams et al. 2006), where R is the radius and N is the number of YSOs within the groups.

[c]This value actually includes the two branch of dense dust around this system, which is overestimated for the group itself.

[d]It actually includes two separated nearby small groups of YSO candidates.

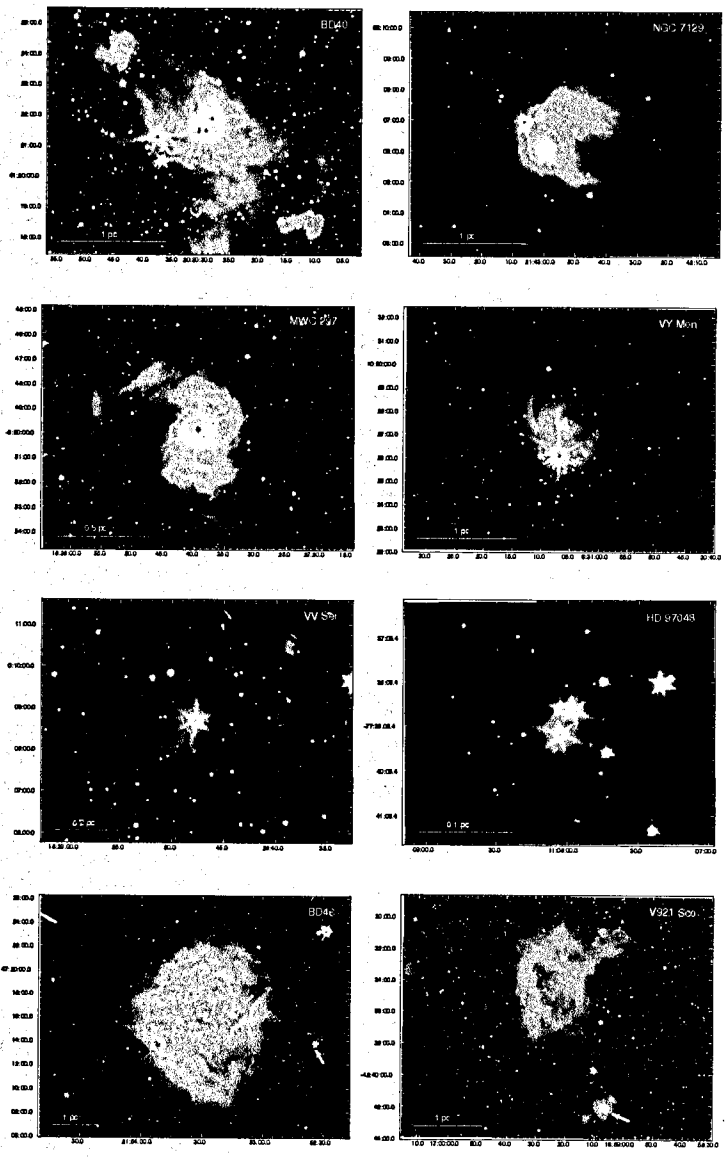

Figure 4.1 Spitzer Images of my sample with coordinates in J2000. [3.6], [4.5], and [8.0] are displayed as blue, green, and red, respectively. In the BD46 system, the B star BD + 46° 3474 is located at the center of the bright nebula, while the Be star BD + 46° 3471 is $\sim$ 3.5 pc away, as labeled by the thick small arrow. Likewise, in the V921 Sco system, the big bright nebula centers on an HII region, while the thick small arrow points to the Be star V921 Sco at $\sim$ 2pc away.

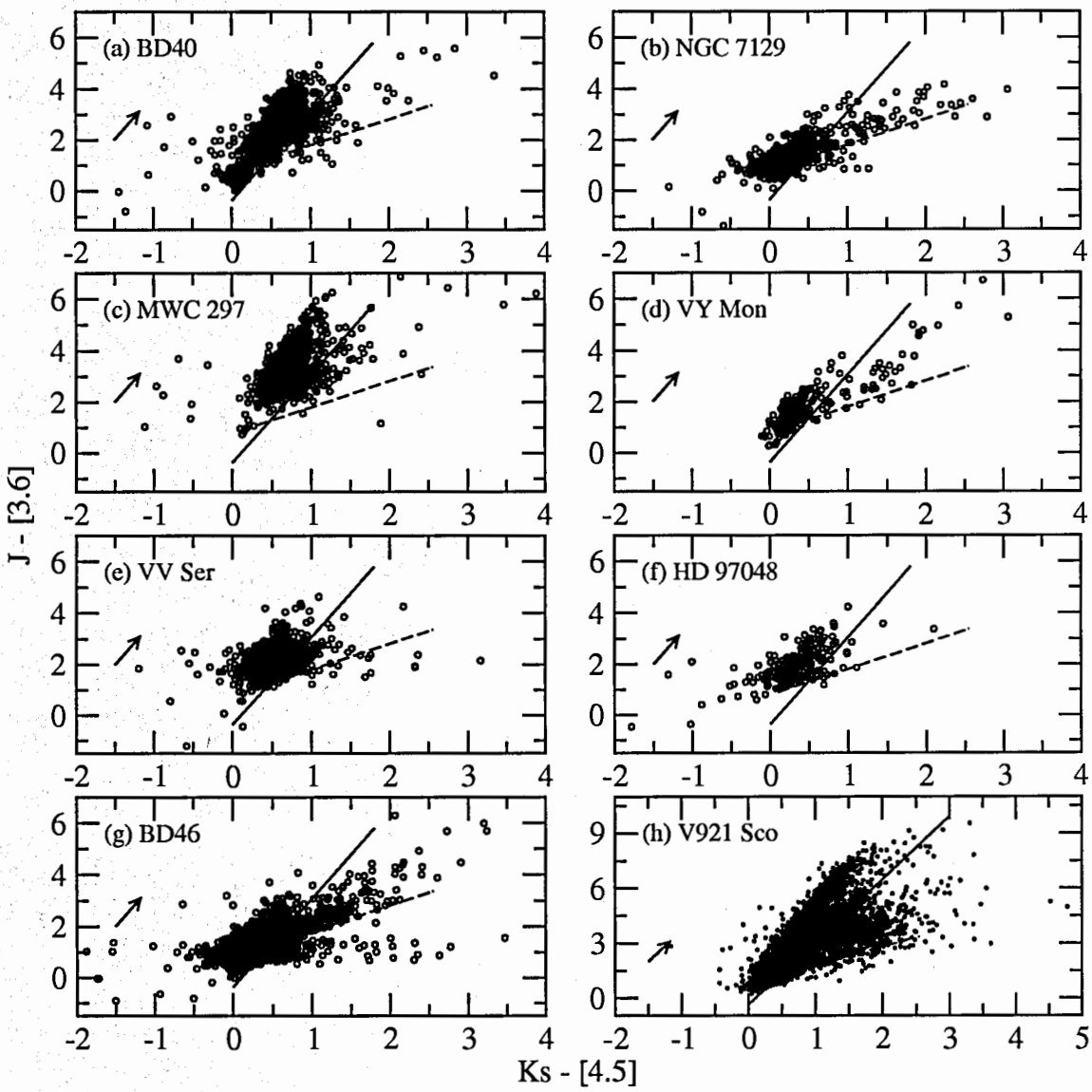

Figure 4.2 The color-color diagrams of sampled clusters. The solid lines are Equation (3.1) and the dashed lines are the YSO loci (Equation (3.3)). Stars that are located at the right side of the solid lines are identified as YSO candidates. The extinction vector for $A_V = 5$ is drawn as the arrow in each panel.

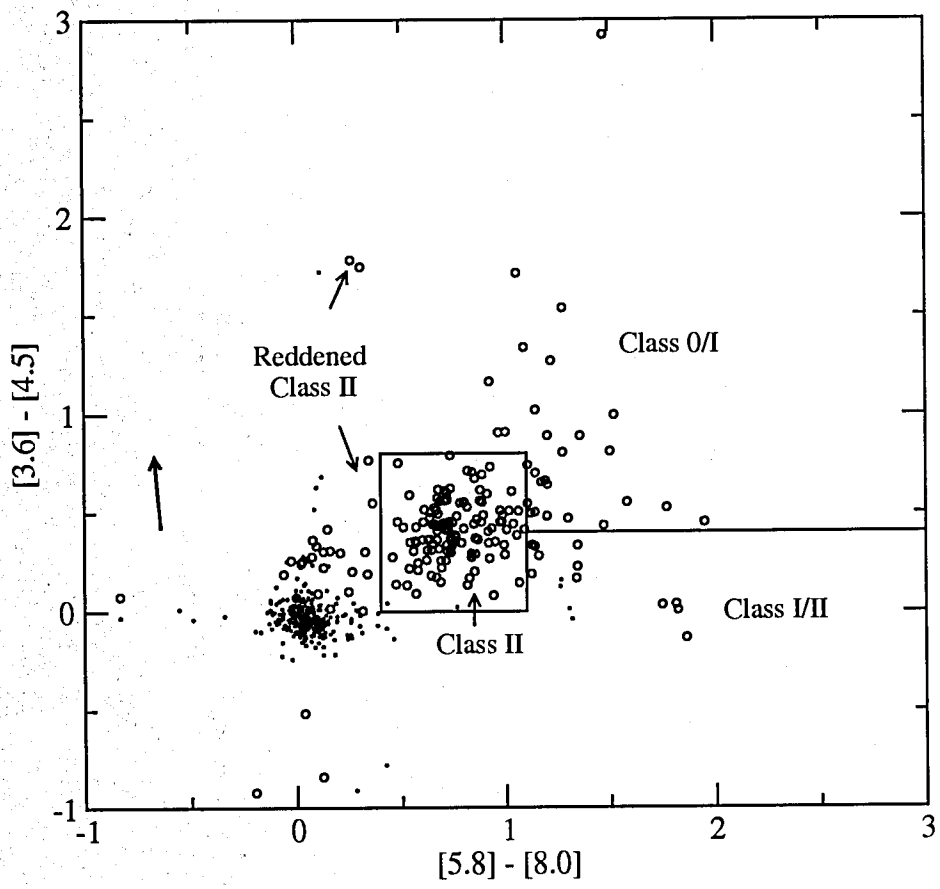

Figure 4.3 The IRAC color-color diagram for those YSO candidates with identifications at all four IRAC bands. The thick vector on the left shows A_V =30. The small dot and circle label the normal stars and YSO candidates, respectively. The labels for different types of protostars are based on the classification in Megeath et al. (2004). Only 18 out of 322 (6 %) YSO candidates are located in the regime of normal stars.

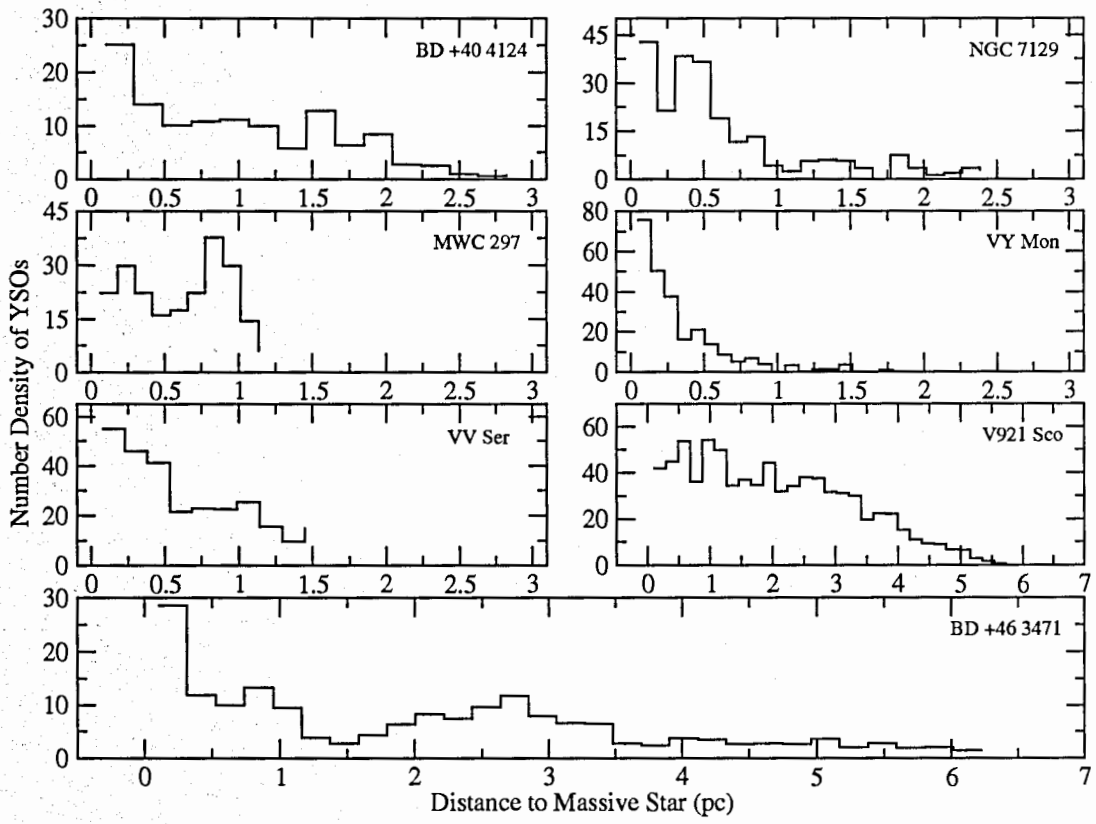

Figure 4.4 The number density of YSO candidates vs. the distance to massive stars shown at the up-right corner of each panel. See texts in this chapter for the definition of the number density and Table 2.1 for the position for each massive star. The small cluster around HD 97048 is not shown because there are too few stars to be plotted.

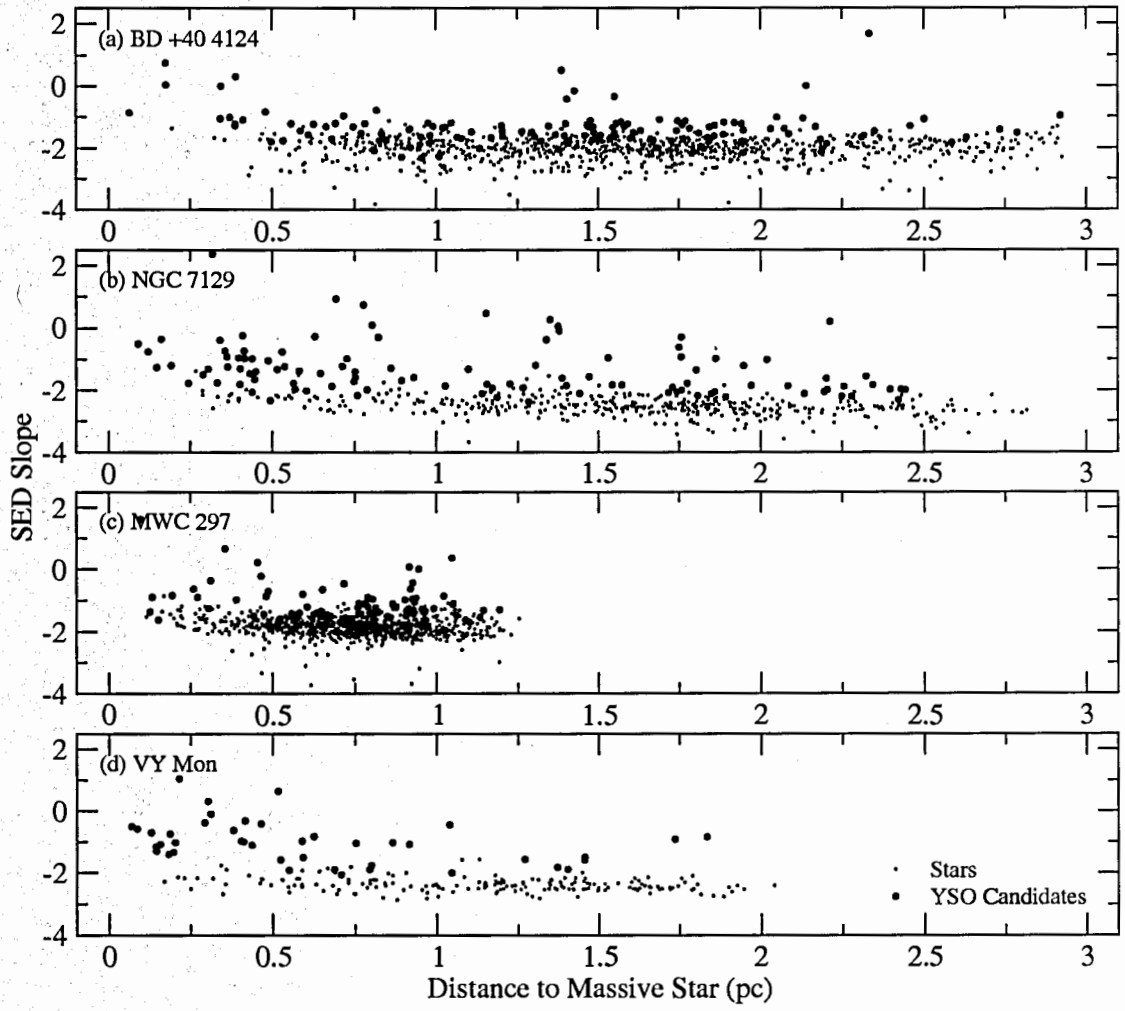

Figure 4.5 The SED slopes of YSO candidates vs. the distance to massive stars. The cluster of YSO candidates around the HAeBes tend to show larger SED slopes compared to those distributed outside the cluster.

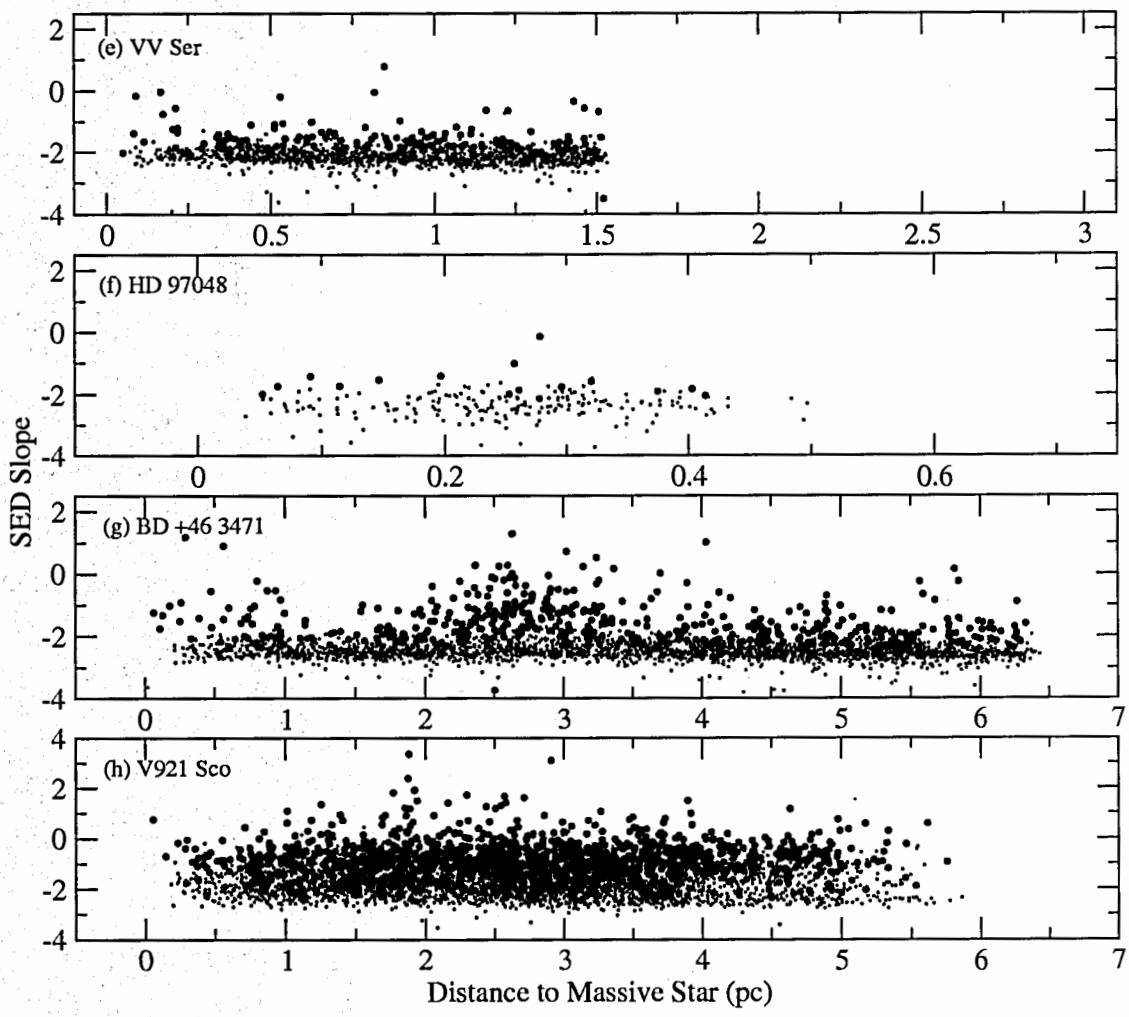

Figure 4.6 Same as Figure 4.5.

Chapter 5

The Laboratory of the MWC 1080 Cluster– Rule of the Massive Star: I. The Cloud

The MWC 1080 system is an intermediate-size stellar cluster embedded within the dark cloud LDN 1238 (Lynds 1962) at 2.2 kpc (Canto et al. 1984; Ábrahám et al. 2000). The most luminous star, MWC 1080 (V628 Cas), has been classified as a B0e star (Cohen & Kuhi 1979) with 20.6 $M_\odot$, 10^4 $L_\odot$ (Hillenbrand et al. 1992, 1995a), and a flat optically thick circumstellar disk (Hillenbrand Class I object for Herbig Ae/Be stars). Within 0.2 pc, it is surrounded by at least 15 stars presenting large near infrared excesses (Hillenbrand et al. 1995a). In addition to infrared excesses, the discoveries of molecular outflows, a P-Cygni feature in the Hα line, and several nearby HH objects, also indicate active accretion and thus the youthfulness of this system ($<$ 1 Myr) (Fuente et al. 1998a; Finkenzeller & Mundt 1984; Poetzel et al. 1992; Yoshida et al. 1992). Levreault (1988) estimates an outflow age of 2.2 $\times$ 10^5 yrs. Thus, the age of this system is $\sim$ 0.1 - 1 Myr. Single-dish maps of CO, ^{13}CO, C^{18}O, and CS also show that this group is associated with more than 1000 $M_\odot$ of molecular material within 1 pc (Hillenbrand et al. 1995a) and $\sim$ 10 $M_\odot$ within 0.08 pc (Fuente et al. 2002). Judged by the age of MWC 1080, this system is actually young enough to still have molecular gas and forming stars but also old enough to have shown the influence of MWC 1080– the natal gas is dispersing. Therefore, it provides a valuable system to study the effects of massive star on its cloud and low-mass siblings.

In the following two chapters, I carry out a thorough inspection of this system by observing the dense molecular gas, dust, and young stars around MWC 1080 and studying their physical conditions. The submillimeter and millimeter observations probing dense molecular gas and dust continuum will be presented in this chapter, while the infrared observations detecting young stars within 0.25 pc radius will be shown in the next chapter.

The majority of this chapter was published as "Dense Molecular Gas In A Young Cluster Around MWC 1080– Rule Of The Massive Star", Wang et al., 2008, ApJ, 673, 315.

5.1 BIMA and SCUBA Observations

MWC 1080 was observed using the line transitions CS $J = 2 \rightarrow 1$, ^{13}CO $J = 1 \rightarrow 0$, and C^{18}O $J = 1 \rightarrow 0$ with the 10-element Berkeley Illinois Maryland Association (BIMA) Array (Welch et al. 1996). BIMA's high angular resolution can probe the dense gas and dust in this young stellar cluster on spatial scales of 1000's to 10,000's of AU. These molecular transitions are typical tracers for dense gas due to their high critical densities ($n \sim 10^4 - 10^6$ cm^{-3}), which helps reveal star-forming clumps and further probe the kinematics and physical conditions in the system.

The CS $J = 2 \rightarrow 1$ ($\nu = 97.981$ GHz) observations in C and B array configurations were obtained in October and December 2003. The correlator was configured with the line window of a velocity range of 76 km s^{-1} with 0.3 km s^{-1} per channel, and two 600 MHz bands for continuum. The system temperatures during the observations ranged from 150 - 700 K. The ^{13}CO $J = 1 \rightarrow 0$ ($\nu = 110.201$ GHz) and C^{18}O $J = 1 \rightarrow 0$ ($\nu = 109.782$ GHz) observations in B and C array configurations were obtained in March and April 2004. The correlator was configured with the line window of a velocity range of 135 km s^{-1} with 1.0 km s^{-1} per channel, and two 150 MHz bands for continuum. The system temperatures during the observations ranged from 230 - 1000 K.

The data were reduced with the MIRIAD package (Sault et al. 1995) and mapped using two array configurations with various u, v weighting schemes to stress structures on spatial scales from $2''$ to $9''$.

I also obtained a continuum submillimeter map of MWC 1080 at $\lambda = 850$ μm from the archive data of the Submillimeter Common User Bolometer Array (SCUBA) instrument on the James Clerk Maxwell Telescope (JCMT).

5.2 The Morphology of Dense Gas around MWC 1080

The BIMA interferometry data provide the highest resolution observations to date, revealing the dense gas in this cluster. I have weighted the data to probe the structures with spatial scales of $2''$ - $9''$ for CS, ^{13}CO, and C^{18}O. These sizes correspond to spatial resolutions roughly from 20000 AU down to 4000 AU, which is a good scale of probing low-mass star forming clumps (e.g. Looney et al. 2000).

5.2.1 The Distribution of Dense Gas

The left portion of Figure 5.1 plots the velocity-integrated CS contours overlaid on an K′-band adaptive optics observation from the 3.6m CFHT of the core stellar population (this observation is presented in Ch. 6). The right portion zooms into the core with this $\sim 0.1''$ resolution K′-band image (Ch. 6), which illustrates not only the distribution of cluster members but also the morphology of a reflection nebulae with a hourglass structure at the NW-SE direction (called the hourglass axis). This Hokupa'a 36 (Graves et al. 1998) adaptive-optics near-infrared (JHK′) observation and the photometry of cluster members will be presented in Ch. 6. The reflected light results from the existence of dense dust whose surface is illuminated by the UV radiation from MWC 1080.

The CS map shows two distinct branches of emission (Figure 5.1), which I call East and West for the left and right branch, respectively. Figure 5.1 shows that the distribution of CS emission is clearly aligned with the obscuring and scattering dust seen in the near-infrared map. This suggests the existence of a previous bipolar outflow that cleaned out the natal material along the direction perpendicular to the hourglass axis (the outflow axis), and helped clear the view to the stellar population along this direction. However, the CS emission is only associated with the upper part of the dense dust, revealing only the upper half of the cavity structure; the molecular gas is denser in the upper part than the lower part.

Moreover, the ^{13}CO map also supports the suggestion of bipolar outflows by revealing a nearly complete biconical cavity around MWC 1080 (see Figure 5.2). Figure 5.2 plots the velocity-integrated ^{13}CO and C^{18}O contours as well as the $\lambda = 850$ μm and $\lambda = 3$ mm dust continuum. The ^{13}CO morphology also gives an lower limit of the estimation for the outflow cavity with ~ 0.3 and 0.05 pc for the semimajor and semiminor axis and $\sim 45°$ position angle. This is just a lower limit because possible inclination or projection effects have not been taken into account. Fuente et al. (1998a, 2002) investigates the evolution of dense gas dispersal around HAeBes by presenting IRAM single-dish ^{13}CO and CS observations. They propose an evolutionary sequence from stars that are still embedded within dense clumps and associated with bipolar outflows (Type I) to stars that have dispersed their natal clouds and formed cavities (Type III). MWC 1080 is shown to be their Type II system. Our high spatial-resolution observations further show that although this system is

still young, age < 1 Myr, the bipolar outflows in the MWC 1080 system has already constructed a small cavity, which is revealed for the first time. The size of this cavity is much smaller, compared to the cavities seen in older systems, such as HD 200775, a HAeBe with age of 8 Myr and a cavity of size ~ 1.5 pc $\times$ 0.8 pc (Fuente et al. 1998b). This might suggest that the bipolar outflow activity around MWC 1080 is still an ongoing process that will form a larger cavity.

From Figure 5.2, the dust morphology at $\lambda = 850$ μm is similar to the morphology of dense gas, which infers that the dense gas traces well the dust around MWC 1080. The high resolution of the $\lambda = 3$ mm continuum BIMA map reveals five dust clumps, which are consistent with dense gas distribution as well.

In addition to the morphology, more information, such as the clumpiness, kinematics and physical conditions inside this system, can be further investigated by extracting the mass and velocity distribution of dense gas. Studying the clumpiness of a molecular cloud is essential as it is usually closely related to the fragmentation and collapsing of molecular cores inside the cloud, which provides valuable insights to the ongoing star-forming activities in the system. On the other hand, the kinematics of gas and physical conditions reveal the natal environment where stars were born. As CS traces a denser region than ^{13}CO, I mainly use CS to examine the clumpiness of dense gas, and use both CS and ^{13}CO to reveal the kinematics and physical conditions in this system.

5.2.2 Clumpiness of Dense Gas

Clumpiness is always observed in molecular clouds. This is not surprising as a star forms through collapsing the natal cloud after reaching certain collapsing criteria. Therefore, local fragmentation and further clumping are naturally two typical characteristics in star forming clouds. With the ability of interferometric observations to peer into dense layers of the molecular cloud, I can study how clumpy the dense gas is and its clump size, compared to those cores forming isolated stars.

A clump is defined as a local density enhancement, which results in a flux density enhancement observationally. A molecular cloud without clumpy structures will not show multiple local emission peaks in its map, no matter how small the probing scale, or beam size. On the other hand, if clumps exist in a molecular cloud, the number of local emission peaks will increase with decreasing scale, until all clumps have been picked up or some clumps are too weak to be detected. Therefore, high

resolution maps are essential to distinguish clumpy structures in the molecular clouds.

Figure 5.3 plots the CS contours at four different mapping scales with 8″, 4″, 3″, and 2″ beams. Fuente et al. (1998a) published the IRAM single-dish molecular line and continuum data of MWC 1080 and showed one emission peak near MWC 1080 in their ^{13}CO (1-0) and CS (3-2) maps with a 24 ″ and 16 ″ beam respectively, and two emission peaks around MWC 1080 at the 1.3 mm continuum map with a ∼11″ beam. By comparing these maps, more and more clumps are seen from their maps to Figure 5.3 here, and from Figure 5.3(a) to 5.3(c). This indicates that the dense gas around MWC 1080 is not a single big cloud centered on MWC 1080 but rather consists of small clumps, with clump sizes down to ∼ 3″ (6600 AU). However, there is not much difference in the clumpy structures between Figure 5.3(c) to Figure 5.3(d), which suggests that the u, v weights used in Figure 5.3(d) are less suitable to the majority of the dense gas. The reason is that the dense gas in Figure 5.3(d) is resolved out with the interferometer. Therefore, in this chapter, I will use Figure 5.3(c) to further identify clumps and study their physical properties.

The main purpose of identifying clumps is to obtain individual star-forming building blocks that are capable of forming one or multiple low-mass protostars, in order to investigate their physical condition, such as mass, velocity dispersion, spectral feature, etc., in each system. In order to identify clumps, I basically adapt the idea of the *Clumpfind* method (Williams et al. 1994) to: (1) select local peaks with fluxes above 3 σ in the velocity-integrated CS map (Figure 5.3(c)), (2) trace down to the half-maximum (HM) flux level of contours, which determines the sizes of clumps by fitting an ellipse, (3) assign the contour to the nearest peak once this contour is shared by more than one peak, (4) extract the spectrum and mass of each clump within the clump size, and (5) fit the extracted spectra with Gaussian to obtain the peak flux, peak velocity, and line width (FWHM). This is different from directly using three-dimension cubes because it can avoid some specific star forming features, such as a P-Cyg profile being mis-separated into two clumps.

Table 5.1 lists parameters of 32 identified clumps, including coordinates, sizes, and integrated fluxes (I_t). The a_o, b_o, PA_o, a, b, and PA are the observed and deconvolved sizes, including the major axis (a), minor axis (b), and the position angle (PA), respectively. I directly use the beam size as the upper limit of clumps with deconvolved sizes smaller than the beam size. The R_{cq} is $\sqrt{ab}/2$, the equivalent size assuming a spherical clump. The sizes of identified clumps range from ∼

4000 AU to 10000 AU. This is generally consistent with a typical system forming a single isolated low mass star (e.g., $\sim$ 5000 AU, Looney et al. 2003).

Moreover, the eccentricity of clumps, ϵ, derived by a and b, can be used to characterize the clump shape. From the derived values of projected eccentricity, we can see that not all clumps have circular morphology, especially for those closer to MWC 1080, which show somewhat elongated structures with larger eccentricities. In order to examine the spatial distribution of clump eccentricity, I plot the eccentricity vs. the distance to MWC 1080 (Figure 5.4(a)) and to the outflow axis (Figure 5.4(b)) for those resolved clumps. This plot shows that clumps closer to both the outflow axis and MWC 1080 tend to have larger projected eccentricities. This implies that clumps are more elongated when located closer to MWC 1080. This also suggests possible effects from outflows on the morphology of dense gas, especially modifying the shape of clumps.

5.3 The Kinematics of Dense Gas

I study the kinematics of the dense gas by investigating its velocity distribution. The spectral resolution of CS, ^{13}CO, and C^{18}O, observations are 0.299, 1.034, and 1.034 km s^{-1}, respectively, with V_{LSR} at 29.3 km s^{-1} (Hillenbrand et al. 1995a). As can be seen in Figure 5.1 and 5.2, CS and ^{13}CO trace more gas than C^{18}O does and CS traces gas with higher density than the other two transitions. I will use both CS and ^{13}CO to display the overall velocity distribution of dense gas and specifically use CS to examine the kinematics of identified clumps.

5.3.1 Overall Velocity Distribution

Figure 5.5 displays the integrated spectra of CS, ^{13}CO, and C^{18}O emission, and Figure 5.6 shows the integrated CS spectra of East and West. From Figure 5.5, we can see that all CS and C^{18}O and most ^{13}CO emission are blue-shifted, compared to the V_{LSR}. In addition, a double-peaked feature is seen in the integrated spectra of ^{13}CO and CS. Figure 5.6 shows that the spectrum of East is single-peaked with a broad linewidth, while West contains two components. Table 5.2 lists the Gaussian-fitted parameters of these integrated spectra. From all integrated spectra, a large velocity gradient of the dense gas is seen throughout the whole system; the separation of peak velocity between two components in West is as large as 3.3 km s^{-1}.

In order to reveal the velocity distribution and investigate the double-peaked feature, Figure 5.7 shows the position-velocity (PV) diagrams for East and West from CS and ^{13}CO maps. This is made by applying two cuts from south to north toward both portions, as the dense gas of two portions are elongated along the outflow axis. Interestingly, it shows that two components seen in the integrated CS spectrum of West are also spatially distinguishable– the blue and red component in the spectrum are related to the northern and southern part of the dense gas in West, respectively. Canto et al. (1984) also detected a double-peak feature on the spectrum of dense gas around MWC 1080, but explained it as the results from self-absorption due to poor spatial resolution. Our high-resolution interferometric data shows that this double-peaked feature actually comes from two sets of gas with different velocities. In addition to West, Figure 5.7 also shows that there is a systematic velocity gradient in East from -35 km s^{-1} (bluer, south) to -30 km s^{-1} (redder, north), especially seen in the ^{13}CO map. This gradient may result from an inclination of the outflow cavity, as the direction of the gradient is along the outflow axis.

Not only is there a velocity variation along the outflow axis, there is also a velocity gradient along the hourglass axis, which is perpendicular to the outflow axis. Figure 5.8 is the PV diagrams of the CS map with three cuts perpendicular to the outflow axis and moving away from MWC 1080. This also shows that the velocity dispersion along the farther cut is larger than that along the closer cut from MWC 1080. This is contrary to the idea that outflows or stellar winds from MWC 1080 contribute to the nonthermal motion, thus increase the velocity dispersion, of gas closer to MWC 1080.

5.3.2 Spectra of Identified CS Clumps

Figure 5.9 displays example spectra of the identified clumps. Table 5.3 lists Gaussian-fitted parameters of the clumps that can be fitted with Gaussian. A few of them show P-Cyg-like absorption; several of them contain two peaks, which might come from either self-absorption or a secondary component (another clump along the line of sight).

5.4 Estimating the Column Density and Mass of Dense Gas

Several methods have been used to estimate the column density from molecular emission, such as a direct estimation from individual transitions (Miao et al. 1995; Friedel 2005), the Large Velocity Gradient approximation (LVG, Goldreich & Kwan 1974), rotational temperature diagrams (RTD, e.g., Friedel 2005), etc. Since I only have individual transitions for each molecular species, I use a simple LTE method for all column density estimated in this chapter, and also use the LVG models for those CS clumps with fitted spectra for comparison.

5.4.1 LTE Approximation

By assuming LTE with an excitation temperature T_{ex}, small opacity and negligible background continuum contribution, the total column density from a single transition using an array can be derived by (e.g., Miao et al. 1995),

$$N = \frac{2.04 I C_\tau}{\theta_a \theta_b S \mu^2 \nu^3} Q e^{\frac{E_u}{T_{ex}}} \times 10^{20}\, cm^{-2}. \tag{5.1}$$

I is the total integrated intensity in Jy beam^{-1} km s^{-1}, θ_a and θ_b are the FWHM sizes of beams in arcseconds, S, μ^2, ν, Q, and E_u are the line strength, dipole moment in Debyes, line frequency in GHz, partition function, and energy in K of the upper state, respectively (Table 5.4). I use the deconvolved source sizes, a and b, as θ_a and θ_b here. C_τ is the opacity correction factor (Goldsmith & Langer 1999),

$$C_\tau = \frac{\tau}{1 - e^{-\tau}}.$$

The optical depth, τ, can be derived by (Rohlfs & Wilson 2000),

$$\tau = -ln[1 - \frac{T_{MB}}{J(T_{ex}) - J(2.73)}],$$

where T_{MB} is the main beam brightness from observations and J(T) is given by $\frac{h\mu}{k} \frac{1}{e^{h\mu/kT} - 1}$. Table 5.1 lists some of these parameters for CS(2-1), ^{13}CO(1-0), and C^{18}O(1-0) (Rohlfs & Wilson 2000).

With estimated column density, mass can be obtained by assuming the abundance ratio to H_2, X_{CS}, $X_{^{13}CO}$, and $X_{C^{18}O} = 10^{-9}$, 1.26×10^6, and 1.7×10^{-7}, respectively (Rohlfs & Wilson 2000).

An excitation temperature, T_{ex} = 20 K, is assumed, as a medium value often seen in dense cores forming massive stars (see review, Zinnecker & Yorke 2007). Therefore, the mass can be derived by

$$M = \mu m_H \frac{N}{X}(1.133abD^2), \tag{5.2}$$

where $\mu = 2.33$ is the mean molecular weight, m_H is the mass of a hydrogen atom, and D is the distance (= 2.2 kpc for MWC 1080; Canto et al. 1984; Ábrahám et al. 2000).

The estimated CS column densities and masses for CS clumps are listed in Table 5.5, labeled as M_{LTE}, along with the estimated optical depth. The masses of these clumps range from $\sim$ 1 - 10 $M_\odot$, with mean optical depth τ less than 1. I also estimate the maximum optical depth based on the peak emission of the CS map, which gives optical depth $\sim$ 1.2 in this system.

Using the same assumptions and eq. (5.1) and (5.2), the total masses of dense gas are also calculated. There are $\sim$ 800, 1000, and 900 $M_\odot$ for CS, ^{13}CO, and C^{18}O, respectively, within the area of 0.7 pc radius from the MWC 1080.

5.4.2 LVG Model

Another method, that is frequently used especially for optical thick lines, is the Large Velocity Gradient (LVG) approximation (Goldreich & Kwan 1974). This is a radiative transfer model that takes optical depths into accounts for photon transport. It basically assumes a cloud with a systematic velocity gradient with velocity increasing away from the cloud center, so that a local treatment for photon transport can be approximated. I also estimate column densities and masses of CS clumps based on the LVG model, in order to compare to the previous LTE calculation. I only apply LVG for those 14 CS clumps with well fitted spectral information from Table 5.3.

I use the *lvg* task in MIRIAD to generate grids of the LVG model with kinetic temperatures of 10 - 30 K, number densities of 10^4-10^8 cm^{-3}, and column densities of 10^{13}-10^{15} cm^{-2}. By using these grids to fit the observed brightness temperature, a range of CS column density can be found that can produce the observed emission. I further narrow the obtained range of CS column density by assuming the optical depth $\tau \lesssim 2$. As there is a lack of observations of NH_3 to further constraint the kinetic temperature, I simply use the range of 10 - 30 K, which is typically used for both low-

mass and massive star forming regions. The derived column densities and masses of CS clumps are listed in the Table 5.5.

I also compare the estimation of M_{LTE} and M_{LVG} for these clumps. All clumps, except clumps A2 and A4, show a roughly good agreement between the derived M_{LTE} and M_{LVG}. This consistency suggests that most CS clumps are under good LTE approximation with small opacity. Clumps A2 and A4 have the brightest peak emission. The reason why the LVG model gives much larger column density than the LTE approximation is that there is either a larger opacity or a higher temperature inside these two clumps. Large opacity will give a larger column density in the LTE approximation; while higher temperature than 30 K will allow smaller column density in the LVG model to produce lines with such strong intensity. Both are reasonable explanations, especially the temperature in these two clumps is likely higher than usual, as they are located very close to the source of strong UV radiation, MWC 1080. In this chapter, I will use the M_{LTE} for further discussion.

5.4.3 Virial Mass

With the estimated masses and the velocity dispersion of clumps, I can further study the virial condition inside each clump by comparing clump mass with the virial mass, M_{vir}. M_{vir} is the mass when the system is in virial equilibrium, when the time average over the kinetic energy is equal to half of the potential energy. In this situation, the system is gravitationally bound.

I assume a spherical symmetric clump with total mass M, radius R, and a density profile, $\rho(r) = \rho_0 r^{-\alpha}$, where ρ_0 is the central density and r is the radial distance from the clump center. Therefore,

$$M_{vir} = \frac{5-2\alpha}{3-\alpha}\frac{3R}{G}\frac{\Delta V^2}{8ln2}, \tag{5.3}$$

where $\alpha \neq 3$. Either uniform density or isothermal condition is often assumed while deriving the virial mass of a cloud. In these two cases,

$$M_{vir} = \frac{5}{3}\frac{3R}{G}\frac{\Delta V^2}{8ln2} \tag{5.4}$$

for uniform density, and,

$$M_{vir} = \frac{3R}{G}\frac{\Delta V^2}{8ln2} \tag{5.5}$$

for the isothermal cloud with density $\rho(r) = \rho_0 r^{-2}$.

In order to understand the density profile in this system, I investigate the relation between the total mass and size of CS clumps, by plotting M_{LTE} and R_{eq} (Figure 5.10), as used in Saito et al. (2006). I obtain a linear relation between these parameters via least-square fittings,

$$logM_{LTE}(M_\odot) = (0.87 \pm 0.32) logR_{eq}(pc) + (1.82 \pm 0.67), \tag{5.6}$$

with $\chi^2_r = 1.35$. This assumes that all clumps in this system around MWC 1080 have the same density structure. Since $\rho(r) = \rho_0 r^{-\alpha}$, which gives $M = \frac{4\pi\rho_0}{3-\alpha} R^{3-\alpha}$, then $\rho_0 = 4.57 \pm 1.69$ $M_\odot$ pc^{-3} and $\alpha = 2.13 \pm 0.32$ are obtained. Therefore, in this case

$$M_{vir} \sim \frac{3R}{G} \frac{\Delta V^2}{8ln2}, \tag{5.7}$$

shows that these systems are consistent with a standard isothermal sphere density (Shu 1977).

Given R_{eq} and FWHM from Table 5.1 and 5.3 as R and ΔV^2, M_{vir} is calculated and listed in Table 5.5. M_{vir} ranges from $\sim$ 1 - 10 $M_\odot$. By comparing M_{vir} with M_{LTE}, I find that the M_{vir} is $\sim$ 0.4 - 2 times the M_{LTE}, except A8, C1, and C5, the farthest three clumps away from MWC 1080, which are 2 - 4 times larger than M_{LTE}. In general, I can conclude that the virial mass is similar to the clump mass, as the mass estimation usually has an uncertainty to an order of 2. This is similar to low-mass star forming cores, rather than massive cores (e.g., Saito et al. 2006).

5.5 Discussion

This chapter presents high resolution data for dense gas in the cluster environment around the HAeBe star MWC 1080. The CS transition is especially used to peer into the dense core region. Freeze-out depletion of CS or CO onto dust grains would affect my results. However, molecular depletion mostly occurs in colder cores. For example, CS and CO are often seen to freeze-out onto dust grains in starless cores, which have lower average temperatures, $\sim$ 10 K (see review, di Francesco et al. 2007).

With high resolution, the importance of this study is being able to reveal the physical conditions

and examine the sub-structures (i.e. clumps, that may be forming single low-mass cluster members) within this cluster-forming cloud, and distinguish the effects of MWC 1080 and its outflows from the initial cloud environment. I will focus on discussing the effects from MWC 1080 on its natal cloud by characterizing the dense gas, its dispersal history, and star-forming clumps in this cluster. To best study star formation in cluster environments would require a large sample of objects like MWC 1080; however, these data still provide valuable insights into such systems.

5.5.1 Gas Removal in Clusters

Outflows are the primary sources to remove the natal material during the formation of stars, in addition to stellar winds and stellar radiation in the core of starburst clusters. However, the gas removal process via outflows in clusters has not been clearly characterized. As there are both high-mass and low-mass members forming in a cluster, the gas removal process might be different from that in a single star forming system. Especially, does the most massive star still dominate the outflows that results in similar gas removal processes as seen from an isolated star? What is the role of low-mass cluster members in the strength and collimation of outflows?

In fact, the existence of a bipolar outflow in this cluster around MWC 1080 has been suggested based on its blue and red components on CO spectra in previous single-dish studies (e.g., Canto et al. 1984; Yoshida et al. 1991). However, due to poor angular resolution of single-dish observations, the outflow properties, such as the direction of the outflow axis, have not been well characterized. From my data, a biconical cavity is distinctly revealed around the most massive star in this system, MWC 1080, suggesting that the bipolar outflow has been dominated by MWC 1080. This also implies evidence of the gas removal by outflows in clusters. With the observed outflow cavity, the outflow axis is also clearly defined to have a PA of 45 degree.

Our data also show that this outflow cavity has a size of 0.3 $\times$ 0.05 pc. This roughly gives an opening angle of 20 degree and a collimation factor of 3. This also means that the outflow activity has begun and formed a small cavity at the age $<$ 1 Myrs for a HAeBe star like MWC 1080. However, gas removal via outflows is still an ongoing process in this system, as a larger outflow cavity has been seen in a similar but older system (HD 200775, 8 Myrs, Fuente et al. 1998b). A future ^{12}CO high resolution observation will be helpful to confirm the ongoing outflow activity in

this system, as ^{12}CO can trace low density outflow gas. Assuming a homogeneous mass distribution of gas in the initial natal cloud and an initial mass density the same as the remaining gas, I can estimate that there was $\sim$ 1000 $M_\odot$ of gas in the cavity before outflows removed it. Therefore, an outflow mass loss rate $> 10^{-3}$ $M_\odot$/yr is required to form this cavity, either assuming a outflow age of $\sim$ 0.2 Myrs (Levreault 1988) or an age $<$ 1 Myrs (Fuente et al. 1998a). This value is higher than the typical mass loss rate of outflows from a single OB star ($10^{-3} - 10^{-4}$ $M_\odot$/yr). In fact, previous CO observations, which trace outflow gas at larger scale than this study, have estimated an outflow mass loss rate of $\sim 10^{-4}$ $M_\odot$/yr (e.g. Yoshida et al. 1991; Canto et al. 1984; Levreault 1988). One explanation of possible higher mass loss rate for CS gas is that the outflows from other cluster members are strong enough to strengthen the overall effects, but not enough to change the outflow direction, at the scale of this study. Another possibility is that the remaining gas does not just include the natal material but also the swept-up gas by outflows, so the mass loss rate is overestimated.

In order to clarify whether the observed dense gas is the remaining gas from the initial cluster-forming cloud or the swept-up gas by outflows, I further inspect the possible non-thermal contribution from outflows in dense gas next.

5.5.2 Non-thermal Contributions in Dense Gas

Molecular clouds, except for single star-forming prestellar cores, are generally observed to have broader linewidths than those caused by the thermal motion from their thermal temperatures. This is suggested to be resulting from the presence of turbulence (see review by Mac Low & Klessen 2004). Is this also true for single star-forming clumps in a cluster around an intermediate- to high-mass star, like the MWC 1080 system? What is the role of the cluster environment in the kinematics of dense gas and clumps within one cluster-forming cloud?

Our data show that the linewidth of clumps range from 0.85 to 2.48 km s^{-1}, which is much larger than 0.63 km s^{-1}, the linewidth of thermal broadening at 20 K. If only thermal motion contributes to the linewidth, the kinematic temperatures of these clumps would range from 36 - 310 K. This is unlikely, except for those clumps very close to MWC 1080, which heats its surroundings via UV radiation. Therefore, my results suggest that most gas in this system has a non-thermal

contribution to their kinetic motions. However, what contributes to these non-thermal motions? Initial turbulence, outflows from forming stars, and stellar winds from massive stars are possible candidates.

Initial turbulence is the general non-thermal random motion caused by turbulence in the molecular cloud before forming stars. Larson (1979, 1981) found the linewidth-size relation for molecular clouds with different scales. This relation indicates that there is a power-law relation between the velocity dispersion of molecular clouds and cloud size. Caselli & Myers (1995) further suggested that the non-thermal linewidth-size relation follows different power-law trends for low-mass and massive cores. In other words, non-thermal motion still dominates at small scales for massive clumps, while low-mass clumps show only thermal motions at these scales. Nevertheless, there exist non-thermal components in the kinematics of molecular clouds, which provides the initial turbulence. Based on my data, I roughly estimate that the radius of this cluster-forming cloud is $\sim$ 0.7 pc. This gives an estimation for the initial turbulence with linewidth of $\sim$ 1 km s^{-1} in this system, assuming the linewidth-size relation from Larson (1981). This value is smaller than the linewidth from my integrated spectra (Table 5.3), which implies that the initial turbulence may not be the only contributor to the non-thermal motion in this system.

In order to confirm more carefully whether there are extra contributors to broaden the linewidth of clumps, I plot the linewidth-size relation for identified clumps in Figure 5.11, compared to Caselli & Myers (1995). Caselli & Myers (1995) shows the nonthermal linewidth-size relations for massive and low-mass cores. Therefore, in this figure, I add the thermal components to their relations with thermal temperature of 18 K and 10 K for massive (solid line) and low-mass (dashed line) cores, respectively, as assumed in Caselli & Myers (1995). The dotted line indicates the thermal motion of 20 K, which is well below the linewidths of all clumps. It also shows that there is either a flat relation or no correlation between the linewidth and the clump size. When using the relation from Caselli & Myers (1995) as expected initial turbulence contribution, this figure suggests that extra contributions dominate over the initial turbulence and affect more the smaller clumps. Not only the relation, but the linewidth values of identified clumps are also overall larger than those in Caselli & Myers (1995). In addition, Figure 5.11 also plots the relation between the linewidth and the LTE mass of clumps, compared to the result shown in Larson (1981). It shows that the low-mass

clumps seem to deviate more from Larson's relation. This indicates that the lower-mass clumps are possibly affected more, which implies that the extra contributor to the non-thermal motions may come from a common source outside these clumps, instead of heated contribution from embedded forming stars inside individual clumps.

Both outflows or stellar winds can contribute to the observed non-thermal components of linewidth. From the Figure 5.11, those extra contributors need to broaden the linewidth by $\sim$ 1-1.5 km s^{-1}. Furthermore, Figure 5.12 plots the relations for the linewidth and mass vs. the distance to MWC 1080. From the linewidth-distance relation, no correlation is shown. As outflows or stellar winds from MWC 1080 are possible contributors to the non-thermal motions of natal gas, the affected linewidth are expected to be broader for clumps closer to MWC 1080. Therefore, this plot possibly suggests that there is less initial turbulence deep inside the core region of this cluster-forming cloud. Besides, it is shown in the linewidth-mass relation that more massive clumps form closer to MWC 1080, which is or is close to the center of this cluster-forming cloud.

In short, the kinematics of dense gas in this cluster has been effectively modified by outputs from forming stars, such as outflows and stellar winds, instead of still being sustained by the initial turbulence. This further suggests that the observed hourglass dense gas is much more likely to be swept-up gas.

5.5.3 Implications from the Dense Gas Morphology

Who forms first in a cluster– massive or low-mass stars? This has been an fundamental but difficult question in the study of cluster formation, because highly embedded nature of protoclusters, where massive star forms, have prevented us from catching the earliest stage of the formation of low-mass cluster members. However, clarifying this question is essential as it helps understand the star forming environment in clusters and after all most low-mass stars actually form in such cluster environments. This also plays an important role in studying massive star formation as massive stars often form in clusters along with many low-mass stars.

Our results have suggested that the observed molecular lines most likely trace the swept-up gas on the outflow cavity wall, instead of outflows or remaining gas with initial density. The kinematics of the swept-up gas has also been effectively modified by outflows or stellar winds from MWC 1080.

The biconical cavity implies a domination of MWC 1080 and also eliminates the contribution of other cluster members. In addition, Ch. 6 also presents that there are $\sim$ 50 low-mass stars within 0.3 pc radius around MWC 1080. Most of these stars are located inside the outflow cavity (also see Figure 5.1 and 5.2).

These results may imply that it is unlikely to form low-mass cluster members after MWC 1080 in this system. If low-mass cluster members form after MWC 1080 does, then the gas dispersal from MWC 1080 should eliminate the formation of low-mass cluster members along the outflow direction. Hence, the stellar density in the cavity should have been lower than observed, if these low-mass stars formed after MWC 1080.

However, one puzzle remains about the morphology– why does CS emission only trace the upper half of the outflow cavity? In other words, why is the gas in the upper part denser than the lower part? One explanation is an inhomogeneous distribution of initial natal gas; the gas is just denser in the upper side than the lower side. Another explanation is that this is due to the inclination of outflow cavity, as all CS emission is blue-shifted and a gradient has been seen in Figure 5.8. The asymmetry of the opening angle between both sides from the ^{13}CO map also may also result from the inclination.

5.5.4 Clumpiness of Dense Gas vs. Gas Dispersal History

As stars form, they disperse their natal material, so studying the morphology of molecular gas around newly forming stars has been very helpful to distinguish stars with different evolutionary stages (e.g., Fuente et al. 1998a, 2002). A star-forming cloud typically evolves from compact dense gas centered on the star, to dense gas with bipolar outflows, then finally to a cavity with little gas left. However, not only the natal molecular cloud, but the clumpiness of dense gas in the cloud may also be actively affected by the dispersal processes from the forming star. Therefore, the clumpiness of dense gas might be able to provide an alternative point of view to describe the evolutionary stages of star formation.

The clumpiness of dense gas can be defined as: (1) the fraction of mass inside clumps to total mass; or (2) the number density of clumps– number of clumps per projected area. The first definition is determined by the intrinsic star forming efficiency in the cloud and the degree of gas

dispersal; the second definition is determined by the intrinsic fragmentation in the cloud and the degree of gas dispersal. Both definitions depend on the gas dispersal history because the mass inside clumps decreases and the clumps disappear as stars form. Therefore, the clumpiness can actually be used to trace the evolutionary stages of the forming stars, assuming the same initial conditions in the cloud and similar star forming processes. This assumption is valid if I simply apply and compare the clumpiness to similar systems, for example, to clusters around HAeBes like MWC 1080. However, we have to keep in mind that the cloud's initial conditions may dominate the clumpiness, as different star or cluster forming mechanisms could result in various initial cloud conditions.

In this chapter, I will only use the second definition to discuss the clumpiness. This is because the true mass inside clumps can not be fully obtained and the first definition will be biased with the dependence of mapping scales, due to the limitation of interferometry. Looney et al. (2006b) identifies 16 clumps from another cluster around HAeBes including BD +40° 4124. Using the second definition, I find that the clumpiness in the BD +40° 4124 system is $\sim$ 1.6 times larger than that in the MWC 1080 system. This suggests that the dense gas seen in the BD +40° 4124 system is at a younger stage than that in the MWC 1080 system.

From the infrared SED classification (Hillenbrand et al. 1992), BD +40° 4124 and MWC 1080 are both classified as Group I objects, which have rising SED slopes. From the gas dispersal history (Fuente et al. 1998a, 2002), they are both associated with compact dense gas, which suggests a similar evolutionary stage. In addition, from the CS maps using high resolution interferometric observations (Figure 1 in Looney et al. 2006 for BD 40° +4124 and Figure 5.5(b) here), both systems show that the CS distributions are actually offset from the most massive stars– still at a similar evolutionary stage. Looney et al. (2006b) show that the dense gas is around other younger stars, not BD+40° 4124. The clumpiness discussed here suggests the youthfulness of dense gas in the BD +40° 4124 system and also shows that the dense gas in the MWC 1080 is dominated by MWC 1080, unlike the BD +40° 4124 system. Indeed, the clumpiness provides an alternative point of view to examine the evolutionary stages of young stars, other than the morphology of dense gas or the SEDs of young stars.

5.5.5 Dynamics of Clumps

Our data have shown that the mass of identified clumps ranges from $\sim$ 0.5 to 10 $M_{\odot}$, capable of forming low-mass stars, with equivalent radius from 0.01 to 0.04 pc. These clumps are, in general, more massive than protostellar cores with similar sizes. This suggests that clumps formed in a cluster environment tend to have higher densities, which is also shown in Saito et al. (2006).

In addition, all clumps are estimated to have masses similar to the virial masses, which suggests that they are close to being in virial equilibrium. Figure 5.13 compares the LTE mass and LVG mass vs. virial mass for all clumps. This figure shows that most clumps have masses within 2 times of their virial masses, which means that they are self-gravitational bound systems. This is usually seen in low-mass cores; but it is different from turbulent cores in massive star-forming regions (Saito et al. 2006), showing larger virial masses than LTE masses. This may be due to the external gas pressure helping support the turbulence (Saito et al. 2006). However, according to their Table 5.4, cores with LTE masses $<$ 10 $M_{\odot}$ are actually close to their virial masses, which is consistent with my results.

Nevertheless, clumps in the MWC 1080 system are self-gravitationally bound, similar to low-mass star-forming cores, but have a higher density like massive cores. This is not surprising as more mass is needed to bound clumps in order to overcome the non-thermal motions, which are contributed not only by initial turbulence but also inputs from massive stars, such as outflows and stellar winds. This does not necessary mean that they will form massive stars eventually, because they will experience stronger external gas removal, such as outflows from nearby massive stars, than those isolated star-forming cores. In fact, I can simply assume that the identified clumps are possible precursors of those NIR-identified low-mass cluster members (Paper II), that are revealed just because their surrounding gas is strongly dispersed by outflows from MWC 1080. This means that these clumps will indeed be likely forming low-mass stars.

In addition, from Sec. 5.3, I derive a density profile for the identified clumps, $\rho(r) \sim r^{-2.13\pm0.32}$. This is consistent with Saito et al. (2006), which shows a density profile of $\rho \sim r^{-1.9}$ for cores in massive star-forming regions. My results show that clumps in this system are consistent with the density profile of many protostellar collapse models (e.g., Tassis & Mouschovias 2005). Therefore, along with the fact that these clumps are gravitationally bound, the $\sim r^{-2}$ profile from my data

suggest that these clumps are likely collapsing protostellar cores.

I simply conclude that low-mass stars in the cluster environment like the MWC 1080 system tend to be formed in dense and turbulent cores, which are different from isolated low-mass star-forming cores but similar to massive cores. However, gas dispersal contribution from the massive cluster member prevents these dense and turbulent cores from forming massive stars, instead forming low-mass stars, which are also revealed earlier than isolated low-mass stars are. This indicates that massive stars in clusters do have effects on the formation of their low-mass cluster members– both help and hinder.

5.6 Summary

I present BIMA CS(2-1), ^{13}CO(1-0), C^{18}O(1-0), and 3mm continuum observations toward the young cluster around MWC 1080, which is a $\sim$ 20 $M_{\odot}$ massive star with the age $<$ 1 Myr. I summarize the results as follows.

- A biconical cavity, with size of 0.3 $\times$ 0.05 pc and $\sim$ 45° position angle, is revealed, which suggests the presence of bipolar outflows. The outflows are dominated by the MWC 1080, and effectively modifying the morphology of clumps.

- The observed molecular lines trace the swept-up gas on the cavity wall, instead of the initial natal material or the outflow gas.

- The observed gas is clumpy; 32 CS clumps are identified with mass ranging from 1 - 10 $M_{\odot}$. All clumps are approximated under the virial equilibrium, which suggests that they are gravitationally bound, and isothermal. This suggests that they are likely collapsing protostellar cores.

- The gas is mostly blue-shifted. I identify two distinct clouds with different velocities that were thought to be self-absorption. Velocity gradients have also been revealed suggesting an inclination of the outflow cavity and some effects from MWC 1080.

- Both overall gas and clumps show broader linewidths than thermal motion at 20 K. The non-thermal component is possibly contributed by outputs from MWC 1080, such as outflow

and stellar wind, in addition to the initial turbulence often seen in the molecular cloud. This suggests that the kinematics of dense gas has been affected by either outflow or stellar wind from MWC 1080; lower-mass clumps are more strongly effected from MWC 1080 than higher-mass clumps.

- Clumps in clusters have, in general, higher densities than isolated star-forming cores. This results from non-thermal contributions, such as outflows or stellar winds, from nearby forming massive star or stars. However, low-mass stars can still be forming from these clumps, because of the increased gas dispersal from MWC 1080. Therefore, low-mass cluster members tend to be formed in dense and turbulent cores, which are different from isolated low-mass star-forming cores.

In summary, my results show that in the cluster like MWC 1080 system, effects from the massive star dominate the star-forming environment in the cluster, in both kinematics and dynamics of the natal cloud and the formation of low-mass cluster members. However, more studies in similar systems like the MWC 1080 cluster are needed in the future, in order to systematically confirm the effects from massive stars.

Table 5.1. Parameters of Identified CS Clumps

Label	a_o "	b_o "	PA_o degree	a "	b "	PA degree	R_{eq} 10^{-2} pc	ε
A1	6.81±0.29	3.60±0.02	-73.65±0.07	5.85	1.33	-73.8	1.49±0.04	0.97±0.04
A2	11.77±1.37	3.88±0.09	69.30±0.04	11.26	1.85	69.1	2.43±0.16	0.98±0.01
A3	-	-	-	3.49	3.34	-67.6	1.82	-
A4	8.11±0.63	6.25±0.41	-36.87±1.91	7.33	5.25	-35.9	3.31±0.19	0.69±0.09
A5	-	-	-	3.49	3.34	-67.6	1.82	-
A6	6.75±0.77	4.95±0.13	-11.99±0.82	5.84	3.55	-10.7	2.42±0.16	0.79±0.09
A7	6.77±3.20	4.63±0.37	-7.57±1.78	5.87	3.08	-6.5	2.27±0.63	0.85±0.30
A8	6.10±2.24	4.13±0.34	44.68±3.82	5.09	2.24	43.7	1.80±0.42	0.89±0.23
A9	5.73±0.89	3.31±0.07	-81.44±0.32	3.49	3.34	-67.6	1.82	-
B1	4.25±0.09	2.74±0.01	-46.23±0.28	3.49	3.34	-67.6	1.82	-
B2	6.81±3.35	4.49±0.49	87.86±1.67	5.86	2.97	87.0	2.22±0.66	0.86±0.29
B3	6.95±1.13	4.43±0.17	-82.63±1.17	6.01	2.90	-83.2	2.23±0.22	0.87±0.08
B4	5.16±0.87	3.35±0.29	78.28±1.41	3.49	3.34	-67.6	1.82	-
B5	6.23±0.59	4.81±0.22	67.31±2.10	5.21	3.38	65.4	2.24±0.14	0.76±0.09
B6	6.98±3.60	3.72±0.11	0.47±0.40	6.12	1.33	1.1	1.52±0.45	0.97±0.17
B7	10.14±3.91	4.98±0.08	-19.60±0.19	9.55	3.62	-19.2	3.13±0.64	0.92±0.10
B8	4.99±0.26	4.09±0.09	72.30±2.06	3.63	2.25	68.7	1.52±0.06	0.78±0.06
B9	-	-	-	3.49	3.34	-67.6	1.82	-
B10	7.89±4.62	4.30±0.26	55.54±1.25	7.13	2.58	54.9	2.28±0.75	0.93±0.20
B11	7.03±2.73	3.26±0.09	-63.31±0.38	3.49	3.34	-67.6	1.82	-
B12	4.59±2.18	3.86±0.57	7.20±17.14	3.14	1.66	9.3	1.22±0.47	0.84±0.65
B13	6.65±3.71	4.29±0.37	26.21±2.56	5.75	2.50	26.1	2.02±0.66	0.90±0.30
B14	5.24±0.85	3.92±0.41	79.86±2.81	3.95	1.98	77.6	1.49±0.22	0.86±0.16
C1	-	-	-	3.49	3.34	-67.6	1.82	-
C2	-	-	-	3.49	3.34	-67.6	1.82	-
C3	-	-	-	3.49	3.34	-67.6	1.82	-
C4	-	-	-	3.49	3.34	-67.6	1.82	-
C5	5.49±0.19	4.01±0.05	-58.20±0.70	4.24	2.22	-57.5	1.63±0.04	0.85±0.02
D1	5.64±0.71	3.57±0.13	89.11±0.62	4.45	1.21	87.9	1.24±0.12	0.96±0.06
D2	6.36±0.97	4.76±0.29	-59.04±3.04	5.31	3.38	-58.5	2.26±0.23	0.77±0.13
D3	5.53±1.67	3.99±0.37	-40.14±5.56	4.31	2.13	-38.4	1.61±0.34	0.86±0.23
D4	4.57±1.09	3.88±0.55	-43.04±27.76	2.98	1.93	-38.7	1.28±0.29	0.76±0.38

Table 5.2. Fitted Parameters of CS Integrated Spectra

Label	Peak Jy	Velocity km/s	FWHM km/s
East	4.79±0.31	-31.68±0.06	1.87±0.14
West(N)	3.91±0.37	-30.83±0.08	1.52±0.19
West(S)	1.73±0.25	-34.13±0.26	3.24±0.69

Table 5.3. Spectral Fitting of CS Clumps

Label	Peak Jy	Velocity km/s	FWHM km/s
A1	0.44±0.05	-31.42±0.07	1.30±0.16
A2	1.77±0.10	-31.70±0.04	1.45±0.09
A3	0.68±0.08	-32.35±0.05	0.85±0.11
A4	1.60±0.09	-31.10±0.05	1.76±0.12
A5	0.45±0.05	-31.37±0.10	1.63±0.23
A6	0.64±0.06	-31.46±0.07	1.52±0.16
A7	0.54±0.05	-31.31±0.08	1.70±0.20
A8	0.20±0.04	-32.33±0.22	2.48±0.52
B2	0.36±0.07	-30.65±0.09	1.00±0.22
B3	0.44±0.08	-30.72±0.13	1.48±0.30
B6	0.50±0.04	-30.92±0.06	1.55±0.14
B7	0.68±0.06	-30.95±0.08	1.84±0.18
C1	0.28±0.04	-30.81±0.13	1.76±0.31
C5	0.35±0.05	-30.73±0.14	1.91±0.33

Table 5.4. Parameters of the Observed Molecular Lines

Molecular Name	Transition	ν GHz	$S\mu^2$ Debye	Q	E_u K
CS	J = 2 - 1	97.980968	7.71	0.86 T_{ex}[a]	7.0
^{13}CO	J = 1 - 0	110.201370	0.01	0.36 T_{ex}	5.3
$C^{18}O$	J = 1 - 0	109.782182	0.01	0.36 T_{ex}	5.3

[a]T_{ex} is the line excitation temperture.

References. — Rohlfs & Wilson (2000)

Table 5.5. Mass Estimation of CS Clumps

Label	I_t Jy beam^{-1} km s^{-1}	τ	M_{LTE} $M_\odot$	N_{lvg}(CS) 10^{13} cm^{-2}	M_{LVG} $M_\odot$	M_{vir} $M_\odot$
A1	1.755	0.46	3.59	3.43 - 5.56	0.64 - 1.04	2.38
A2	4.210	0.74	9.82	33.93	17.01	4.84
A3	1.631	0.34	3.15	3.64 - 5.91	1.02 - 1.65	1.24
A4	3.832	0.55	8.19	41.18	38.18	9.09
A5	1.557	0.38	3.08	4.30 - 6.98	1.20 - 1.95	4.57
A6	2.649	0.57	5.73	6.51 - 10.56	3.25 - 5.26	5.31
A7	2.582	0.57	5.58	5.71 - 9.28	2.48 - 4.03	6.20
A8	1.328	0.33	2.56	2.48 - 6.55	0.68 - 1.80	10.47
A9	0.930	0.30	1.76	-	-	-
B1	0.572	0.25	1.04	-	-	-
B2	1.042	0.21	1.88	2.07 - 3.36	0.87 - 1.41	2.11
B3	1.399	0.31	2.67	3.91 - 6.33	1.64 - 2.66	4.62
B4	0.799	0.26	1.49	-	-	-
B5	1.266	0.26	2.37	-	-	-
B6	2.012	0.48	4.17	5.21 - 8.46	1.02 - 1.66	3.47
B7	4.457	0.72	10.30	7.88 - 12.79	6.56 - 10.65	10.05
B8	1.582	0.49	3.28	-	-	-
B9	0.950	0.30	1.81	-	-	-
B10	1.516	0.30	2.88	-	-	-
B11	1.031	0.24	1.91	-	-	-
B12	0.703	0.22	1.28	-	-	-
B13	1.102	0.25	2.04	-	-	-
B14	0.810	0.24	1.55	-	-	-
C1	1.103	0.33	2.12	2.85 - 5.91	0.80 - 1.65	5.33
C2	1.444	0.33	2.77	-	-	-
C3	1.600	0.54	3.40	-	-	-
C4	1.200	0.50	2.50	-	-	-
C5	1.059	0.27	1.97	3.95 - 6.42	0.90 - 1.46	5.65
D1	0.914	0.23	1.66	-	-	-
D2	1.188	0.24	2.20	-	-	-
D3	0.878	0.24	1.61	-	-	-
D4	0.782	0.26	1.45	-	-	-

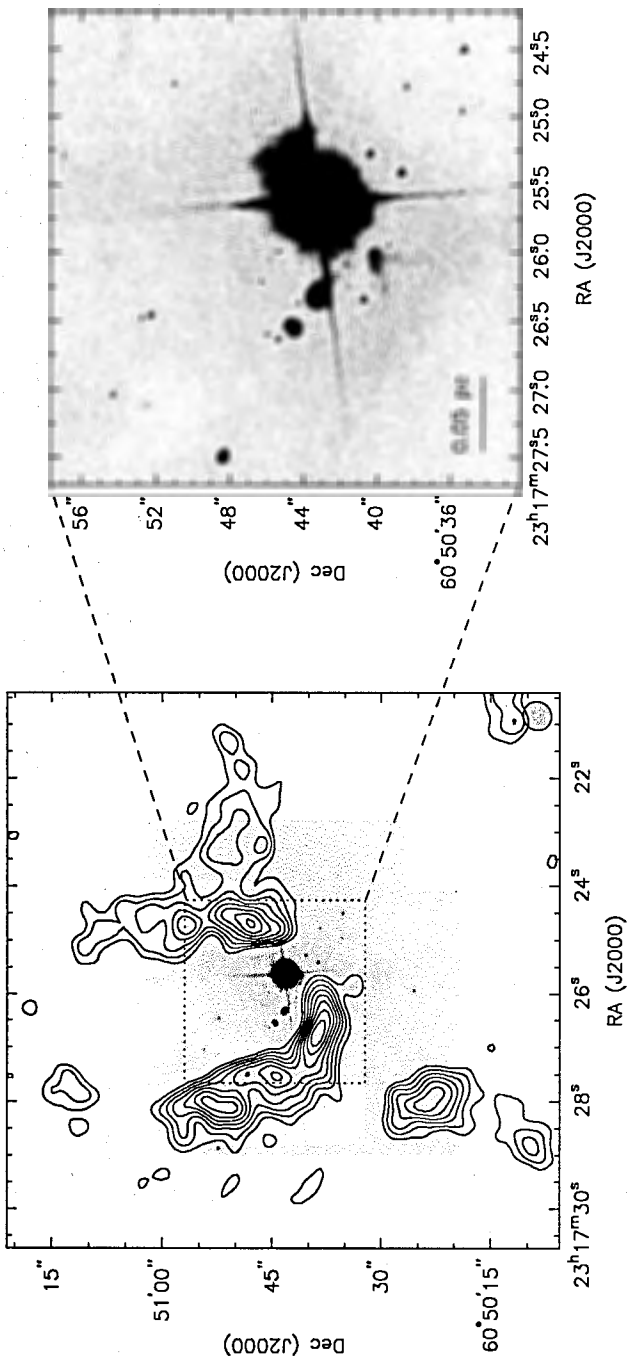

Figure 5.1 Left: CS(2-1) emission toward the MWC 1080 system overlaid on a small adaptive optics K′-band image taken from CFHT (Paper II). The noise is 0.14 Jy/beam km/s. The contours are linearly spaced from 2 to 10 times of noise. The beam, shown at the lower right hand corner, is 4.″04 × 3.″84 with a PA of -62°. Negative contours, mainly from resolved out large-scale emission, are not shown here in order to simplify the image. The dotted box indicated the zoomed field of the K′-band image (right) in order to show the distribution of young cluster members more clearly.

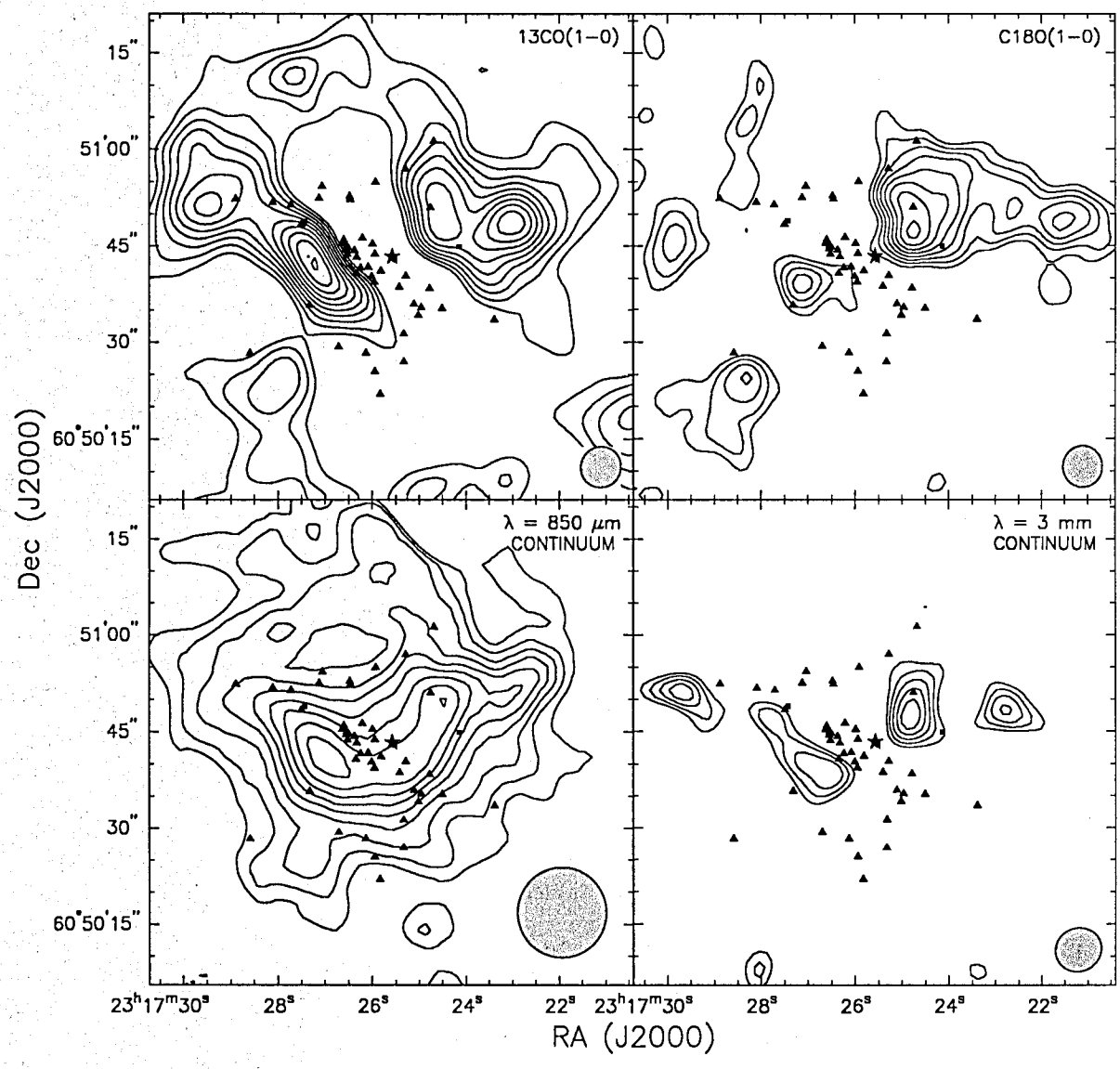

Figure 5.2 ^{13}CO, $C^{18}O$, and continuum emissions. For ^{13}CO, the noise is 0.3 Jy/beam km/s. The contours are linearly spaced from 2 to 20 times of noise. The beam is 6.″44 × 6.″28 with a PA of -51°. For $C^{18}O$, the noise is 0.12 Jy/beam km/s. The contours are linearly spaced from 2 to 10 times of noise. The beam is 6.″41 × 6.″34 with a PA of -13°. For 3 mm continuum map, the noise is 0.009 Jy/beam km/s. The contours are linearly spaced from 2 to 6 times of noise. The beam is 7.″36 × 6.″74 with a PA of -70°. Beams are shown at the lower right hand corner of each panel. The star symbols indicate the location of MWC 1080, and the triangle symbols indicate the NIR-identified cluster members from Paper II.

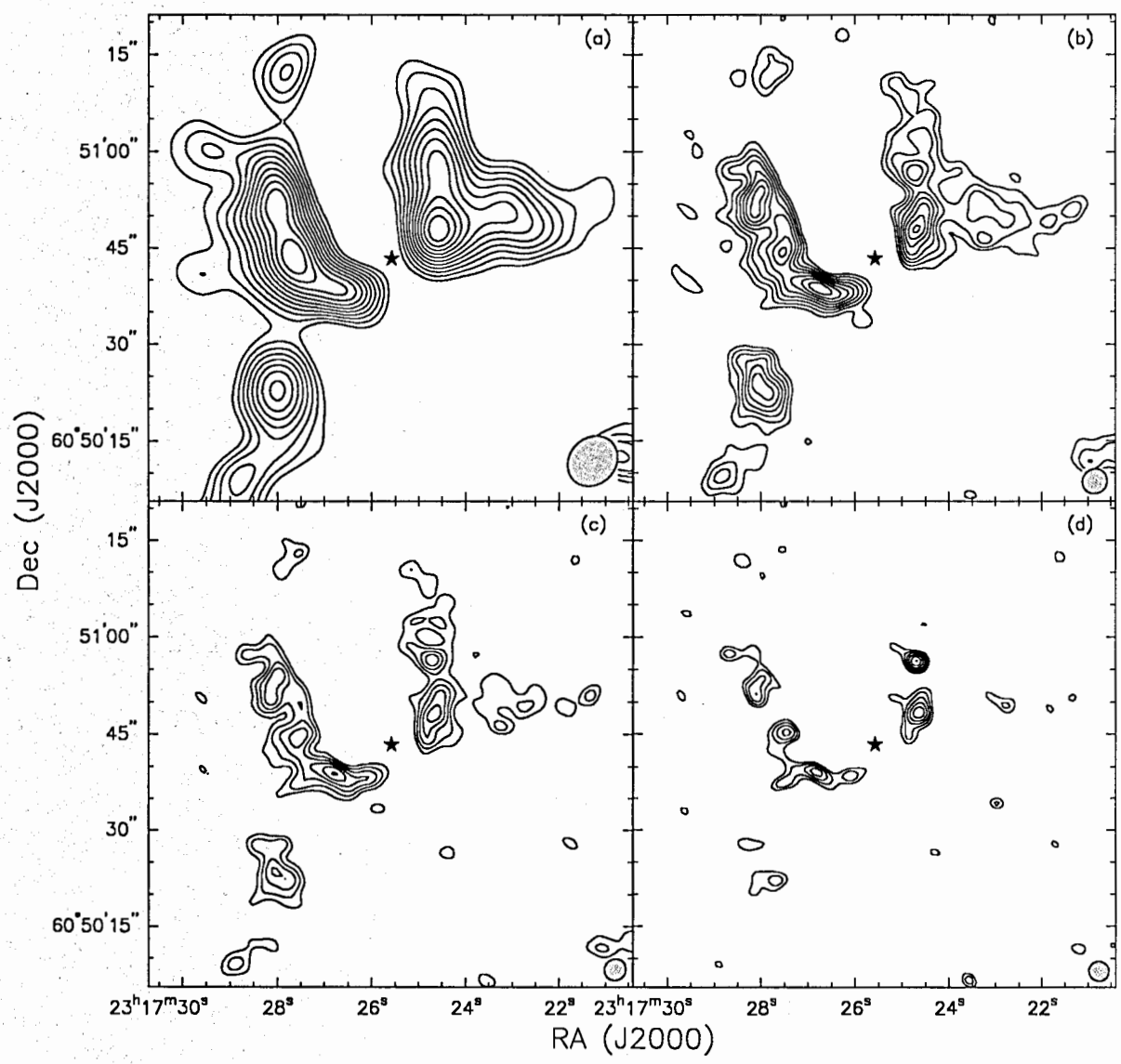

Figure 5.3 The beam sizes are 8.″51 × 7.″25 with a PA of -46°, 4.″04 × 3.″84 with a PA of -62°, 3.″49 × 3.″34 with a PA of -67°, and 3.″24 × 3.″05 with a PA of 72°, from (a) to (d) respectively. Beams are shown at the lower right hand corner of each panel. The contours are linearly spaced from (a) 2 to 13 times of noise, 0.23 Jy/beam km/s, (b) 2 to 10 times of noise, 0.14 Jy/beam km/s, (c) 2 to 8 times of noise, 0.16 Jy/beam km/s, (d) 2 to 5 times of noise, 0.25 Jy/beam km/s. The star symbols indicate the location of MWC 1080.

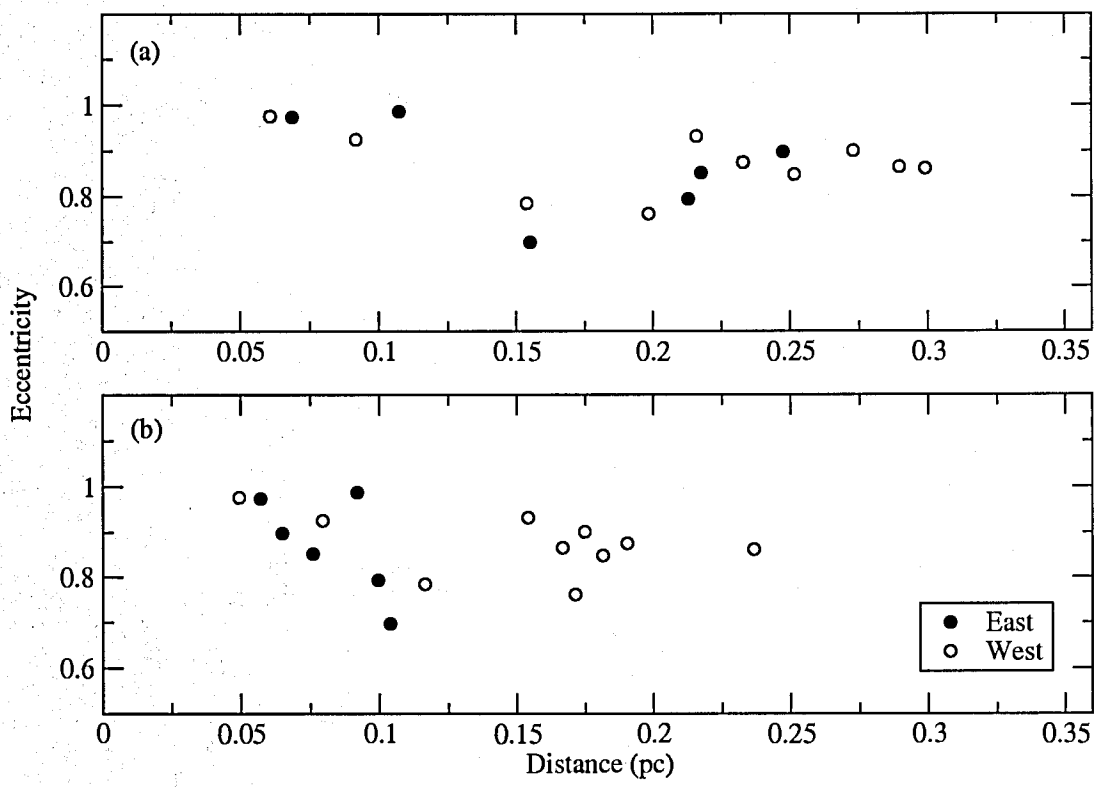

Figure 5.4 The projected eccentricity of clumps vs. the distance to (a) MWC 1080 and (b) outflow axis.

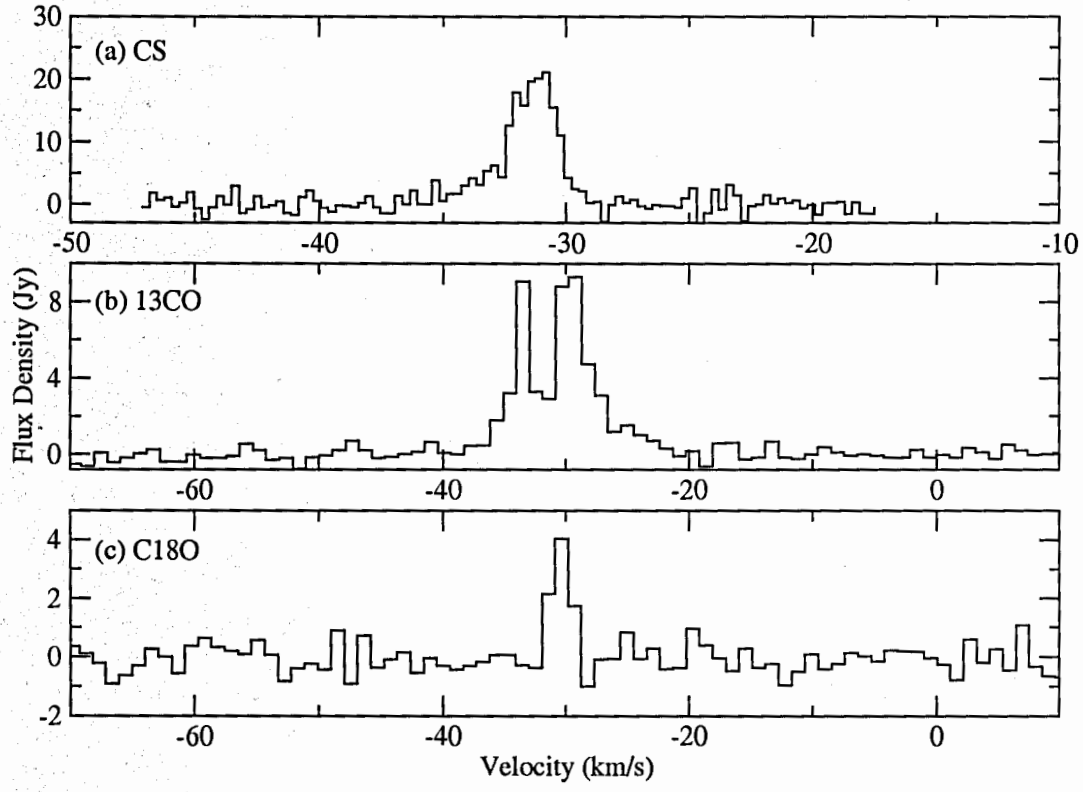

Figure 5.5 Integrated spectra for overall gas traced by CS, ^{13}CO, and $C^{18}O$.

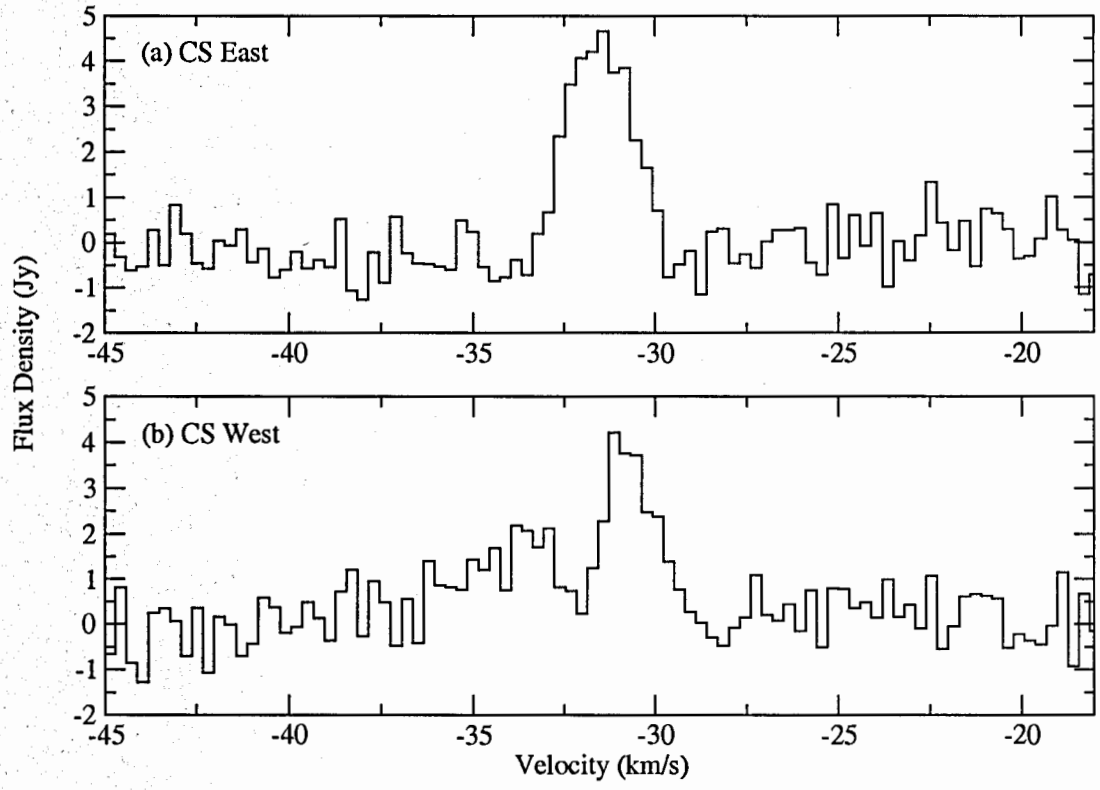

Figure 5.6 Integrated spectra for CS East and West. East shows a broad linewidth; while West shows double-peaked features. This double-peaked feature actually comes from two gas components with different velocities.

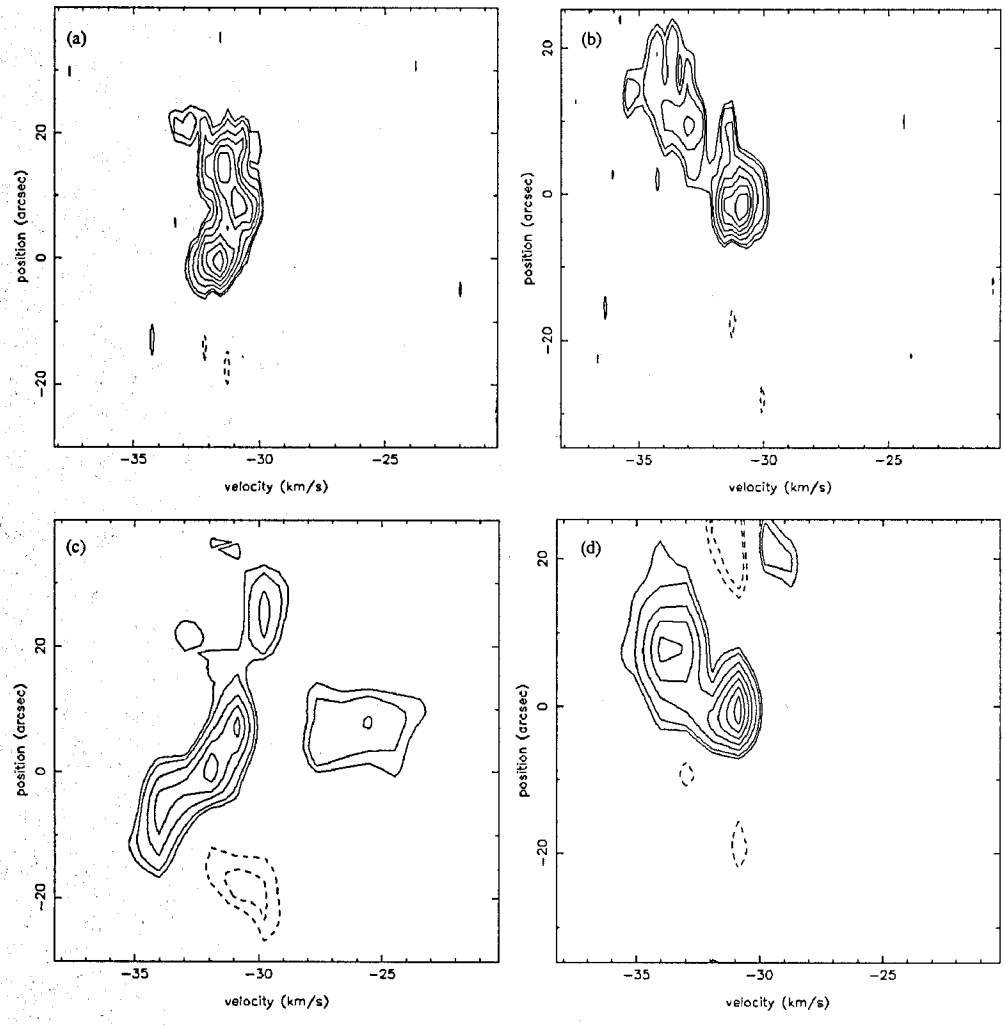

Figure 5.7 Position-velocity (PV) diagrams along the outflow axis for (a) CS East, (b) CS West, (c) ^{13}CO East, and (d) ^{13}CO West. Contours are plotted from 1.5 σ, 2 σ, 3 σ to maximum, with $\sigma = 0.1$ Jy beam^{-1}.

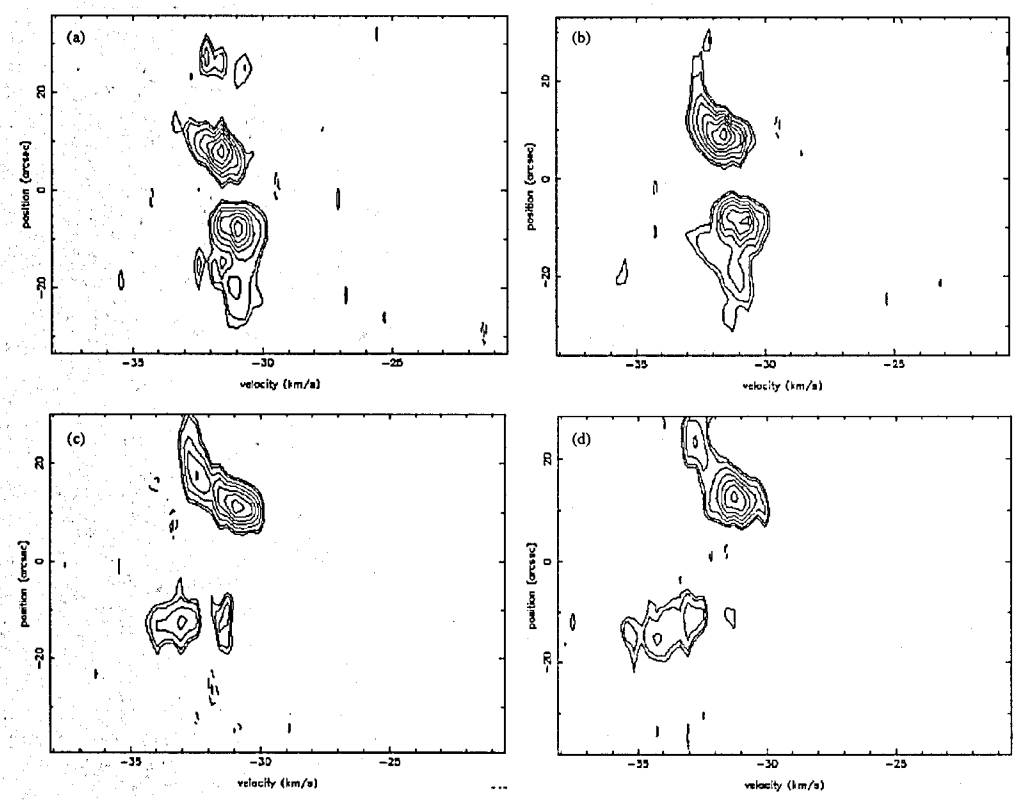

Figure 5.8 PV diagrams along the hourglass axis from closer to MWC 1080 (a) to farther to MWC 1080 (d). Contours are plotted from 1.5 σ, 2 σ, 3 σ to maximum, with $\sigma = 0.1$ Jy beam^{-1}.

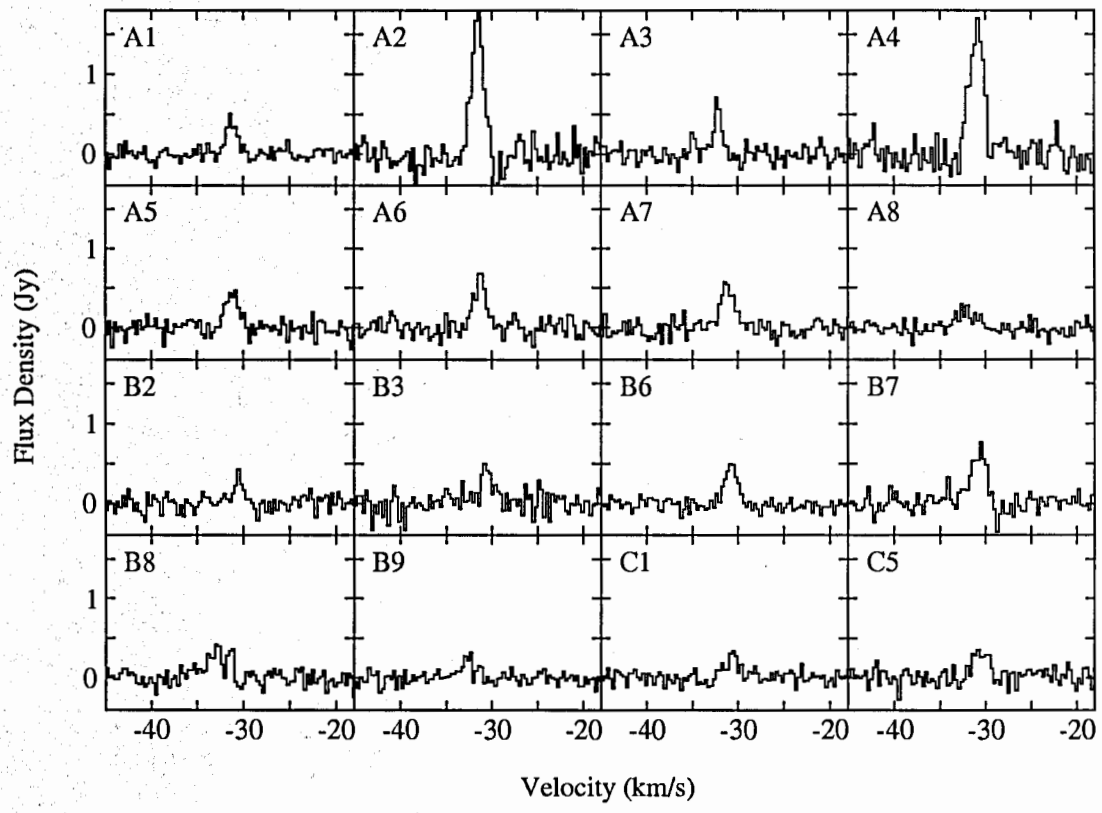

Figure 5.9 Integrated CS spectra for identified CS clumps.

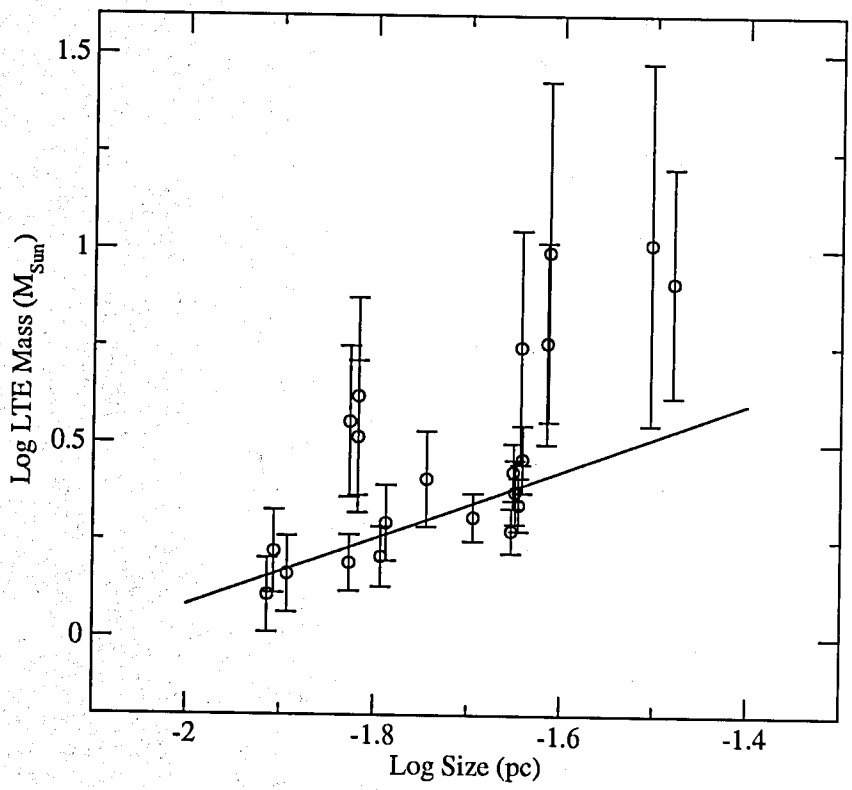

Figure 5.10 Mass vs. size of clumps. The solid line is the fitted relation.

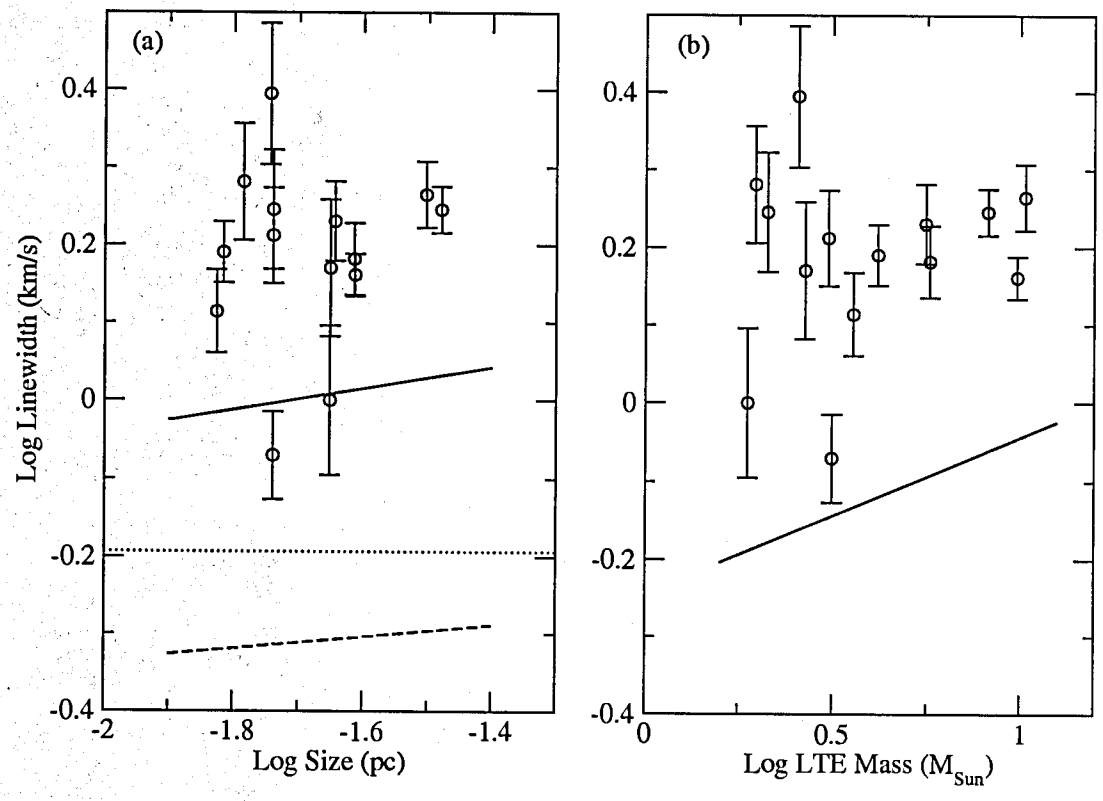

Figure 5.11 The relationship between linewidth vs. (a) size and (b) LTE mass of CS clumps. The solid and dashed lines in (a) indicate the massive cores and low-mass cores (Caselli & Myers 1995), respectively, and the dotted line is the thermal motion at temperature of 20 K. The solid line in (b) indicates the mass-linewidth relation from Larson (1981).

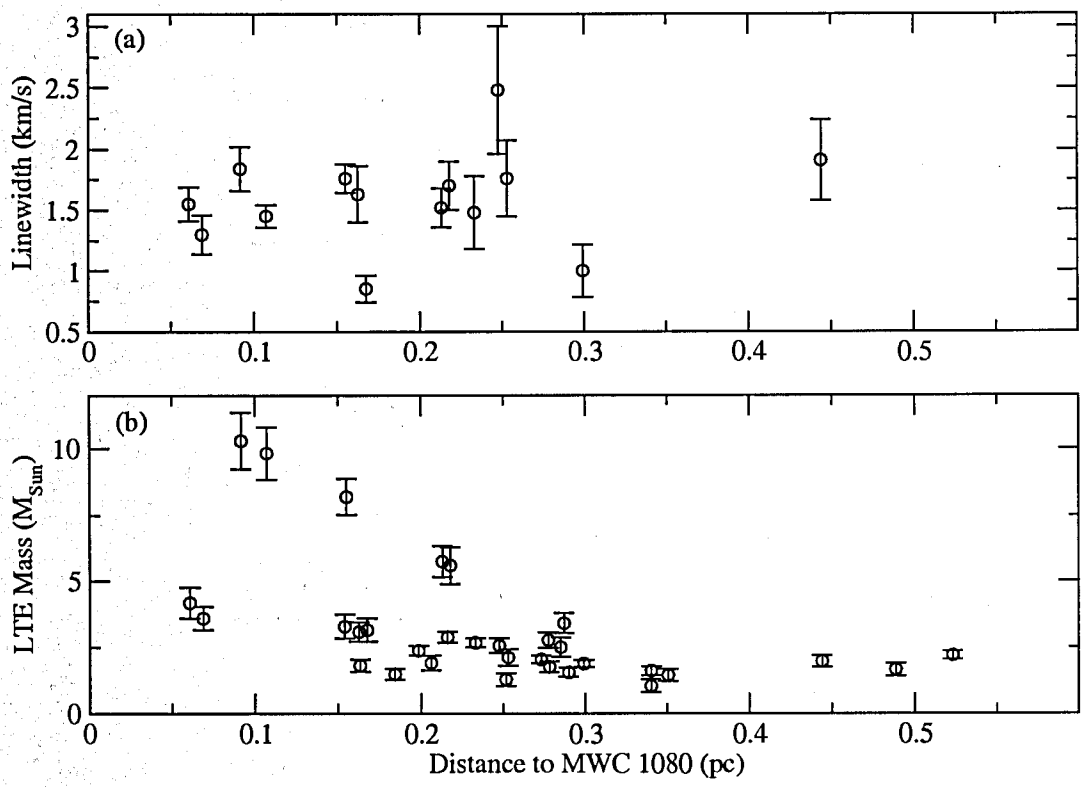

Figure 5.12 (a) The CS linewidth and (b) the derived LTE mass vs. the distance to MWC 1080.

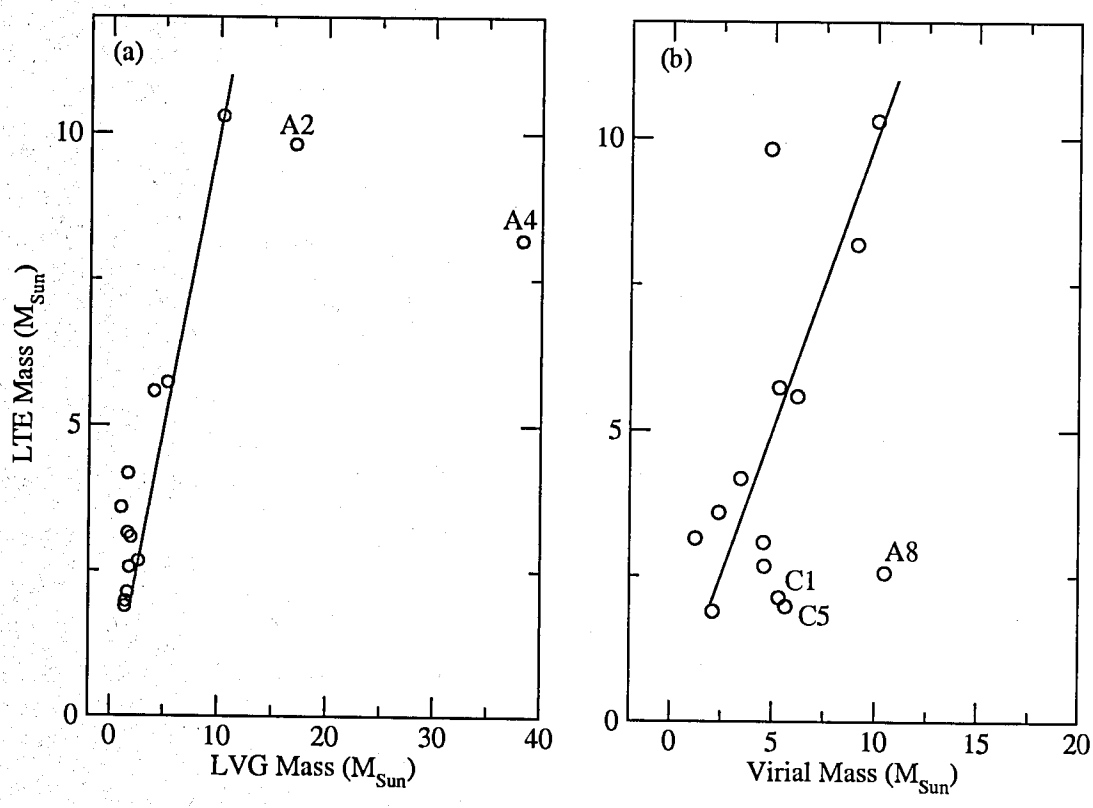

Figure 5.13 The comparison between differently derived masses. The solid lines are when the two masses are equal.

Chapter 6

The Laboratory of the MWC 1080 Cluster– Rule of the Massive Star: II. The Stars

In this chapter, I present the high-resolution CFHT adaptive-optics near-infrared observations toward the MWC 1080 system. The main goal is to identify young stars very close to MWC 1080 and examine their infrared properties.

As mentioned in Ch. 4, stars away from 0.3 pc radius around the massive star are dominated by the intrinsic clustering over effects from the massive star. On the other hand, those forming stars closer than 0.3 pc radius are possibly experiencing significant influence from the massive star. For example, as discussed in Ch. 1, massive stars impact their siblings and result in disk truncation and mass loss modification of the circumstellar material around the siblings. Furthermore, it is still not clear how cluster members are located compared to the massive star, due to serious saturation near these bright HAeBes or even more massive stars in previous studies. However, this is important because it reveals the star forming efficiency, which may have been previously underestimated, and helps understand the initial mass function (IMF) in clusters.

Therefore, with the high-resolution CFHT adaptive-optics data, I will probe stars within 0.3 pc radius around MWC 1080 and examine any ensemble difference of these stars from isolated star formation.

6.1 Near-infrared Observations

I present the Hokupa'a 36 (Graves et al. 1998) adaptive-optics near-infrared JHK′ observations, with 0.035″ pixel size, from the 3.6 m CFHT. The field of view of these observations is $\sim 0.9' \times 0.9'$, which allows us to probe the cluster around the MWC 1080 within ~0.3 pc radius. In addition, I have also carried out wide-field Omega 2000 near-infrared HKs observations for standard star calibrations.

IRAF DAOFIND is used to identify point sources and perform photometry with PSF fitting for both wide-field and adaptive-optics data. At first, in order to calibrate the wide-field H and Ks observations, I select $\sim$ 50 isolated and bright stars throughout the whole field as standard stars and calibrate them with the Two Micron All Sky Survey (2MASS; Skrutskie et al. 2006) point-source catalog. Then, I use the calibrated wide-field data to calibrate the photometry of the adaptive-optics H and K$'$ data with 8 stars as standard ones. The uncertainty of H and K$'$ band is $\sim$ 0.15 magnitude.

For the J band, as I do not have any wide-field observation, I directly use the 2MASS catalog to obtain the transformation relation between the 2MASS photometry and adaptive-optics photometry. Since there are only three stars available to be standard stars, the uncertainty at this band is $\sim$ 0.3 magnitude. I also use the same 2MASS to adaptive-optics transformation method for stars at H band, which gives a 0.2 magnitude difference from wide-field to adaptive-optics field.

6.2 Dust Morphology around MWC 1080

The left and right portion of Figure 6.1 show the rgb color composite of wide-field JHKs and adaptive-optics JHK$'$ images, respectively. The wide-field images show a nebulear morphology centered on MWC 1080, which is mostly elongatedly distributed along the outflow direction (position angle of 45 degrees, Wang et al. 2008) within 0.5 pc and also spherically extended up to 1 pc from MWC 1080. However, unlike the large-scale nebulae seen in the wide-field images, a hourglass morphology is revealled along the direction perpendicular to the outflow axis. Nebulae seen in both images show color gradients, which implies that they are reflected light, which is illustrated by the UV radiation from MWC 1080 on the surface of dust.

Figure 6.2 plots velocity-integrated ^{13}CO contours (Wang et al. 2008) overlaid on the wide-field Ks, and CS contour (Wang et al. 2008) with identified stars from the adaptive-optics images in this chapter. ^{13}CO traces the dense molecular gas in this cluster, and is clearly aligned with the large-scale elongated dust within 0.5 pc region, along the outflow direction. For example, a hole in the dust morphology is seen in the northeastern side from MWC 1080, which matches well with the hole in ^{13}CO map in this area. Wang et al. (2008) suggests that the observed dense molecular gas presents the swept-up gas by outflows, which is dominated by MWC 1080, instead of the initial

natal gas. Therefore, the bright elongated dust condensation within 0.5 pc also most likely traces the swept-up material, as the enhancement of its density results from the accumulation of outflow activities. On the other hand, the diffuse dust which extends spherically to 1 pc still preserves the initial conditions of cluster-forming environment.

In addition, the hourglass morphology of small-scale dust seen in the adaptive-optics image also traces well with ^{13}CO in the region close to the MWC 1080. A biconical outflow cavity is well revealled by ^{13}CO, which corresponds to the absence of dust along the outflow direction in the adaptive-optics image. This is why an hourglass shape is observed. Not only dust, there are numbers of stars revealled, especially in the outflow cavity from the removal of cloud material by the outflow.

Another interesting feature in the dust morphology is that the large-scale dust is brighter, in the northeastern side than that in the southwestern side along the outflow direction (Wang et al. 2008). There is a higher density of dense molecular gas distributed to the northeast (lower desnity to the soutwest). This implies that gas and dust are denser in the northeast. This is likely an inclination effect; the northeast is toward us and the southwest is away from us.

6.3 Clustering of Star Formation in Young Clusters

It has been shown that there are sub-structures in massive clusters (e.g., Allen et al. 2006). Wang & Looney (2007) also suggests that these sub-clusters in massive clusters might be comparable to isolated small groups or clusters, which typically surround one to a few intermediate-mass to massive stars, such as the MWC 1080 system. This means that understanding the overall star formation in massive clusters and cluster formation can be based on investigating the formation and clustering of cluster members in small clusters and comparing them with massive clusters. In this section, I take a close look at the stellar distribution and clustering in the MWC 1080 system and other nearby small clusters.

6.3.1 Stellar Population around MWC 1080

There are 44 stars identified within 0.25 pc of MWC 1080 from the adaptive optics images. There are stars also associated with this cluster outside 0.25 pc from MWC 1080, as the size of whole

reflected nebula extends up to 1 pc range. However, in this chapter, I focus on those stars within 0.25 pc, because they are located deeply within the cluster core and experience the most influence from MWC 1080. Our results show a surface number density within the inner 0.25 pc range in this cluster to be $\sim$ 230 stars per pc^2.

Figure 6.3 plots the size vs. the surface number density of stars of nearby embedded clusters within 2.5 kpc from Lada & Lada (2003). In order to compare my result of the MWC 1080 system to these clusters, Figure 6.4 also plots its location as a filled triangle, using the 0.25 pc as its size, although this is not the actual cluster size. Adams et al. (2006) fits a relation between the size (R) and the number of stars (N) of these clusters, $R = (1-2)$ pc $(N/300)^{1/2}$, which implies that there exists a roughly constant surface number density, $\sim$ 25 - 100 stars per pc^2. Figure 6.4 and this relation show that the MWC 1080 cluster seems to have a much higher surface number density in the inner cluster region ($<$ 0.25 pc). However, this comparison does not necessarily mean that the MWC 1080 is especially crowded compared to any other cluster.

Table 6.1 lists parameters of some embedded clusters, including the size, number of stars, surface number density, and the detection limit at K band. The locations of these clusters are also labelled in the Figure 6.3. This table shows that one of reasons that my results of the MWC 1080 system show a higher surface number density than other clusters is simply because of its better sensitivity than other observations (e.g., IC 348). Another reason is that the high spatial resolution of my adaptive-optics observations allow us to detect stars in the cluster core, which cannot be achieved by previous observations, especially for distant sources (e.g., NGC 2282) or bright sources (e.g., MWC 297). The only cluster which we can fairly compare with the MWC 1080 system is the Trapezium cluster in Orion, because of their comparable distance-scaled detection limits and spatial resolutions (Muench et al. 2002; Lada & Lada 2003). Table 6.1 shows that the surface number density in the Trapezium cluster is much higher than the MWC 1080 system. This is not surprising, as the Trapezium cluster hosts more massive stars than the MWC 1080. Nevertheless, my result shows a higher surface number density in the cluster core than previous observations of nearby embedded clusters. This suggests that there might be a large number of stars hidden within the cores of these clusters in previous studies due to their dimness or being shielded by the central massive star in the cluster.

6.3.2 Average Surface Density of Companions

In order to characterize the population of cluster members around MWC 1080, I further investigate the clustering of both stars and dense cores in this system. The average surface density of companions $\Sigma(\theta)$, or equivalently the two-point correlation function, has been used to study the clustering of young stellar populations in several nearby star forming regions (Gomez et al. 1993; Larson 1995; Simon 1997; Nakajima et al. 1998). $\Sigma(\theta)$ is defined as the average number of companions with the angular separation θ per surface area per star. $\Sigma(\theta)$ is calculated by counting the number of stars located within the annulus at certain radial distance θ from each star and normalizing it for all stars devided by the area of this annulus (also see the equations (1) to (3) in Nakajima et al. 1998, for the formula of Σ and its error estimation). Therefore, in a cluster with N stars, the average surface density of companions within the j-th annulas $[\theta_{j-\frac{1}{2}}, \theta_{j+\frac{1}{2}}]$ from each star is,

$$\Sigma_j = \Sigma(\theta_j) \equiv \frac{1}{N} \sum_{i=1}^{N} \frac{n_{i,j}}{\pi(\theta^2_{j+\frac{1}{2}} - \theta^2_{j-\frac{1}{2}})}, \tag{6.1}$$

where $n_{i,j}$ is number of stars within the annulas $[\theta_{j-\frac{1}{2}}, \theta_{j+\frac{1}{2}}]$ from the i-th star. Throughout this section, I calculate the Σ with varied annulas sizes in order to keep a constant uncertainty between each bin.

Gomez et al. (1993) shows that the two-point correlation of young stars in Taurus follows a power-law relation suggesting a clustering than random distribution, which might present a hierarchical structure of the star-forming cloud. Larson (1995) further shows different power-law relations between the binary and cluster scale. In addition, there is a consistent behavior for binary formation between different star-forming regions (Simon 1997), and the break between two scales probably depends on the dispersal history of the star-forming systems (Nakajima et al. 1998). Nevertheless, the average surface density of companions has been an efficient method to characterize the clustering of binary and cluster formation.

Figure 6.4 plots $\Sigma(\theta)$ vs θ for both stars and dense molecular cores (Wang et al. 2008) around MWC 1080. Dense cores indicate the possible site of prestellar or protostellar star-forming cores. Wang et al. (2008) has identified these cores by using BIMA CS line observations. Figure 6.4 shows that both stars and molecular cores trace very similar power laws, suggesting that both types of

sources probably origin from the same star-forming episode. This supports that these stars are just revealled earlier than equivalent isolated stars by energetic outflows from MWC 1080, which has been suggested in Wang et al. (2008).

Moreover, the power law in Figure 6.4 is also significantly presenting a nearly initial clustering in a centrally condensed cluster like the MWC 1080 system, which might be also comparable to those sub-clusters seen in massive clusters (Wang & Looney 2007). This can be a starting point to study the initial clustering of star formation in clusters, and should be further compared to the clustering of dense cores and young stars in different cluster environments. In particular, the power law features of clustering of dense cores in protoclusters will be useful to understand the clustering of star formation at the earliest stages.

Another interesting feature of the power law in the Figure 6.4, especially from 4(a), is the lack of a slope break and binary regime as seen in other young clusters, (Gomez et al. 1993; Larson 1995; Simon 1997; Nakajima et al. 1998). Simon (1997) shows that there is a universal power index $\sim$ -2.0 in the binary regime, power laws from -0.2 to -0.7 in the cluster regime, and breaks from $\sim$ 0.002 to 0.06 pc, for Taurus, Ophiuchus, and Trapezium. Our result of the MWC 1080 system is similar to the cluster regime for star separations from $\sim$0.007 pc to 0.5 pc ($\sim$ 1500 - 10000 AU), without a power law break. This suggests that either the binary regime exists in a smaller scale or the formation mechanism resulting in a different law in the binary regime from the cluster regime does not initiate at the early stage of star formation in this system. Again, studies in more systems are needed to systematically probe this power law break. In particular, the clustering in protoclusters will be very useful to examine these suggestions.

In order to compare my results with other small clusters, Figure 6.5 plots $\Sigma(\theta)$ vs θ for young stars in several small clusters Wang & Looney (2007). These clusters are all embedded or partially embedded small clusters around Herbig Ae/Be stars. Wang & Looney (2007) use Spitzer observations to identify young stars around these systems and show that there are groups of young stars centered on the Herbig Ae/Be stars and also young stars populated throughout the whole fields outside the cluster systems. Figure 6.5 is only plotting the clustering of those groups of young stars centered on the Herbig Ae/Be stars, which present similar systems with the MWC 1080 cluster. This plot shows power indices from 0.1 to 0.7 for these systems, which are consistent to the MWC

1080 system and the cluster regime in other clusters (e.g., Simon 1997, for Taurus, Ophiuchus, and Trapezium).

6.4 Infrared Properties of Identified Stars

From the adaptive-optics images, I identify 44 stars around MWC 1080 within $\sim$ 0.25 pc radius. Figures 6.6 and 6.7 are the color-magnitude and color-color diagram of identified stars. I also indicate the slopes of main sequence and pre-main sequence stars (Bessell & Brett 1988; D'Antona & Mazzitelli 1994), the classical T-Tauri star (CTT) loci (Meyer et al. 1997), and the interstellar extinction arrows Rieke & Lebofsky (1985).

From the Figure 6.6, it shows that the mass of these stars are between 0.1 and 2.5 $M_{\odot}$. Figure 6.7 further shows that $\sim$ 35 % of stars are redder than extincted main sequence stars, which means that they have large infrared excesses similar to CTTs or younger sources; while $\sim$ 65 % have near-infrared emission similar to stars with little circumstellar material, such as weak-line T-Tauri stars (WTTs) or pre-main sequence stars. However, previous studies of small clusters around Herbig Ae/Be stars (Hillenbrand et al. 1995a) have suggested that most cluster members in these young clusters have large infrared excesses.

In order to understand why we have different results from other studies, I compare stars with or without large infrared excesses. I separate the identified stars to (1) those inside the outflow cavity and (2) those outside the outflow cavity, which are labelled in the Figure 6.7. The former case presents the stars that have been influenced by the strong outflow from MWC 1080 and are revealed by the outflow. On the other hand, stars of the latter case form within the dense core of this system but are not influenced by the outflow. From Figure 6.7, only 25% of stars in the cavity have large infrared excesses; while 100% of stars outside the cavity do. Figure 6.7 suggests that stars outside the cavity have more infrared excesses, which are probably younger, than stars inside the cavity. This means that stars inside the cavity are not just less extincted but also have less circumstellar material, compared to those outside the cavity. This suggests that the MWC 1080 outflow does not just clean out the interstellar material to form the cavity and reveal its cluster members, but also help clean the circumstellar material that influences the formation processes of its cluster members. Moreover, stars outside the cavity are actually consistent with stars with

large infrared excesses from previous studies, which were not able to probe stars very close to the central Herbig Ae/Be stars. This means that small percentage of young stars in this study simply indicates the effects from MWC 1080.

In addition to have less circumstellar material than those outside the cavity, stars within the cavity also seem older than they should normally be if they are isolated, assuming all stars in this system form coevally (suggested from Sec. 4) and have an age like MWC 1080. In order to examine the circumstellar material and ages of stars in the cavity, I fit them with young stellar models (Robitaille et al. 2006, 2007). Model fitting shows that these stars have masses of 0.1 - 5 $M_{\odot}$, disk masses of 10^{-2} - 10^{-9} $M_{\odot}$, and disk accretion rates of 10^{-8} - 10^{-14} $M_{\odot}$/yr. It also shows that most stars in the cavity seem to have ages of $\sim$ 1 - 10 Myrs. Assuming these stars form coevally with MWC 1080, they should have age of 0.1 - 1 Myr, but look as having age of 1 - 10 Myrs. Therefore, assuming the age of all stars in this system is 0.1 - 1 Myr, stars outside the cavity have the formation time scale similar to the stars formed in isolation; while outflows from MWC 1080 speed up the formation of stars in the cavity to an order of magnitude.

I also try to see if there is any trend between those fitted parameters and the distance from MWC 1080, which is to investigate any effect from MWC 1080. However, no trend is found.

6.5 Discussion and Conclusion

MWC 1080 system is a young cluster around a Herbig Be star, which is still young and has large infrared excess (Hillenbrand et al. 1992). Wang et al. (2008) maps the dense gas around this system using high-resolution millimeter interferometry and reveals a small outflow cavity. In this chapter, our adaptive-optics near-infrared observations show that there are 44 stars identified within 0.25 pc from MWC 1080– 85% are located within the cavity. The MWC 1080 cluster presents a young system with age of $<$ 1 Myr, where the formation of stars are still constantly being affected by the forming nearby massive star, especially those stars in the cavity. Here I summarize our results.

6.5.1 Clustering of Stars

I calculate the average surface density of companions for identified stars and CS clumps (Wang et al. 2008). I find that both sources trace the same power-law relation with a power index of $\sim$ -0.8,

which suggests that both sources may form from a single star-forming episode. This non-zero value indicates a clustering rather than random distribution. Our result consists with other star-forming regions which have power-law relations from -0.1 to -1 (Gomez et al. 1993; Larson 1995; Simon 1997; Nakajima et al. 1998). This power law is interpreted as presenting a hierarchical structure of the natal star-forming cloud.

Most of previous studies calculate this value for stars in large molecular clouds, which contain sub-clusters and possibly different episodes of star formation. However, our system is a small central-condensed cluster-forming core, which is still forming stars and has a single star-forming episode. This suggests that the hierarchical structure exists in a small scale at its early star-forming stage, and possibly propagates from this small scale, such as sub-clusters, to the whole large-scale cloud.

In addition, unlike the power index break seen in other star-forming regions (Gomez et al. 1993; Larson 1995; Simon 1997; Nakajima et al. 1998), there is no break between 0.007 to 0.5 pc and no binary regime in the MWC 1080 system. This probably means that either the binary regime exists in a smaller scale or the formation mechanism resulting in different laws between the binary and cluster regime does not initiate at the early stage of star formation in this system. More studies, such as clustering in other clusters or protoclusters and clustering of star-forming molecular cores, are needed, in order to clarify these suggestions.

6.5.2 Effects from the MWC 1080 Outflow

In order to understand the effects from the MWC 1080 outflow, I examine the infrared properties by distinguishing stars inside and outside the outflow cavity– the former has experienced strong outflows from MWC 1080 and the latter has not.

From the colors of stars, I find that stars in the outflow cavity have less infrared excesses, thus less circumstellar material, than those outside the cavity. Indeed, 75% of stars in the cavity have near-infrared emission with little circumstellar contribution, such as WTTs, pre-main sequence stars or main sequence stars; while 100% of stars outside the cavity are similar to CTTs or younger source. In addition, using young stellar models (Robitaille et al. 2006, 2007), stars in the cavity have average ages of 1 - 10 Myrs, an order of magnitude larger than the age of MWC 1080. This

also means that they seem older than they should be, if assuming all stars form coevally with MWC 1080.

Therefore, stars in the cavity are not just less extincted than those outside, but they also seem older than they usually are if forming in isolation. This suggests that the MWC 1080 outflow cleans out the natal cloud to form a outflow cavity that reveals cluster members, and also also removes the circumstellar material from the stars, cutting off the mass reservior, ablating the disk, or disrupting the disk, making the sources appear older.

6.5.3 Summary

The main thrust of this chapter is to understand the role of massive stars in their surrounding low-mass stars by studying a young small cluster around MWC 1080. This is a system having tens of stars forming very close to a massive star while the massive star is still forming and strongly dispersing its natal cloud. Wang et al. (2008) has suggested that low-mass stars tend to form in denser and more turbulent cores around the massive star, and this chapter further shows that the formation of low-mass cluster members is speeded up by strong gas dispersal activities from the massive star.

Table 6.1. Parameters of Nearby Embedded Clusters

Cluster	Distance (pc)	R[a] (pc)	N[b]	S[c] (stars pc^{-2})	K (limit)	K_{2200pc}[d] (limit)	Refs.
MWC 1080	2200	0.25	45	230	14.1	14.1	1
IC 348	320	1.00	300	95	15.0	10.8	2
Trapezium	450	0.24	780	4300	17.5	14.1	2
MWC 297	450	0.50	37	47	16.7	13.3	2
NGC 2282	1700	1.60	111	14	15.0	14.4	2

[a]Either the size or some radial range from the cluster center.

[b]Number of stars within R.

[c]Mean surface number density, which is equal to $N/(\pi R^2)$.

[d]The magnitude limit at K band when the source is at 2.2 kpc.

References. — (1) this study (2) Lada & Lada (2003)

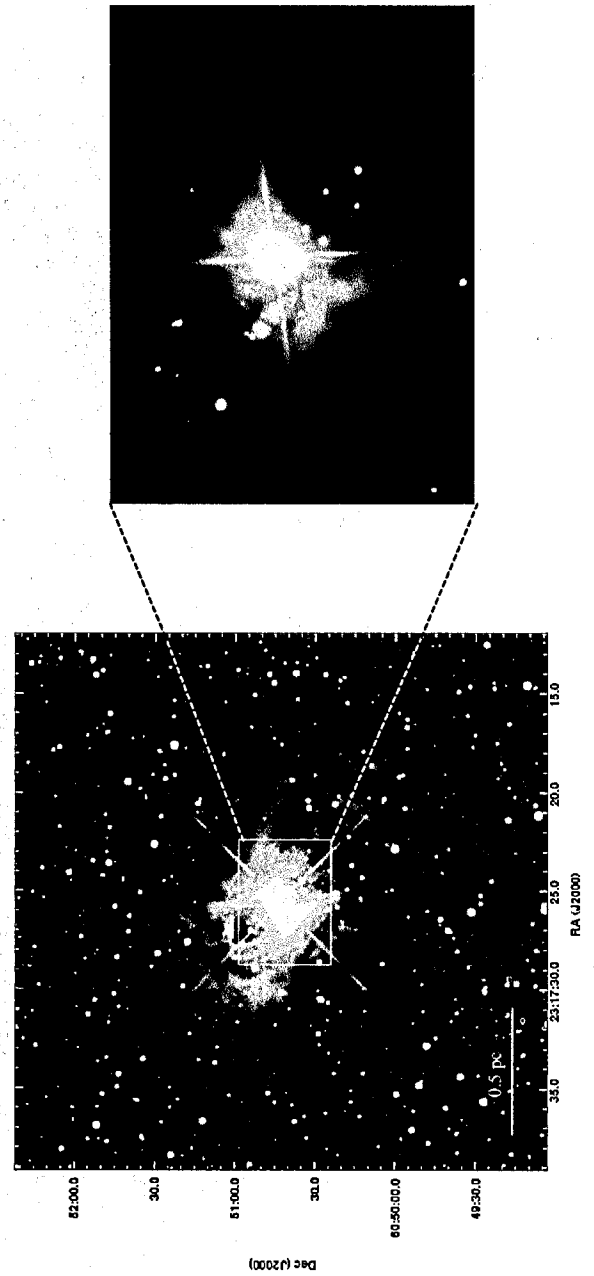

Figure 6.1 Left: Color composite image of the wide-field observations at Brg (blue), H (green), and Ks (red) bands. Right: Color composite image of the adaptive-optics JHK′ observations.

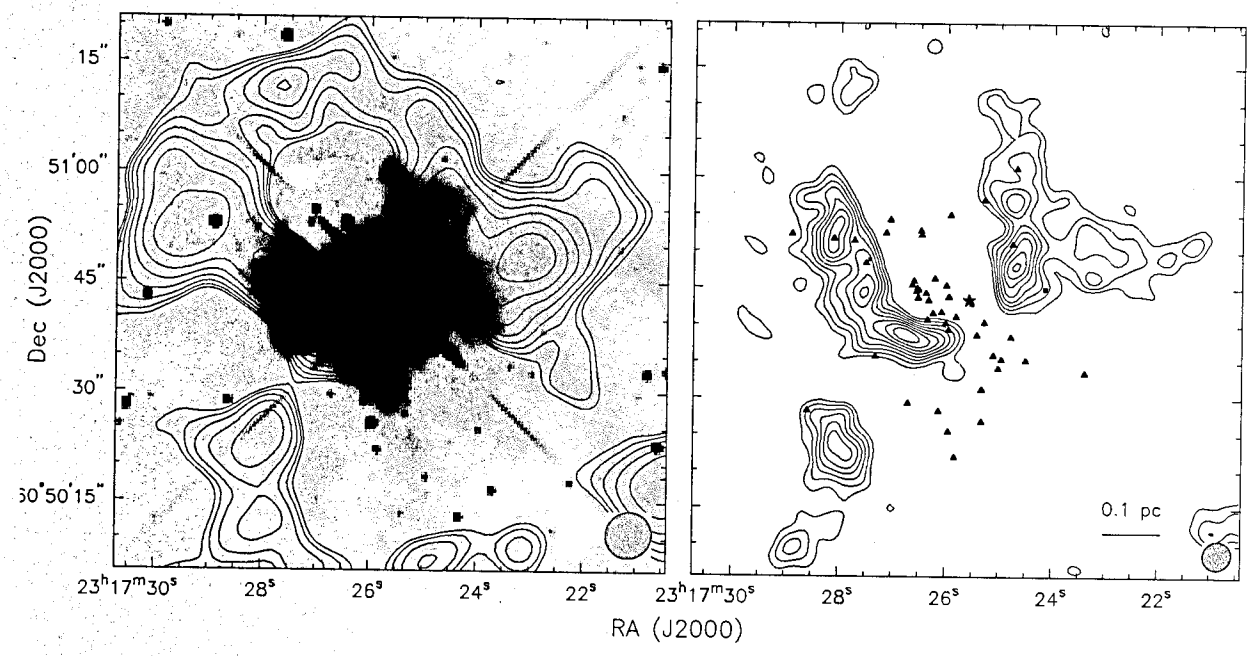

Figure 6.2 Left: ^{13}CO (1-0) contours overlaid on the wide-field Ks image. Right: CS (2-1) contours. Stars, which are identified from the adaptive-optics images, are labelled.

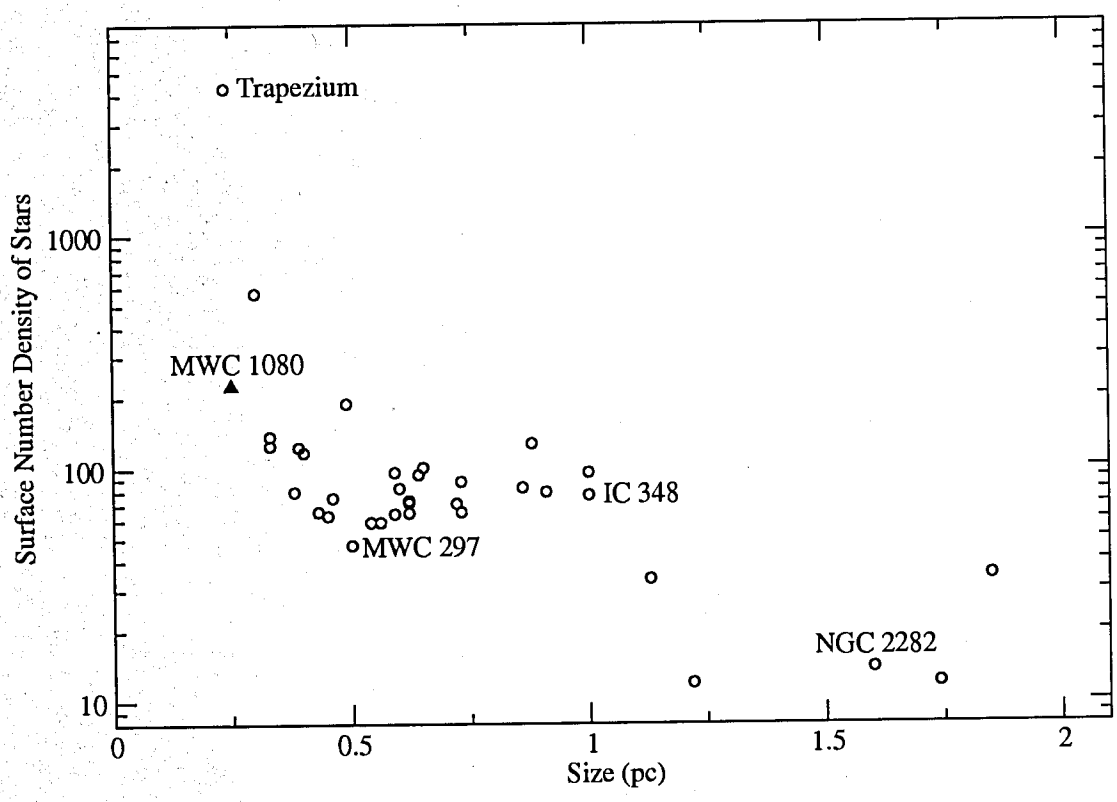

Figure 6.3 A comparsion for the surface number density of stars vs. cluster size between several clusters.

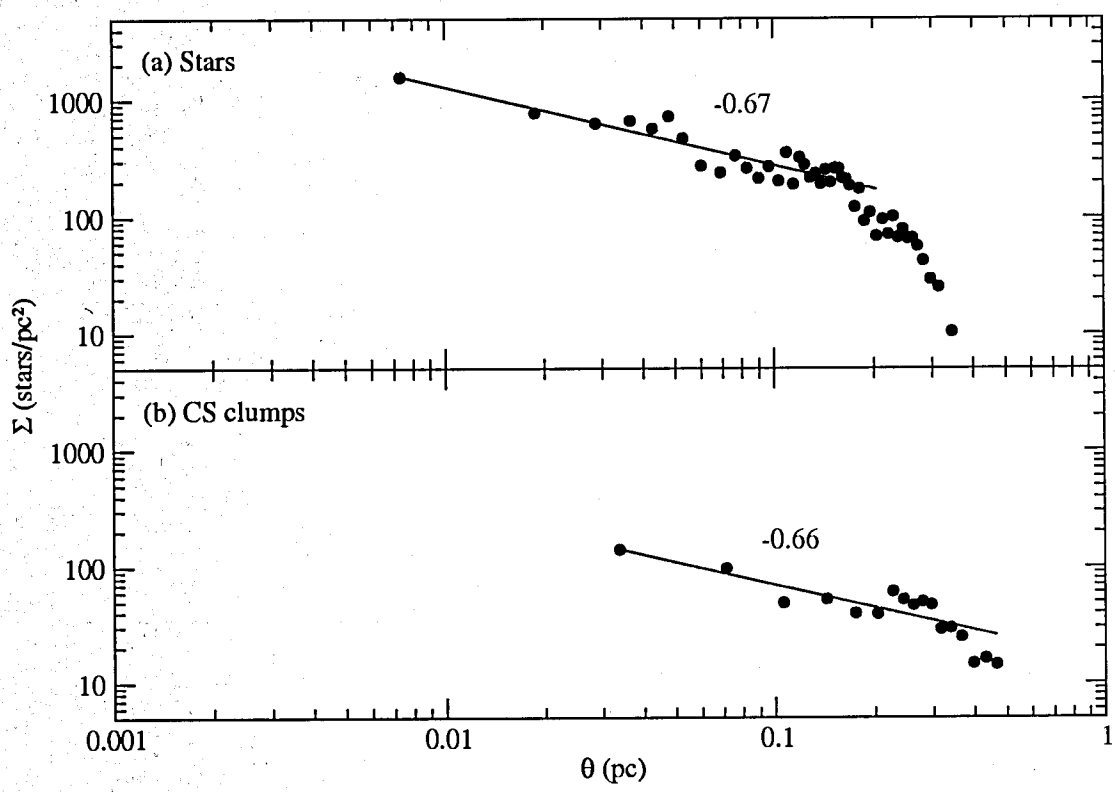

Figure 6.4 Average surface density of companions for identified stars and CS clumps (from Ch. 5). This figure shows that both stars and dense gas clumps are distributed following the same power law. This suggests that they probably come from the same star-forming episode, but stars are just revealled earlier due to the strong outflow from MWC 1080.

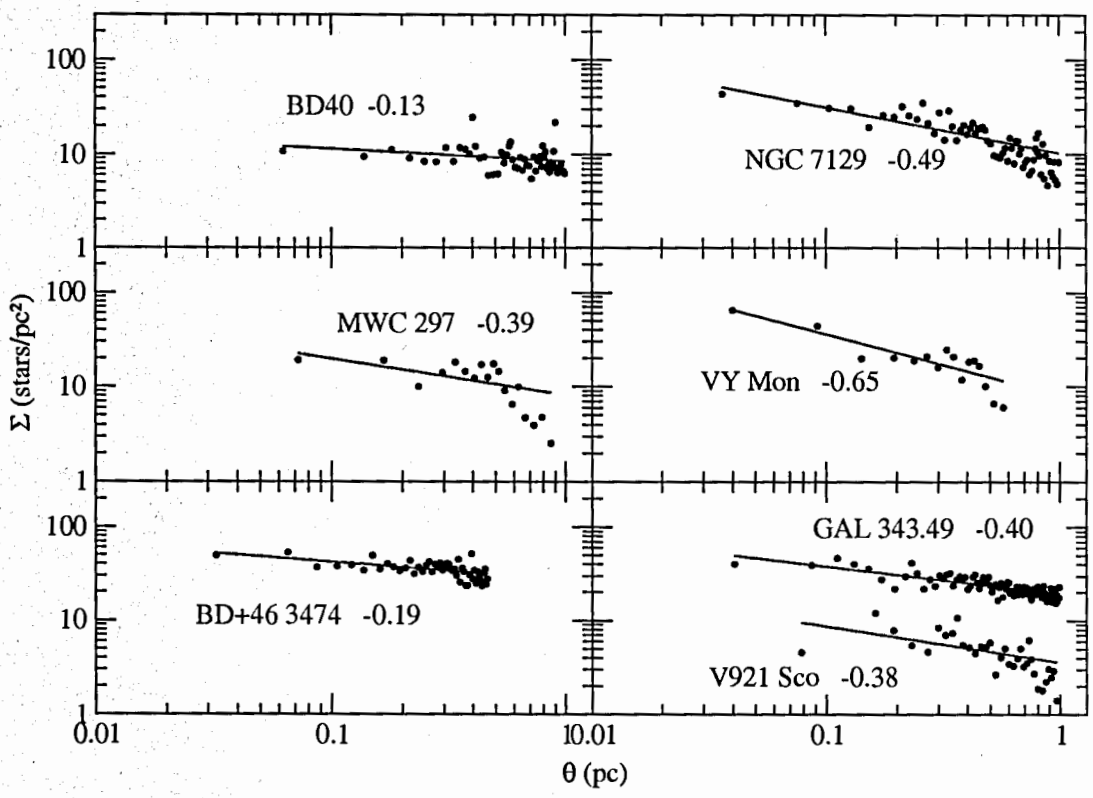

Figure 6.5 Average surface density of companions for stars in six clusters (from Ch. 4). This shows at large scale, stars are also populated with a similar power law.

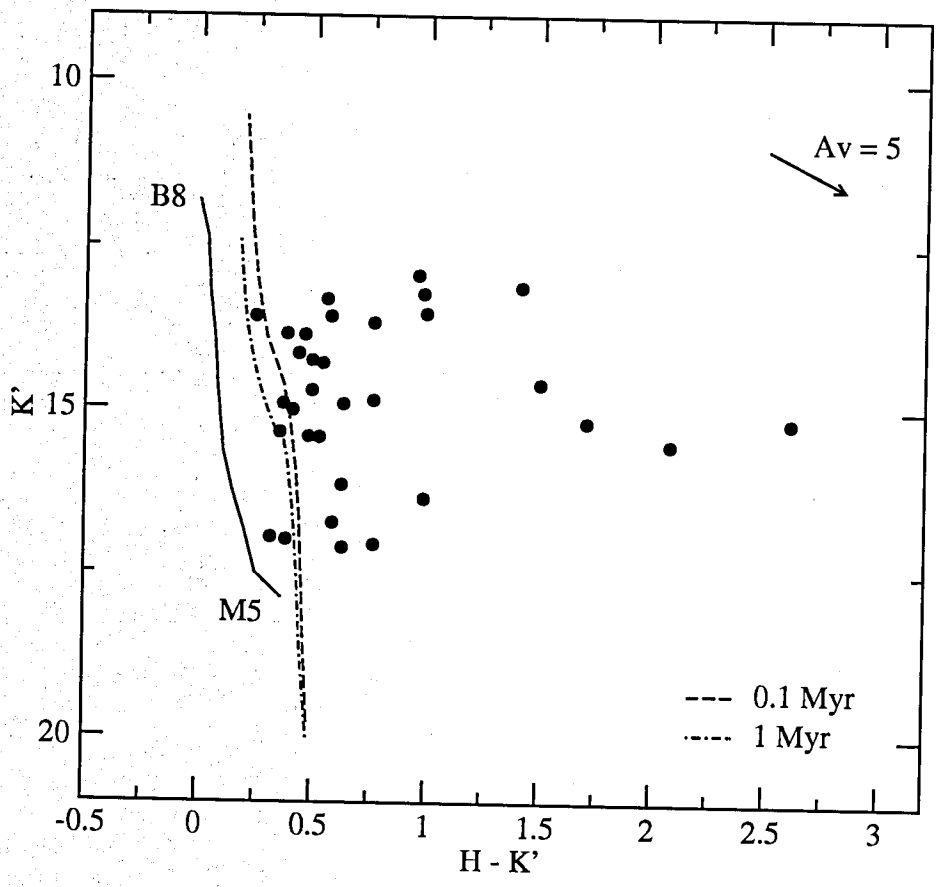

Figure 6.6 Color-magnitude diagram for identified stars. An extinction arrow of $A_V = 5$ is shown. The solid line traces the instrinsic magnitudes and colors for main-sequence stars with spectral types from M5 to B8. The dashed and dashed-dotted lines trace the pre-main sequence stars with masses from 0.1 to 2.5 $M_\odot$ at 0.1 Myr and 1 Myr, respectively.

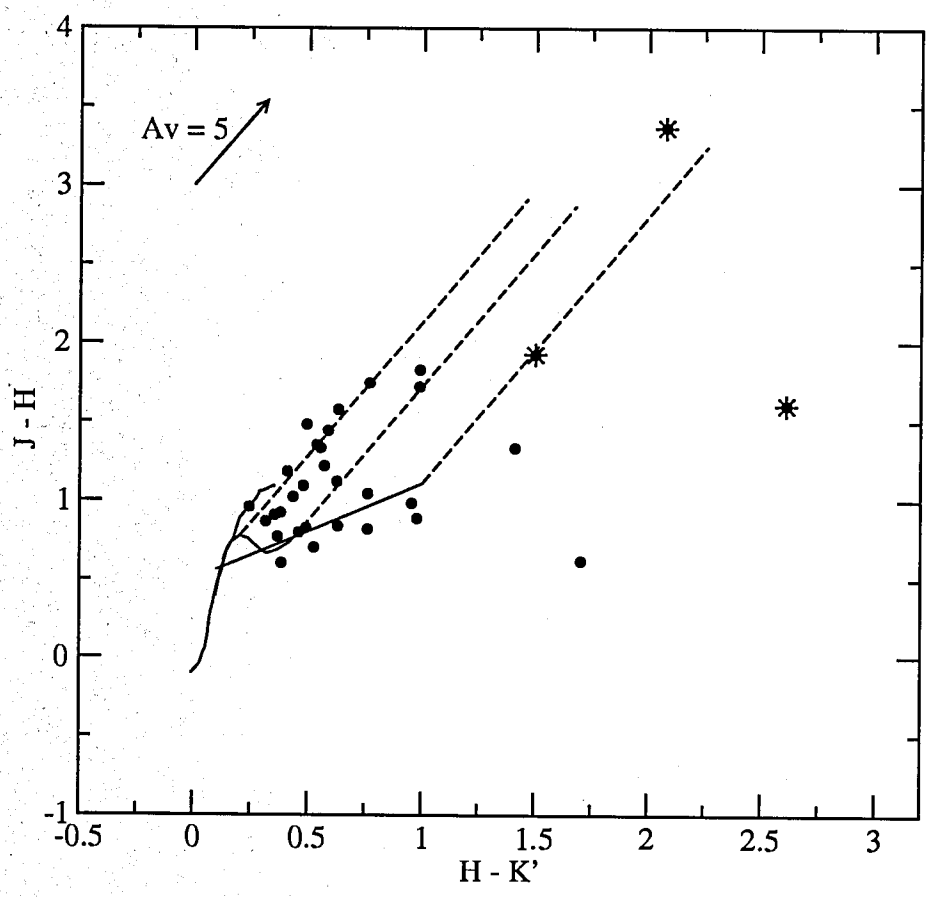

Figure 6.7 JHK′ Color-color diagram of identified stars. The star labels are those stars outside the cavity.

Chapter 7

Dense Molecular Gas around Intermediate Mass Clusters

In this chapter, I present the BIMA interferometric observations of dense gas toward five intermediate-mass young clusters around the BD40, NGC 7129, BD+46° 3471, HD 200775, and Z CMa systems. All of these clusters have known ^{13}CO and CS single-dish detections (Fuente et al. 1998a; Ridge et al. 2003; Hillenbrand et al. 1995a).

Previous single-dish observations of the molecular gas and dust continuum toward many young stellar clusters have actually revealed some interesting morphologies. For example, Fuente et al. (1998a, 2002) studies the gas dispersal around HAeBes, many of which are actually clusters, and proposed a classification based on their surrounding dense gas morphologies. Ridge et al. (2003) mapped the dense gas around a number of young clusters within 1 kpc and also suggested a similar classification of cloud evolution in clusters. As there seems to be an universal classification of the cloud removal process for both clusters and single stars, it indicates that the natal cloud dispersal is dominated by the central most massive star in the system. This means that the molecular gas that low-mass cluster members need is disrupted by their massive sibling rather than themselves. The effects from the massive star on its low-mass cluster siblings have also been seen more directly in the MWC 1080 system (Ch. 5 and 6) using high-resolution observations.

Therefore, based on the results in the MWC 1080 system (Ch. 5. and 6), I study the molecular gas in five more clusters in this chapter, in order to compare the molecular environments at different evolutionary stages, as I sample HAeBes with different ages. CS (2-1) is used as the dense gas tracer here, as it is sufficient to probe the clumpiness of dense molecular gas– one of the main goals in this chapter. Indeed, it is important to identify clumps capable of forming single low-mass stars, so that the physical conditions where each low-mass star is forming in the cluster can be individually revealed.

7.1 BIMA Observations

The CS $J = 2 \rightarrow 1$ observations toward the BD40, BD + 46° 3471, NGC 7129, Z CMa, and HD 200775 were observed in three configurations (B, C, and D) of BIMA array (Welch et al. 1996) in 2003 and 2004, except the C array observation toward the BD40 system, observed in 1996, was obtained from the BIMA archival. The correlator was configured with the line window of a velocity range of 76 km s^{-1} with 0.3 km s^{-1} per channel, and two 600 MHz bands for continuum.

The data were reduced with the MIRIAD package (Sault et al. 1995) and mapped using two or three array configurations with various u, v weighting schemes to stress structures on different spatial scales.

7.2 The Morphology of Dense Gas around HAeBe Clusters

Figure 7.1 - 7.7 show the dense molecular distributions of sampled clusters, which I discuss individually as follows.

7.2.1 BD40

As mentioned in Ch. 2, the BD40 cluster includes three HAeBe stars, BD + 40° 4124 , V1686 Cyg, and the southern star of the V1318 Cyg binary, surrounding by a number of low-mass stars.

Figure 7.1 plots the velocity-integrated maps of the CS (2-1) emission with different beams giving different resolution, overlaid on an adaptive-optics near-infrared H-band image (Davies et al. 2001) illustrating the core stellar distribution. This figure shows that the CS emission, which is tracing the dense molecular gas, does not center on the brightest two HAeBes, BD + 40° 4124 and V1686 Cyg. Instead, it is along a north-south ridge with an extent of ~0.4 pc and actually peaks very close to the southern star of the binary pair, V1318 Cyg, suggesting that this region is forming the youngest members in this system.

Figure 7.2 shows that the dense gas traced by the CS emission aligns with the dust detected by JCMT SCUBA continuum observations at $\lambda = 850\ \mu m$. Two peaks of the dust continuum well corresponds to the CS peaks (labelled as A and J on the right of Figure 7.2), meaning that the CS emission is indeed tracing the densest regions in the molecular cloud. Figure 7.3 illustrates

the dust continuum emission at $\lambda = 3.1\ \mu m$ with two resolutions. From the left of this figure, it shows that there is no detectable dust emission associated with BD + 40° 4124 and V1686 Cyg, but dust emission is detected centered on the V1318 binary, which is consistent with the CS emission. This suggests that the most massive stars in the cluster evolve and reveal themselves quickly, and dominate the cloud disruption.

7.2.2 BD + 46° 3471

The BD46 system includes the Herbig A0 star, BD + 46° 3471, and the B0 star, BD + 46° 3474. Ch. 4 has shown that there is a group of young stars centered on the HAeBe, BD + 46° 3471.

Figure 7.4 illustrates the velocity-integrated CS emission with two resolutions. The low resolution (on the left) and high resolution (on the right) emphasize the overall dense gas distribution and peak emission, respectively. Like the BD40 cluster, the dense gas is also away from the most massive star in this system, BD + 46° 3471, and a cavity with a size $\sim$ 0.15 pc radius has been constructed centered on BD + 46° 3471. The size of this outflow cavity is similar to that seen around MWC 1080. Again, this is also a region where the most massive star in this cluster, despite being just an A star with a few $M_{\odot}$, dominates the natal cloud destruction, and this is the region where the gas is dispersing.

In addition, unlike the MWC 1080 system showing a biconical outflow cavity, the cavity around BD + 46° 3471 is near circularly symmetric, without considering any projection effects. This suggests that either the bipolar outflow is face-on, or that the system is actually older than the MWC 1080 so that the biconical structure has been erased. Low-resolution single-dish data (Fuente et al. 2002) classifies BD + 46° 3471 and MWC 1080 with the same evolutionary stage. However, the latter is not surprising as BD + 46° 3471 is much less massive (thus, less powerful) than MWC 1080, therefore BD + 46° 3471 may have taken more time than MWC 1080 to construct a cavity with similar sizes.

The dense gas traced by CS emission reveals three separated portions: (A) the north-west portion, which is the brightest; (B) the north-east portion; and (C) the south portion. The dense gas is most likely the leftover gas which still preserves the initial cloud condition, or the swept-up gas which has been accumulated and physically influenced by the BD + 46° 3471 outflow.

7.2.3 NGC 7129

The NGC 7129 reflection nebula contains three Herbig B stars, BD + 65° 1637, LkHα 234, and BD + 65° 1638. This is a system that should be similar to the BD40 cluster but more massive.

Figure 7.5 plots the velocity-integrated CS emission in this system. The CS peak emission is centered right on the Herbig B2 star, LkHα 234, which suggests this region is where the youngest stars are forming. The CS emission reveals a $\sim$ 0.4 pc long ridge with a PA $\sim$ 36°. Unlike the BD40 system where three HAeBes are forming closely, the CS emission around LkHα 234 is comparably isolated within $\sim$ 0.3 pc radius area. In addition, as the CS peak is still centered on LkHα 234, it suggests that LkHα 234 is a less evolved HAeBe than any other HAeBes discussed above.

7.2.4 Z CMa

Z CMa is a close (< 100 AU) binary including a optically bright FU Orionis star and a Herbig B0e star.

Figure 7.6 plots the velocity-integrated CS map with two resolutions. The low-resolution map on the left shows that there is an elongated dense gas centered nearly on Z CMa with an extent of $\sim$ 0.25 pc × 0.1 pc and a PA $\sim$ 45 °. However, from the high-resolution map on the right, two CS peaks are actually located $\sim$ 0.02 pc south-east and south-west almost equally from Z CMa, respectively, which has not been seen in previous observations. No previously identified sources are associated with these two peaks. However, there might be newly collapsing protostars hidden within.

In addition, based on the CS channel maps, there is no obvious velocity gradient or dispersion between different parts of the gas. This suggests that the dense gas traced by CS emission is not outflowing gas but dense material around this system.

7.2.5 HD 200775

HD 200775 is a Herbig B3 star with an age of 8 Myr and is surrounding by a large biconical outflow cavity with a size $\sim$ 1.5 pc × 0.8 pc has been constructed (Fuente et al. 2002, 1998b). Within the cavity, the gas is mainly atomic, and molecular gas with multi-shell structures, HI filaments, and bow shock regions have been observed (Fuente et al. 1998b). It is also suggested that the outflow

is currently at its late evolutionary stage probably driven by isotopic winds instead of a bipolar outflow.

Figure 7.7 illustrates the velocity-integrated CS map of this system and shows that there is a big CS clump located $\sim$ 0.1 pc north-east from HD 200775. This dense clump traced by CS emission is located close to the interface between an HI filament and the edge of ^{13}CO wall (Fuente et al. 1998b). This suggests the this BIMA observation catches the dense material on the cavity wall, while the atomic filament probes the area where molecular gas has been excavated by previous outflow activities.

7.3 The BD40 Cluster– a Case of Colliding Cloud Triggering the Star Formation

The BD40 cluster is one of the most interesting systems among my sample. This is a cluster with especially high star-forming efficiency, including multiple HAeBe stars forming closely, surrounding by numbers of low-mass stars. Hillenbrand et al. (1995b) suggests that star formation in this cluster was triggered by an external event based on morphological arguments. However, this cluster is actually isolated from any possible external source capable of inducing star formation, such as nearby expanding HII shells or OB associations. Therefore, previous studies have not yet concluded any mechanisms responsible for this external event triggering the star formation in this system.

By investigating the gas kinematics with BIMA's high spectral resolution observations ($\sim$ 0.3 km/s per channel), it can now be concluded that the highly efficient star formation in this cluster is actually due to cloud-cloud collision. This is based on the existence of systematic velocity gradients seen in the dense gas traced by CS emission.

In this cluster, there are 16 CS clumps identified, labelled in Figure 7.2. Masses of these clumps range from $\sim$ 0.1 to 2 $M_\odot$, indeed capable of forming single low-mass cluster members. The masses are estimated using the LVG model (see its description in Ch. 5). Moreover, spectra of these clumps are extracted and fitted with gaussian functions in order to obtain parameters, such as the peak flux, the peak velocity, and the linewidth of each clump. With fitted parameters, Figure

7.8 plots the relation between the position offset (from the image pointing center) and the peak velocity of each clump. This figure shows different velocity gradients between clumps on the south (clump P, O, N, C, E, A, F, and B), and clumps on the north (clump G, H, I, J, K, and L), with different linear correlations.

The most compelling explanation to the existence of two different systematic velocity trends is that there are two components in this cloud. The linear velocity gradient is probably due to the rotation of each cloud component. In fact, the Spitzer image toward this system (Figure 4.1) has also shown two dust components with different directions connecting on the BD40 cluster. Likewise, Figure 7.8 shows that these two gas components collide at the region where clump A, F, B, and G are. This is also the area where youngest stars are forming. Therefore, the kinematical evidence of two clouds implies that the northern cloud collided with the southern cloud, that accounts for the high star formation efficiency in this area.

The majority of this section, along with Ch. 7.2.1, was published as "Colliding Clouds: The Star Formation Trigger of the Stellar Cluster around BD +40 4124", Looney et al. 2006, ApJ, 642, 330.

7.4 Clumps– Star-Forming Building Blocks for Low-Mass Cluster Members

As mentioned in Ch. 5, clumps are commonly observed in molecular clouds. They are density enhancements in the clouds, and can provide enough material to form stars within. With BIMA's resolution and interferometric ability, clumps capable of forming single low-mass stars in the cluster can be identified and further examined. In this section, I identify clumps from the dense gas around BD+46° 3471, LkHα 234, and Z CMa. The BD40 cluster is excluded because it is a system triggered by an external event, and the HD 200775 system is much more evolved and complicated than others. Therefore, I only study clumps from these three clusters, which are young enough to have stars forming and old enough to have shown any influences from HAeBes. Again, the identified clumps can be treated as star-forming building blocks for low-mass cluster members. Therefore, it is the main thrust of this section to examine the physical conditions of these clumps, such as their masses,

Table 7.1. Physical Parameters of Identified Clumps

Cluster	N[a]	Area (pc^2)	Size (pc)	M_{LTE} ($M_\odot$)	M_{VIR} ($M_\odot$)	Linewidth (km/s)	α[b]
BD + 46° 3471	14	~0.05	0.008 - 0.030	0.1 - 0.4	1.4 - 6.2	0.8 - 1.7	2.2±0.21
LkHα 234	4	~0.01	0.012 - 0.015	1.3 - 5.2	6.4 - 25.4	1.8 - 3.8	-
Z CMa	17	~0.05	0.007 - 0.021	0.8 - 5.0	0.5 - 4.0	0.6 - 1.7	1.67±0.55

[a]Total numbers of clumps within the area

[b]$\rho \sim r^{-\alpha}$

the mass densities, and the non-thermal contributions. I will also compare them with those clumps in the MWC 1080 system (Ch. 5).

I use the same methods in Ch. 5 to (1) identify clumps from the CS velocity-integrated maps, (2) obtain the equivalent sizes of clumps, (3) fit gaussians to their spectra for their peak fluxes, peak velocities, and linewidths, and (4) derive their LTE and virial masses. Ch. 5 has shown that the average opacity of clumps in clusters like the MWC 1080 system is small and the LTE mass and mass based on the LVG model are similar, therefore I use the LTE assumption to derive clump masses. Table 7.1 lists the derived parameter ranges in these systems.

7.4.1 Clump Density

Figure 7.9 plots the average mass density (LTE mass / size^3) vs. size of identified clumps. This shows that most clumps in all clusters, except for those around BD + 46° 3471, have similar mass density and mass range. These clumps present typical sites where low-mass cluster members may form within. Clumps around BD + 46° 3471 are less massive and less dense than others. This is not surprising, as BD + 46° 3471 is the least-massive HAeBe and most evolved (based on the morphology argument) than the other three.

Moreover, I further investigate the density profile of these clumps. I directly estimate it from their LTE masses and sizes (Figure 7.10), as described in Ch. 5. Figure 7.10 plots the clump size vs. LTE mass for identified clumps. Again, as mentioned in Ch. 5, I simply assume all clumps in each cluster have the same density profile with $\rho(r) \sim r^{-\alpha}$, followed by obtaining linear relations

between these parameters via least-square fittings,

$$logM_{LTE}(M_{\odot}) = (0.80 \pm 0.21) logR_{eq}(pc) + (0.83 \pm 0.40), \quad (7.1)$$

for the BD + 46° 3471 cluster, and

$$logM_{LTE}(M_{\odot}) = (1.33 \pm 0.55) logR_{eq}(pc) + (2.68 \pm 1.03), \quad (7.2)$$

for the Z CMa cluster, where R_{eq} is the equivalent clump size. Therefore, the α value of these two systems are 2.2±0.21 and 1.67±0.55 for BD+46° 3471 and Z CMa, respectively. This result suggests that the identified clumps in these two systems are approximately under isothermal conditions, which have density profile of $\rho(r) \sim r^{-2}$. This result is also consistent with clumps in the MWC 1080 cluster (Ch. 5). I did not estimate the α value for the LkHα 234 cluster, as it has too few clumps to be fitted.

7.4.2 Nonthermal Contribution within Clumps

The presence of turbulence has been suggested in typical star-forming cores (Mac Low & Klessen 2004). My studies from the MWC 1080 cluster (Ch. 5) further shows that a larger amount of turbulence is also seen in low-mass star-forming cores in the cluster than those formed in isolation. Thus, it is suggested that low-mass stars in the cluster tend to be formed in more turbulent cores than those in isolation, which is also explained as the impact from the massive star in the cluster. In this section, in order to confirm whether this result is actually commonly seen in intermediate-mass clusters, I also extract spectra of identified clumps and examine their nonthermal contribution based on their velocity dispersion (Figure 7.11).

Figure 7.11 plots the relations between the linewidths of clumps and clump sizes (a) and LTE masses (b). This figure shows that all three clusters, along with the MWC 1080 cluster in Ch. 5, show comparable amount of turbulence. In addition, like those clumps around MWC 1080, clumps in the BD + 46° 3471, LkHα 234, and Z CMa clusters also generally have larger velocity dispersion, thus more turbulent, than thermal motion with a temperature of 20 K. In fact, most of them are even more turbulent, compared to the initial turbulence seen in massive cores (Caselli &

Myers 1995). This suggests that low-mass cluster members indeed generally form in a much more turbulent environment than isolated star formation.

Moreover, as also seen in Ch. 5, there is no obvious trend between the mass and linewidth of clumps in each cluster (Figure 7.11(b)), suggesting that there is a common external source that inputs the extra turbulence to each clump from the initial turbulence– impact from the massive star in the cluster, such as outflows or winds. This also implies that the nonthermal motion in the cluster is dominated by the massive star, instead of individual forming low-mass stars embedded in identified clumps.

7.4.3 LTE Mass vs. Virial Mass

Based on Figure 7.10, I have shown that all clumps approximately have isothermal density profile, $\rho(r) \sim r^{-2}$. This is actually consistent with protostellar collapsing models (e.g., Tassis & Mouschovias 2005). However, it does not necessarily mean that all identified clumps are collapsing. In order to distinguish whether they are star-forming collapsing cores or starless cores, I further investigate their virial conditions. Again, as all clumps have $\rho(r) \sim r^{-2}$ density profile, I simply use the Equation (5.5) to derive the virial masses for identified clumps, assuming they are all isothermal spheres. A range of clump's virial mass is listed in Table 7.1.

Figure 7.12 compares the clump LTE and virial masses. Clumps in the BD+46° 3471 and LkHα 234 system show a much larger virial masses, compared to LTE masses; while they are comparable for clumps around Z CMa. Clumps around MWC 1080 also show comparable masses between the LTE and virial mass. This indicates that the Z CMa cluster is a system similar to the MWC 1080 cluster, which has also been suggested based on their similar dense gas morphologies and the fact that they are both Herbig B0 stars with similar ages. Therefore, like clumps in the MWC 1080 cluster, clumps around Z CMa a re also dense, turbulent, and probably collapsing protostellar cores.

On the other hand, clumps in LkHα are actually more massive compared to those in other system and very close to the HAeBe LkHα 234. Therefore, large virial mass in this system might indicate that there is significant external gas pressure contribution outside the clumps in this area, as seen for massive star-forming cores (Saito et al. 2006).

However, unlike the LkHα 234 cluster, large virial mass in the BD + 46° 3471 system actually suggests that they are gravitationally unbound and starless, instead of protostellar cores, as they do not have enough masses to overcome the large turbulence (Figure 7.11) and initiate the core collapsing for star formation. As BD+46° 3471 is a HAeBe with less mass and also more evolved than other sample, it is not surprising that the clump masses in this system are lower than others. This system presents an example how massive star or HAeBe impacts the surrounding star formation– the nonthermal input from the HAeBe prevents low-mass cores from future star formation.

7.5 Conclusion

In this chapter and Ch. 5, I have presented BIMA dense gas maps toward the intermediate-mass clusters around six HAeBes, BD40, LkHα 234 (in NGC 7129 system), BD+46° 3471, HD 200775, Z CMa, and MWC 1080. I have also studied the physical conditions of clumps around these HAeBes. Here I summarize some results.

7.5.1 Evolutionary Stage Comparison between Sampled Clusters

Hillenbrand et al. (1992) characterizes the sampled HAeBes with the same evolutionary stage, based on their near-infrared emission. They show that these HAeBes are at the stage analogic to classic T-Tauri stars. However, my results actually reveal discrepancy in the dense gas environment around these HAeBes, including the gas morphologies and clump physical conditions. In fact, single-dish millimeter observations (Fuente et al. 2002) have also suggested that the gas dispersal in the sampled clusters is different and can be classified as three types (Fuente Type I-III). Here, I separate my sampled clusters by Fuente Types and discuss their clump properties.

- **LkHα 234: Fuente Type I.** Fuente et al. (2002) shows that Type I HAeBes are still immersed in the center of a dense clump. My results show that in this case (such as the LkHα 234 system), massive clumps with at least a few $M_{\odot}$, instead of low-mass clumps, are forming very close to the cluster core. These clumps are experiencing high turbulence and external gas pressure, as most mass in the cluster is still condensed in the cluster core area.

- **MWC 1080 and Z CMa: Fuente Type II.** Fuente et al. (2002) shows that gas around Type II HAeBes has started to be dispersed, so that they are not in the center of the dense clump. Z CMa is classified as a Fuente Type I star. However, it is actually a Type II star, based on high-resolution BIMA results. My results show that in this case, an outflow cavity with a size of a few 0.1 pc radius has been constructed. Dense gas in this case is most likely swept-up gas, whose physical conditions have been modified by inputs from the HAeBe, such as outflows or winds. In addition, clumps around HAeBes are gravitationally bound, likely collapsing star-forming cores, and are actually denser and more turbulent than those forming isolated stars.

- **BD + 46° 3471: Fuente Type II.** The BD + 46° 3471 system is also classified as Type II, based on its gas morphology. However, physical conditions of clumps suggest that this is a more evolved system than MWC 1080 and Z CMa. The main difference between them is that stars are still forming within the clumps around MWC 1080 and Z CMa, while star formation in the BD + 46° 3471 has been terminated: clumps around BD + 46° 3471 are likely just starless cores. This is because the left-over gas around BD + 46° 3471 has been dispersed, having little mass to overcome the nonthermal motion in the cluster.

- **HD 200775: Fuente Type III.** Fuente et al. (2002) shows that in this case, gas has been mostly dispersed and the HAeBe is located in a large cavity. Therefore, the CS emission in my observations just trace some dense region on the cavity wall.

7.5.2 Summary

In summary, the physical conditions of those clumps cabable of forming single low-mass stars in clusters have been presented. It is also confirmed that low-mass stars indeed form in more turbulent cores than isolated low-mass star formation, as suggested in Ch. 5. Moreover, this chapter also suggests that the nonthermal contribution input by the massive star can accelerate the termination of future star formation in the cluster when the cloud is dispersing. This provides further evidence of the massive star's influence.

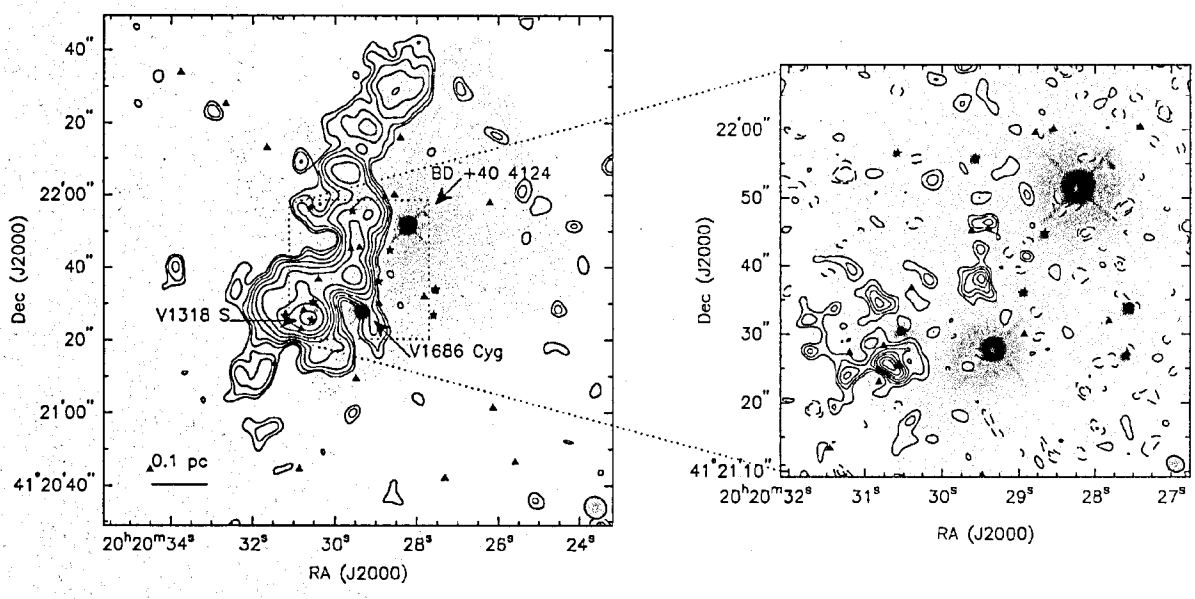

Figure 7.1 CS (2-1) emission toward the BD+40° 4124 young cluster overlaid on a smaller adaptive optic H-Band image (Davies et al. 2001). Both CS maps are made from the same data with different weighting. On the left is the low resolution image emphasizing the large-scale structures. The noise is 0.2 Jy/beam km/s. The contours are logarithmically spaced (increment $\sqrt{2}$) from 2 to 64 times the noise. The negative contours, presumably from resolved out large-scale emission, are not shown to simplify the image. The beam, shown in the lower-right corner, is $6\farcs42 \times 5\farcs83$ with a PA of 40°. The dotted box indicates the zoomed field of the high resolution map (right). The high resolution image emphasizes the smaller-scale clumps of material traced by CS. The noise is 0.29 Jy/beam km/s. The contours are linearly spaced from 2 to 7 (positive and negative) times the noise. The beam, shown in the lower-right corner, is $2\farcs76 \times 2\farcs27$ with a PA of 62°. The symbols indicate IR sources: the star symbols indicate IR sources with optical counterparts, and the triangle symbols indicate IR sources without an optical counterpart (presumably more embedded objects, thus younger).

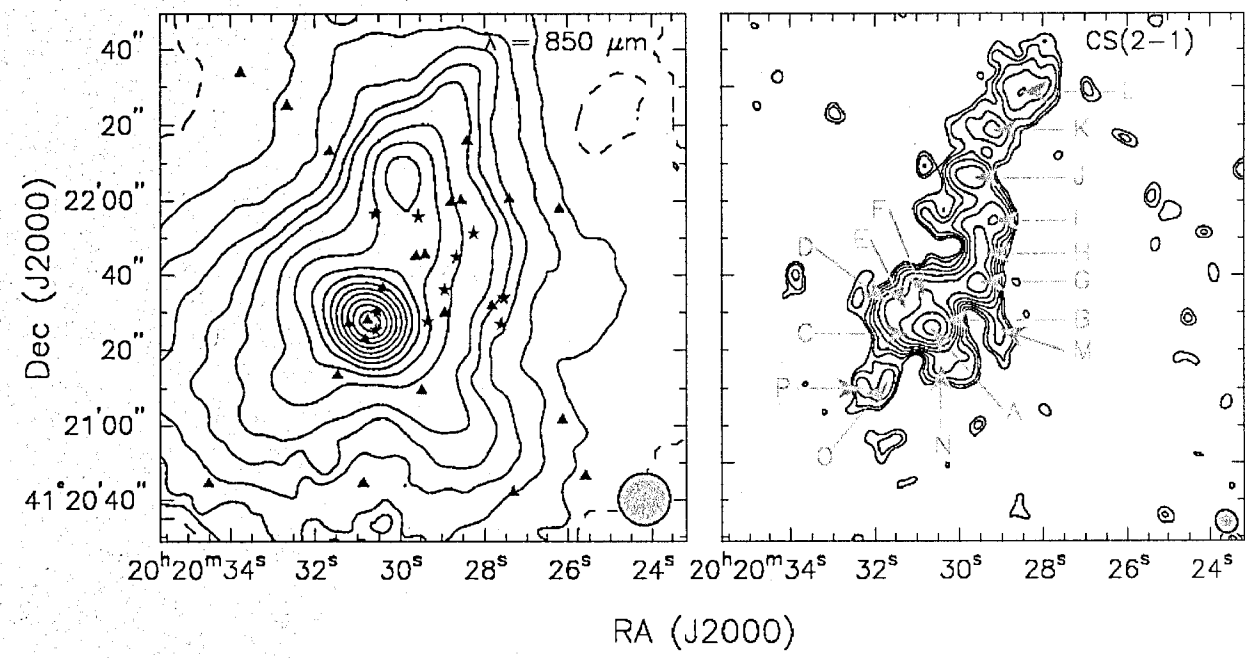

Figure 7.2 $\lambda = 850$ μm continuum emission toward the BD + 40° 4124 young cluster in the left panel is archival SCUBA observations. The contours are in steps of 2 from 2 to 10 and in steps of 5 from 10 to 60 times the noise of 0.045 Jy/beam. The beam shown at the lower right is 14.7″. The symbols are the same as in Figure 7.1. The right panel is the low resolution CS emission from Figure 7.1 with the 16 clumps labeled.

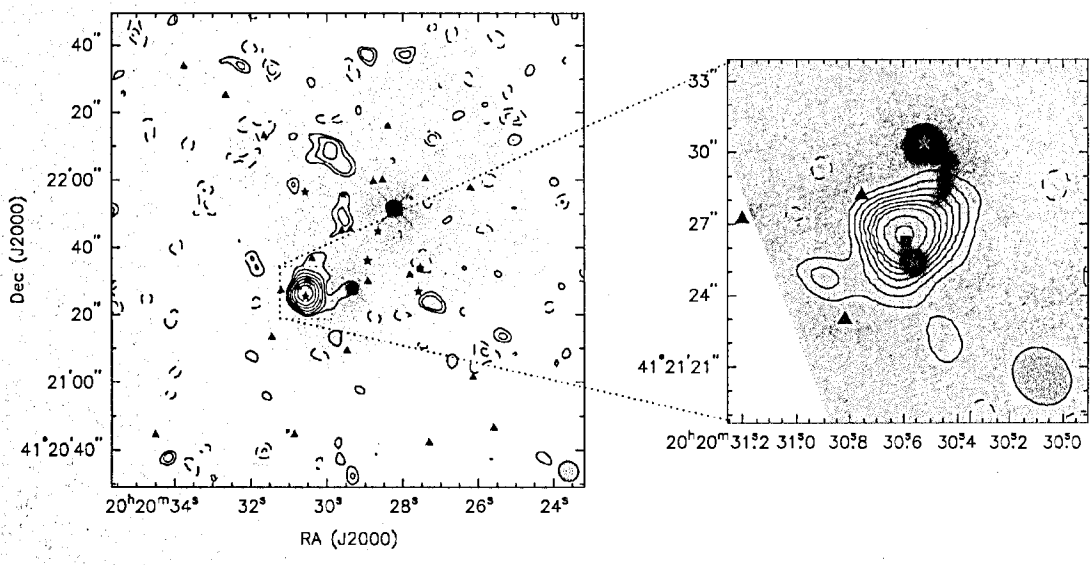

Figure 7.3 $\lambda = 3.1$ mm continuum emission toward the BD + 40° 4124 young cluster overlaid on a smaller adaptive optic H-Band image (Davies et al. 2001). Both maps are made from the same data with different weighting. On the left is the low resolution image emphasizing the large-scale structures. The noise is 1.6 mJy/beam. The contours are logarithmically spaced (increment $\sqrt{2}$) from 2 to 32 times the noise; negative values are indicated by dashed contours. The beam, shown in the lower-right corner, is $6\farcs12 \times 5\farcs68$ with a PA of 45°. The dotted box indicates the zoomed field of the high resolution map (right). The high resolution image emphasizes the compact emission. The noise is 1.8 mJy/beam. The contours are linearly spaced from 2 to 20 (positive and negative in steps of two) times the noise. The beam, shown in the lower-right corner, is $2\farcs67 \times 2\farcs24$ with a PA of 52°. The triangle and star symbols are the same as in Figure 7.1, but the solid square indicates the position of the VLBA water maser source. Inset is a zoom of the V1318 region using a different colormap on the H-band data to emphasize the diffuse structure. Note that the H Band spur off the northern component is a real scattered light feature.

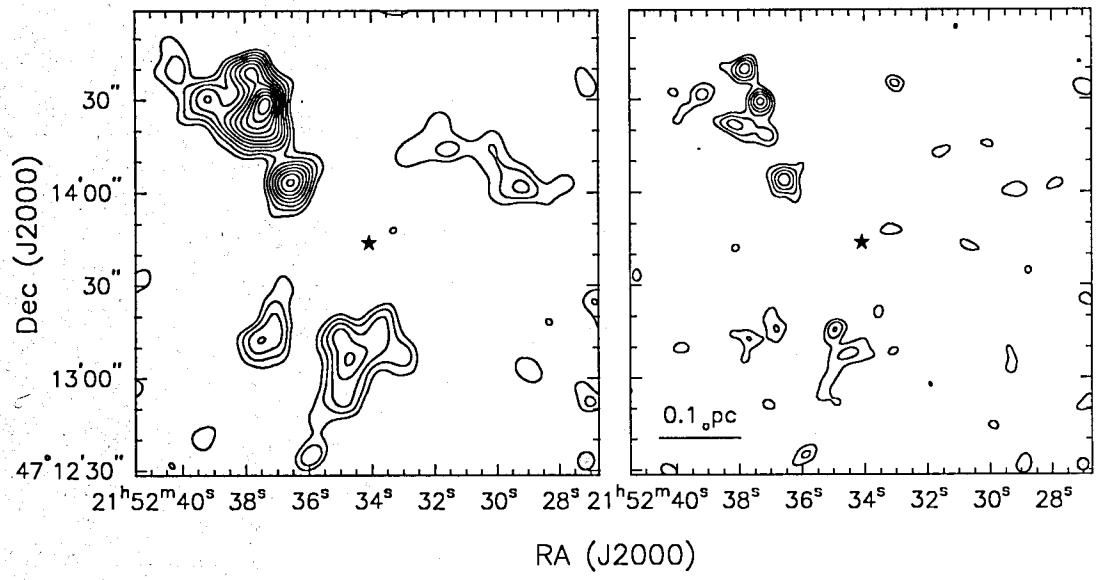

Figure 7.4 CS(2-1) emission toward the star, BD + 46° 3471 with two resolutions. Left: The noise is 0.07 Jy/beam km/s. The contours are linearly spaced from 2 to 13 times of noise. The beam is 10.″14 × 9.″24 with a PA of -22°. Right: The noise is 0.094 Jy/beam km/s. The contours are linearly spaced from 2 to 7 times of noise. The beam is 6.″66 × 6.″42 with a PA of -3°. Negative contours, mainly from resolved out large-scale emission, are not shown here in order to simplify the image. The position of BD + 46° 3471 is plotted as a filled star symbol.

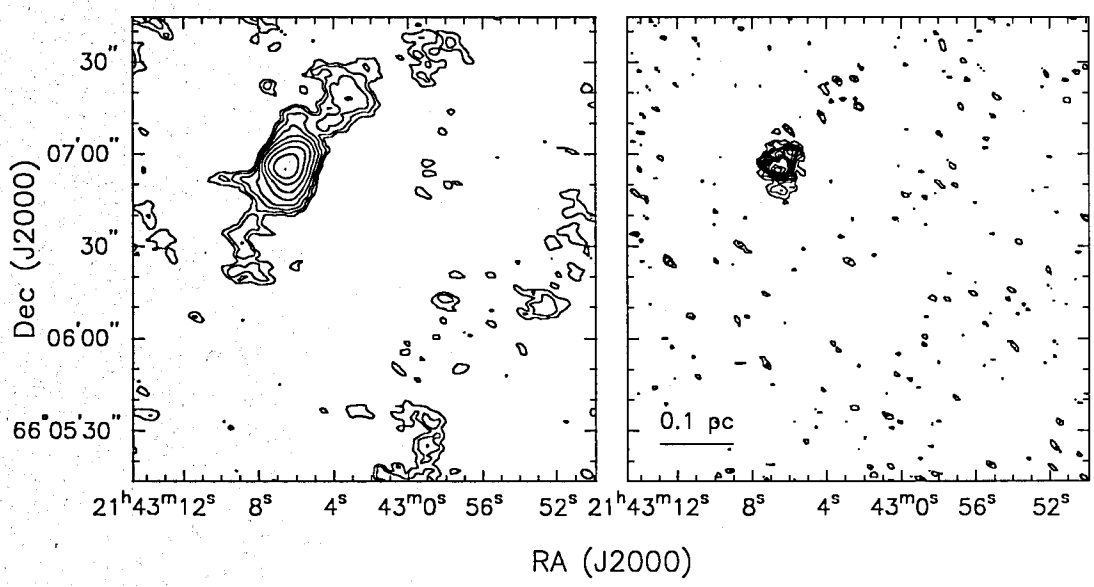

Figure 7.5 CS(2-1) emission toward the NGC 7129 system with two resolutions. The star, LkHα 234 is right at the peak of the dense core on north-east. Left: The noise is 0.133 Jy/beam km/s. The contours are logarithmically spaced from 2 to 60 times of noise. The beam is $6\farcs88 \times 4\farcs67$ with a PA of 65°. Right: The noise is 0.21 Jy/beam km/s. The contours are linearly from 2 to 16 times of noise. The beam is $4\farcs08 \times 2\farcs35$ with a PA of 61°. Negative contours, mainly from resolved out large-scale emission, are not shown here in order to simplify the image.

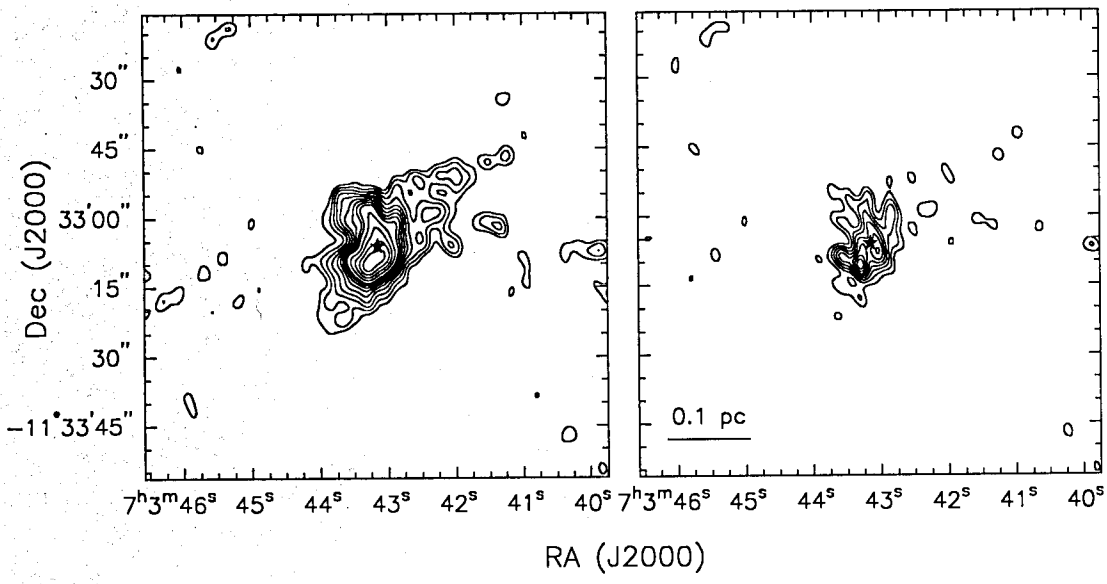

Figure 7.6 CS(2-1) emission toward the Z CMa system with two resolutions. Left: The noise is 0.182 Jy/beam km/s. The contours are linearly spaced from 2 to 20 times of noise. The beam is $6\farcs16 \times 4\farcs13$ with a PA of 7°. Right: The noise is 0.26 Jy/beam km/s. The contours are linearly spaced from 2 to 10 times of noise. The beam is $5\farcs07 \times 2\farcs95$ with a PA of 15°. Negative contours, mainly from resolved out large-scale emission, are not shown here in order to simplify the image. The position of Z CMa is plotted as a filled star symbol.

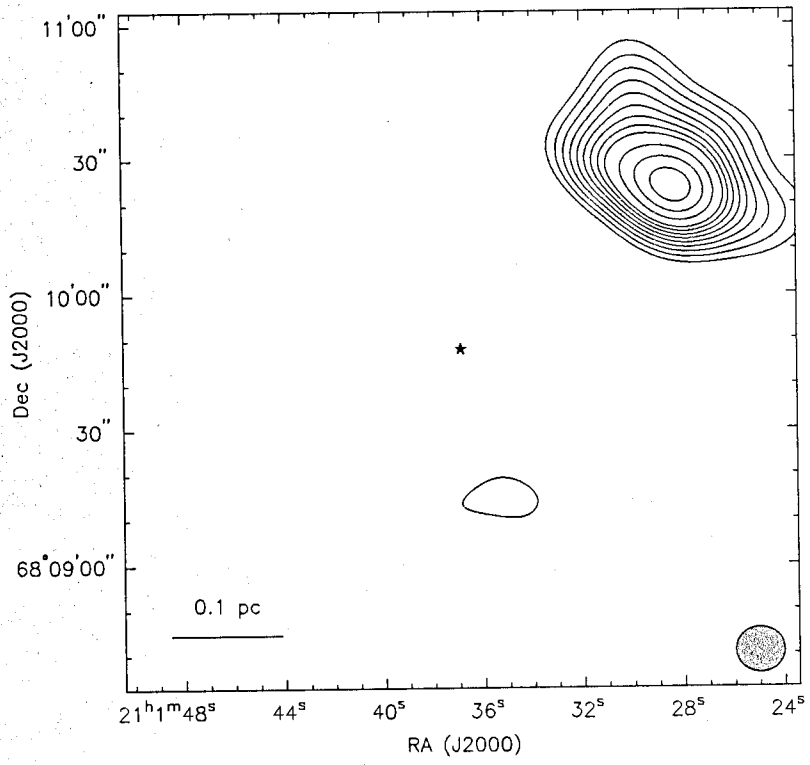

Figure 7.7 CS(2-1) emission toward the HD 200775 system. The noise is 0.18 Jy/beam km/s. The contours are linearly spaced from 2 to 18 times of noise. The beam is $18\farcs67 \times 17\farcs27$ with a PA of 86°. Negative contours, mainly from resolved out large-scale emission, are not shown here in order to simplify the image. The position of HD 200775 is plotted as a filled star symbol.

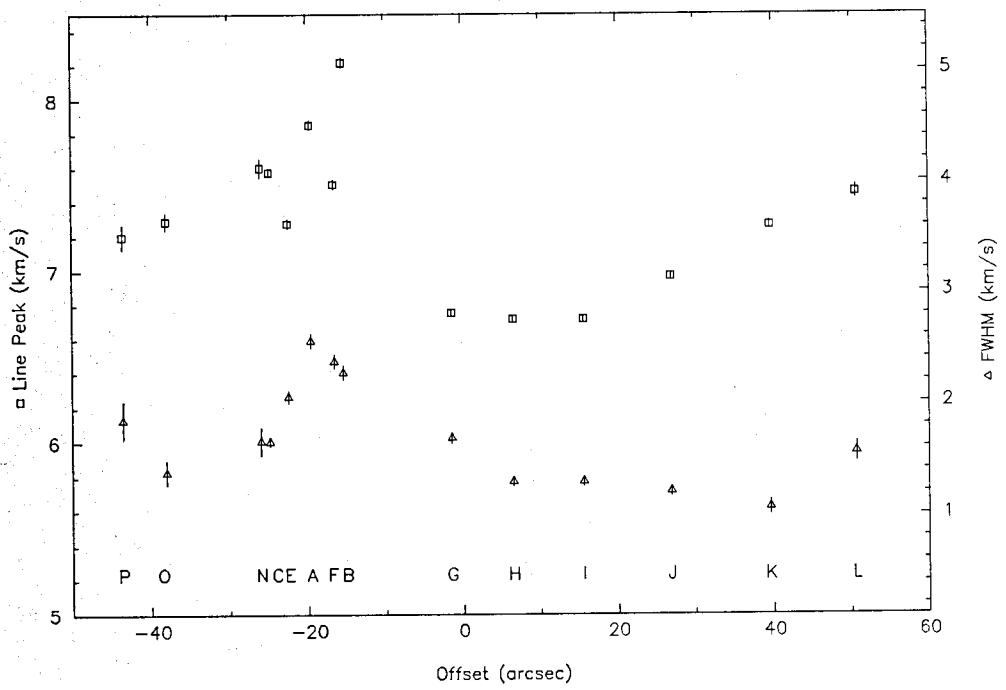

Figure 7.8 Comparison of the low resolution spectra peak velocity and linewidth with offset from the pointing center (near peak G) in arcseconds. Clumps D and M are not plotted as their Gaussian fits are not acceptable. The square symbols are the line center velocities of the remaining 14 best fit Gaussians, as indicated by the left-hand axis. The triangle symbols are the corresponding FWHM of the best fit Gaussians, as indicated by the right-hand axis. The error bars are the Gaussian fit error on the parameters. This assumes that the spectra are well defined as Gaussians. At the bottom, each clump is labeled with the associated letter.

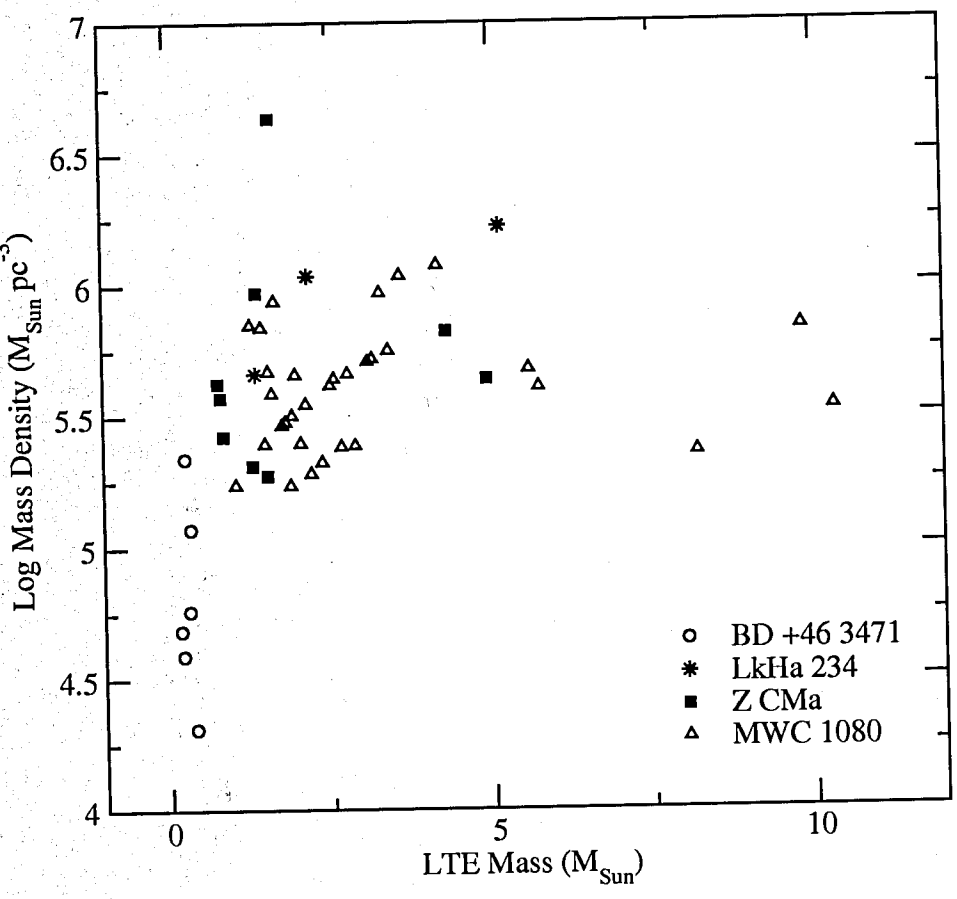

Figure 7.9 Mass density vs. LTE mass of identified clumps around BD + 46° 3471, LkHα 234, Z CMa, and MWC 1080. Except for the BD + 46° 3471 cluster, these clumps with a mass range from 1 - 10 $M_{\odot}$ have comparable mass density. The BD + 46° 3471 cluster contains lower-mass and less dense clumps, compared to the other three clusters. This is not surprising, as BD + 46° 3471 is the lowest-mass and most evolved HAeBe among these four clusters.

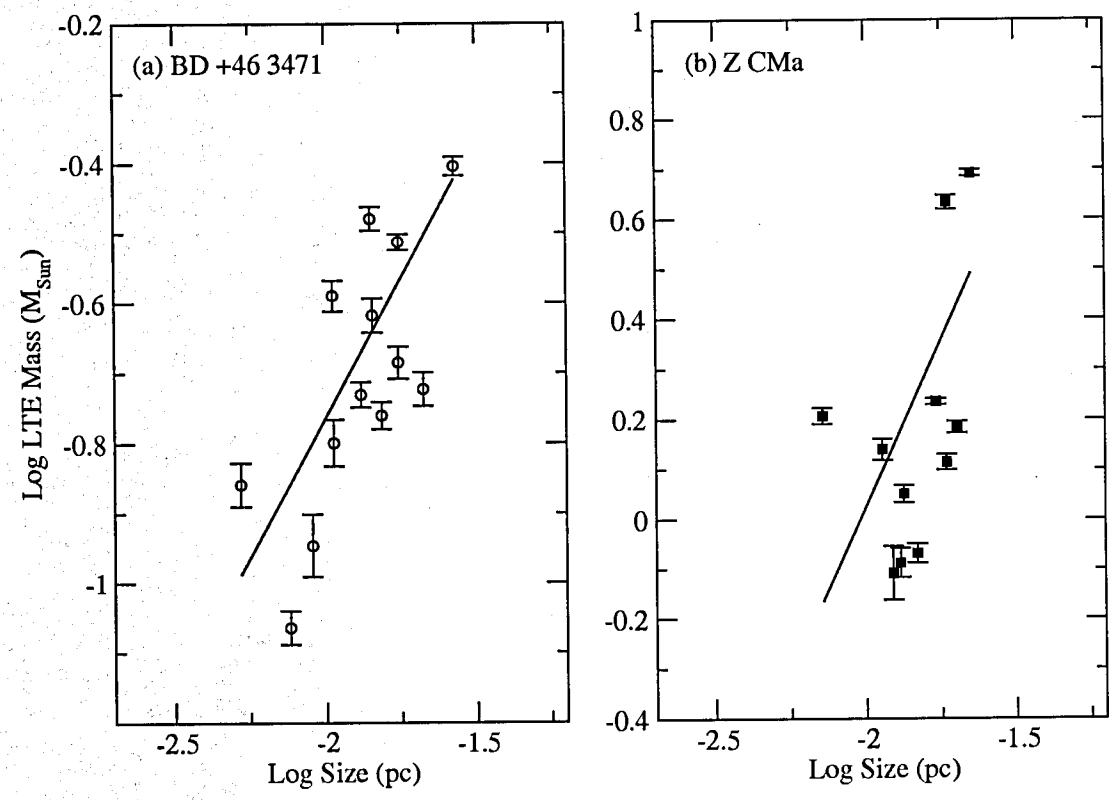

Figure 7.10 LTE mass vs. size for clumps around BD + 46° 3471 and Z CMa. Linear relations are fitted to obtain the density profiles of clumps in both systems. The solid lines plot the Equation (7.1) and (7.2) for BD + 46° 3471 and Z CMa, respectively.

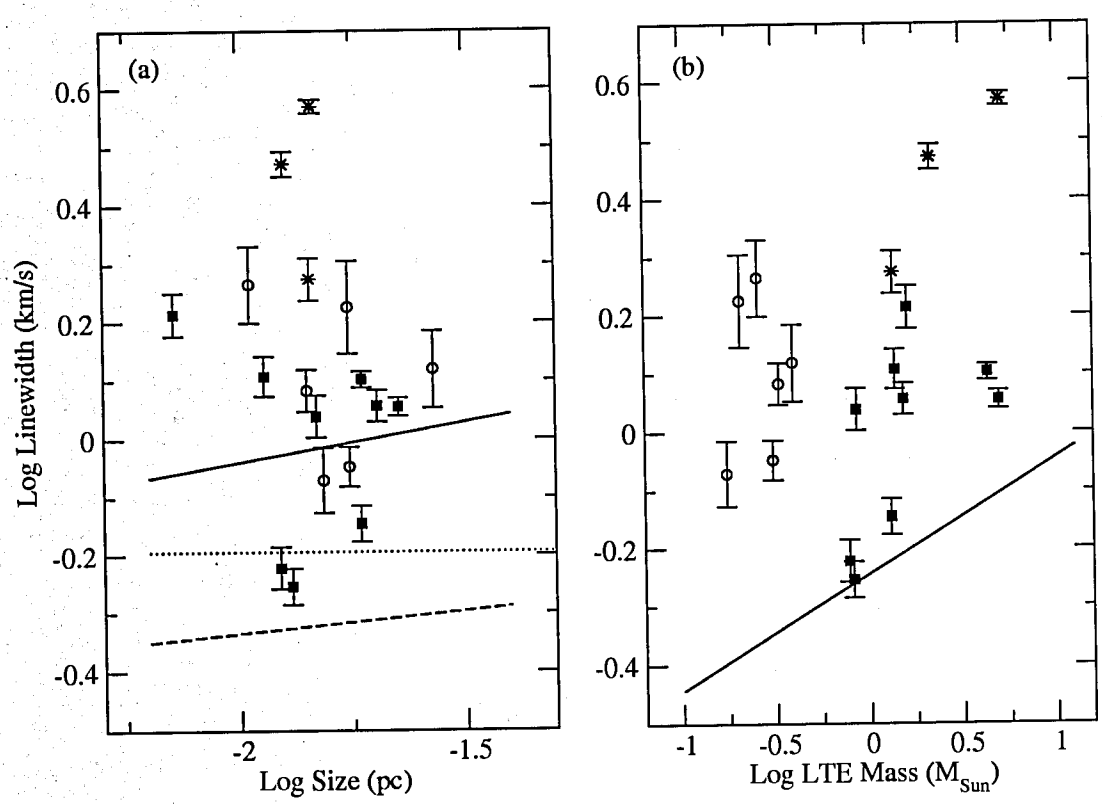

Figure 7.11 Linewidth vs. size and LTE mass for clumps around BD + 46° 3471, LkHα 234, and Z CMa are plotted. Labels are the same as in Figure 7.9. The solid and dashed lines in (a) indicate the massive cores and low-mass cores (Caselli & Myers 1995), respectively, and the dotted line is the thermal motion at temperature of 20 K. The solid line in (b) indicates the mass-linewidth relation from Larson (1981).

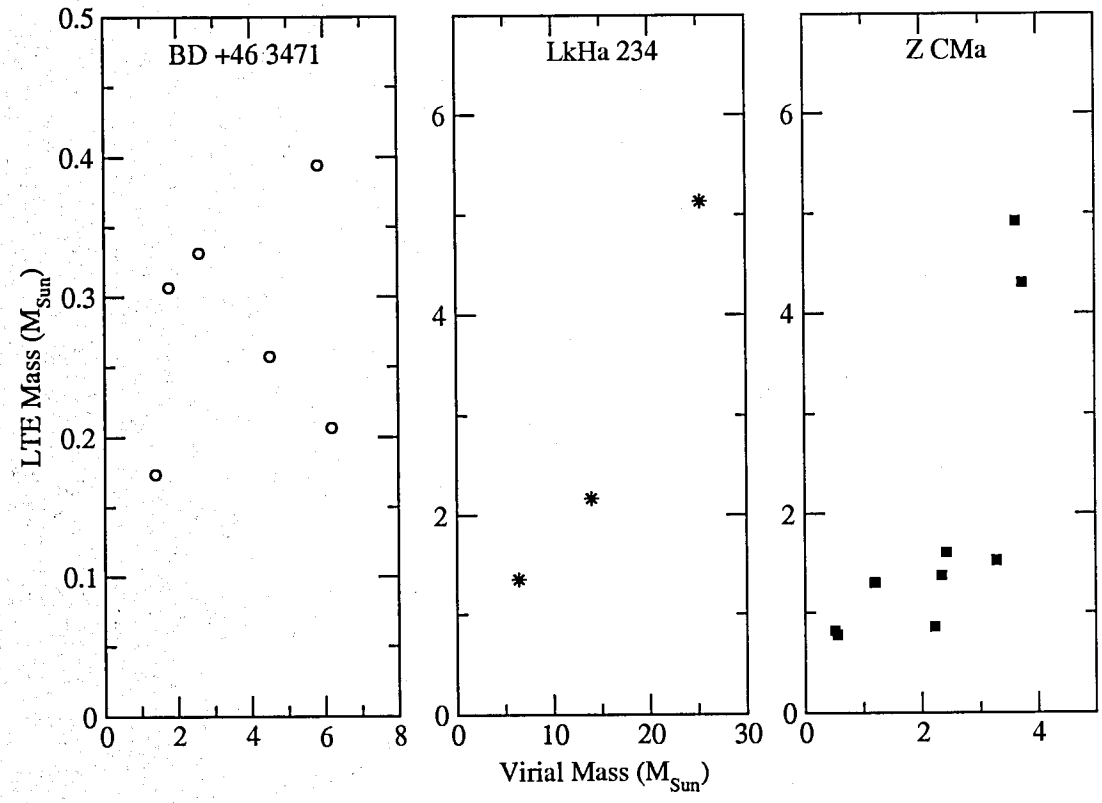

Figure 7.12 Comparison between the LTE and virial mass for clumps around BD + 46° 3471, LkHα 234, and Z CMa.

Chapter 8

Conclusions

In this thesis, I have carried out infrared and millimeter observations of young stars, dense gas, and dust continuum in embedded intermediate-mass stellar clusters around Herbig Ae/Be stars (3 - 20 $M_{\odot}$).

With wide-field infrared observations, I first established a scheme using the color-color diagram with J to M bands to identify young stars. This scheme is especially useful when the observations at wavelengths longer than M band are not reliable. For example, they are often much less sensitive than those at shorter wavelengths, or easily confused with diffuse dust nebulosity or PAH emission. In addition, I also obtained YSO loci, where the intrinsic colors of low-mass disk objects with a wild range of circumstellar parameters are distributed. In fact, the YSO loci can be an extension of CTTs loci (Meyer et al. 1997) to be used to estimate stellar extinction from color-color diagrams.

With this scheme, I identified the large-scale young stellar population around the vicinity where the sampled clusters form. Wide-field near- to mid-infrared observations show that there are indeed groups of young stars (10 - 50) around HAeBes within 1 pc radius. In addition, there are also young stellar populations throughout the whole field outside the sampled clusters, some of which are distributed and some of which are clumped. It appears that clusters around HAeBes are substructures of the large young population within the same molecular cloud. However, young stars in clusters around HAeBes have generally larger SED slopes compared to those outside, suggesting that the young stars in clusters are probably younger than the distributed systems. This might imply that there is usually a higher and more continuous star-forming rate in clusters, that the formation of clusters initiates later, or that low-mass stars in clusters form slower than those outside at the scale of these observations. Moreover, there is no obvious trend between the SED slopes and the distance to the HAeBes for those young stars within the clusters. This indicates that the clustering of young stars dominates over the effect of massive stars on the low-mass young stars

at the scale of this study. Nevertheless, these infrared observations have revealed the large-scale young stellar environment where the sampled clusters form, which is important as the first step to understand the sampled systems.

However, the resolution of these wide-field infrared observations are not good enough to probe the cluster members distributed deep within the cluster core, where the impact from the HAeBe is the most significant. Therefore, in order to examine the effects of the massive star on its low-mass siblings, I also obtained the high-resolution adaptive-optics near-infrared observations toward one of the most massive cluster systems in my sample, the MWC 1080 cluster. With these observations, stars within $\sim$0.3 pc around this 20 $M_{\odot}$ Herbig Be star are revealed. Again, this region is where stars are experiencing the most impact from the central massive star in the cluster. These observations show that 85% of identified stars are located within the biconical outflow cavity. Infrared colors of these stars within the cavity suggest that they are not just less extincted, but also contain less circumstellar material than those outside. This presents evidence of the massive star's influence– the strong gas dispersal from MWC 1080 does not just reveal these stars in the cavity but also helps clean-out their circumstellar material, thus accelerates the apparent evolution of their formation.

Furthermore, along with the wide-field infrared observations, my results also provide examples of how many low-mass stars can accompany an intermediate-mass or massive star from as close as < 0.1 pc to a few pc range. This is significant, as it implies that distant massive stars might not be isolated, even if they appear to be isolated, but instead they might be surrounded with tens of low-mass stars, whose properties should be considered.

Not only stars, the physical conditions in the cluster-forming cloud are also modified by the most massive star in the cluster. Indeed, millimeter observations probing the dense molecular gas and dust continuum toward the MWC 1080 cluster have shown a domination of MWC 1080 on the cloud, including the cloud dispersal and the gas kinematics. In particular, dense clumps in this system show larger mass density and velocity dispersion than isolated low-mass star-forming cores, suggesting low-mass cluster members tend to be formed in the denser and more turbulent cores, compared to isolated low-mass star-forming cores, due to inputs from MWC 1080. Nevertheless, this provides further evidence of the massive star's influence– outflows or winds from the massive star increase the nonthermal motion in the natal cloud so that low-mass cluster members need to

accumulate more masses to initiate the formation.

In addition, in order to obtain a more comprehensive view on the physical conditions of dense clumps capable of forming individual low-mass cluster members, I have also acquired millimeter observations toward a few more clusters around HAeBes. These observations suggest that all clumps approximately have a similar mass density profile of a isothermal sphere, $\rho(r) \sim r^{-2}$, which could be collapsing protostellar cores (Tassis & Mouschovias 2005) if clumps are also gravitationally bound. In addition, it is also suggested that sampled clusters (around early A to early B HAeBes) contain similar amount of turbulence, which is comparable to or even more than the turbulence seen in massive star-forming cores, which are also generally much larger than the turbulence in isolated low-mass star-forming cores. Moreover, these observations also show that the nonthermal contribution inputed by the massive star accelerates the termination of future star formation in the cluster when the cloud is dispersing.

In summary, in this thesis, I have shown that clusters indeed provide a different environment for low-mass star formation, especially kinematically. I have also suggested some effects, particularly disruptive, from intermediate-mass to massive stars on both their low-mass siblings and natal clouds.

In the future, I plan to study low-mass star-forming environment in younger and more massive clusters. I have actually obtained CARMA observations probing dense gas toward four protoclusters around bright IRAS sources, which are systems still at the earliest stage of massive star formation. With these observations, I will be able to identify clumps and examine their kinematics. By comparing with this thesis, I am most interested in investigating the evolution of clumpiness of cluster-forming cloud and the initial turbulence. This will be important to understand the initial conditions of low-mass star-forming environment.

References

Ábrahám, P., Leinert, C., Burkert, A., Henning, T., & Lemke, D. 2000, A&A, 354, 965

Adams, F. C., Proszkow, E. M., Fatuzzo, M., & Myers, P. C. 2006, ApJ, 641, 504

Allen, L. E. 1995, Ph.D. Thesis

Allen, L. E., Calvet, N., D'Alessio, P., Merin, B., Hartmann, L., Megeath, S. T., Gutermuth, R. A., Muzerolle, J., Pipher, J. L., Myers, P. C., & Fazio, G. G. 2004, ApJS, 154, 363

Allen, L. E., Megeath, S. T., Gutermuth, R. A., Myers, P. C., Wolk, S., Adams, F. C., Muzerolle, J., Young, Y., & Pipher, J. L. 2006, astro-ph/0603096

Arce, H. G., Shepherd, D., Gueth, F., Lee, C.-F., Bachiller, R., Rosen, A., & Beuther, H. 2007, Protostars and Planets V, 245

Benjamin, R. A., Churchwell, E., Babler, B. L., Bania, T. M., Clemens, D. P., Cohen, M., Dickey, J. M., Indebetouw, R., Jackson, J. M., Kobulnicky, H. A., Lazarian, A., Marston, A. P., Mathis, J. S., Meade, M. R., Seager, S., Stolovy, S. R., Watson, C., Whitney, B. A., Wolff, M. J., & Wolfire, M. G. 2003, PASP, 115, 953

Bessell, M. S. & Brett, J. M. 1988, PASP, 100, 1134

Canto, J., Rodriguez, L. F., Calvet, N., & Levreault, R. M. 1984, ApJ, 282, 631

Caselli, P. & Myers, P. C. 1995, ApJ, 446, 665

Caswell, J. L. & Haynes, R. F. 1987, A&A, 171, 261

Cohen, M. & Kuhi, L. V. 1979, ApJS, 41, 743

Covino, E., Terranegra, L., Vittone, A. A., & Russo, G. 1984, AJ, 89, 1868

D'Antona, F. & Mazzitelli, I. 1994, ApJS, 90, 467

Davies, R. I., Tecza, M., Looney, L. W., Eisenhauer, F., Tacconi-Garman, L. E., Thatte, N., Ott, T., Rabien, S., Hippler, S., & Kasper, M. 2001, ApJ, 552, 692

di Francesco, J., Evans, II, N. J., Caselli, P., Myers, P. C., Shirley, Y., Aikawa, Y., & Tafalla, M. 2007, in Protostars and Planets V, ed. B. Reipurth, D. Jewitt, & K. Keil, 17–32

Drew, J. E., Busfield, G., Hoare, M. G., Murdoch, K. A., Nixon, C. A., & Oudmaijer, R. D. 1997, MNRAS, 286, 538

Edwards, S. & Snell, R. L. 1983, ApJ, 270, 605

Evans, II, N. J., Allen, L. E., Blake, G. A., Boogert, A. C. A., Bourke, T., Harvey, P. M., Kessler, J. E., Koerner, D. W., Lee, C. W., Mundy, L. G., Myers, P. C., Padgett, D. L., Pontoppidan, K., Sargent, A. I., Stapelfeldt, K. R., van Dishoeck, E. F., Young, C. H., & Young, K. E. 2003, PASP, 115, 965

Evans, II, N. J., Balkum, S., Levreault, R. M., Hartmann, L., & Kenyon, S. 1994, ApJ, 424, 793

Fazio, G. G., Hora, J. L., Allen, L. E., Ashby, M. L. N., Barmby, P., Deutsch, L. K., Huang, J.-S., Kleiner, S., Marengo, M., Megeath, S. T., Melnick, G. J., Pahre, M. A., Patten, B. M., Polizotti, J., Smith, H. A., Taylor, R. S., Wang, Z., Willner, S. P., Hoffmann, W. F., Pipher, J. L., Forrest, W. J., McMurty, C. W., McCreight, C. R., McKelvey, M. E., McMurray, R. E., Koch, D. G., Moseley, S. H., Arendt, R. G., Mentzell, J. E., Marx, C. T., Losch, P., Mayman, P., Eichhorn, W., Krebs, D., Jhabvala, M., Gezari, D. Y., Fixsen, D. J., Flores, J., Shakoorzadeh, K., Jungo, R., Hakun, C., Workman, L., Karpati, G., Kichak, R., Whitley, R., Mann, S., Tollestrup, E. V., Eisenhardt, P., Stern, D., Gorjian, V., Bhattacharya, B., Carey, S., Nelson, B. O., Glaccum, W. J., Lacy, M., Lowrance, P. J., Laine, S., Reach, W. T., Stauffer, J. A., Surace, J. A., Wilson, G., Wright, E. L., Hoffman, A., Domingo, G., & Cohen, M. 2004, ApJS, 154, 10

Finkenzeller, U. & Mundt, R. 1984, A&AS, 55, 109

Friedel, D. N. 2005, PhD thesis, University of Illinois at Urbana-Champaign, United States – Illinois

Fuente, A., Martin-Pintado, J., Bachiller, R., Neri, R., & Palla, F. 1998a, A&A, 334, 253

Fuente, A., Martın-Pintado, J., Bachiller, R., Rodrıguez-Franco, A., & Palla, F. 2002, A&A, 387, 977

Fuente, A., Martin-Pintado, J., Rodriguez-Franco, A., & Moriarty-Schieven, G. D. 1998b, A&A, 339, 575

Fuente, A., Neri, R., Martín-Pintado, J., Bachiller, R., Rodríguez-Franco, A., & Palla, F. 2001, A&A, 366, 873

Goldreich, P. & Kwan, J. 1974, ApJ, 189, 441

Goldsmith, P. F. & Langer, W. D. 1999, ApJ, 517, 209

Gomez, M., Hartmann, L., Kenyon, S. J., & Hewett, R. 1993, AJ, 105, 1927

Graves, J. E., Northcott, M. J., Roddier, F. J., Roddier, C. A., & Close, L. M. 1998, in Presented at the Society of Photo-Optical Instrumentation Engineers (SPIE) Conference, Vol. 3353, Proc. SPIE Vol. 3353, p. 34-43, Adaptive Optical System Technologies, Domenico Bonaccini; Robert K. Tyson; Eds., ed. D. Bonaccini & R. K. Tyson, 34–43

Gutermuth, R. A., Megeath, S. T., Muzerolle, J., Allen, L. E., Pipher, J. L., Myers, P. C., & Fazio, G. G. 2004, ApJS, 154, 374

Habart, E., Testi, L., Natta, A., & Vanzi, L. 2003, A&A, 400, 575

Hartmann, L., Kenyon, S. J., Hewett, R., Edwards, S., Strom, K. M., Strom, S. E., & Stauffer, J. R. 1989, ApJ, 338, 1001

Hartmann, L., Megeath, S. T., Allen, L., Luhman, K., Calvet, N., D'Alessio, P., Franco-Hernandez, R., & Fazio, G. 2005, ApJ, 629, 881

Harvey, P. M., Chapman, N., Lai, S.-P., Evans, II, N. J., Allen, L. E., Jørgensen, J. K., Mundy, L. G., Huard, T. L., Porras, A., Cieza, L., Myers, P. C., Merín, B., van Dishoeck, E. F., Young, K. E., Spiesman, W., Blake, G. A., Koerner, D. W., Padgett, D. L., Sargent, A. I., & Stapelfeldt, K. R. 2006, ApJ, 644, 307

Harvey, P. M., Wilking, B. A., & Joy, M. 1984, ApJ, 278, 156

Herbig, G. H. 1960, ApJS, 4, 337

Herbig, G. H. & Dahm, S. E. 2002, AJ, 123, 304

Hillenbrand, L. A., Meyer, M. R., Strom, S. E., & Skrutskie, M. F. 1995a, AJ, 109, 280

—. 1995b, AJ, 109, 280

Hillenbrand, L. A., Strom, S. E., Vrba, F. J., & Keene, J. 1992, ApJ, 397, 613

Indebetouw, R., Mathis, J. S., Babler, B. L., Meade, M. R., Watson, C., Whitney, B. A., Wolff, M. J., Wolfire, M. G., Cohen, M., Bania, T. M., Benjamin, R. A., Clemens, D. P., Dickey, J. M., Jackson, J. M., Kobulnicky, H. A., Marston, A. P., Mercer, E. P., Stauffer, J. R., Stolovy, S. R., & Churchwell, E. 2005, ApJ, 619, 931

Koresko, C. D., Beckwith, S. V. W., Ghez, A. M., Matthews, K., & Neugebauer, G. 1991, AJ, 102, 2073

Lada, C. J. & Lada, E. A. 2003, ARA&A, 41, 57

Lada, C. J., Muench, A. A., Luhman, K. L., Allen, L., Hartmann, L., Megeath, T., Myers, P., Fazio, G., Wood, K., Muzerolle, J., Rieke, G., Siegler, N., & Young, E. 2006, AJ, 131, 1574

Larson, R. B. 1979, MNRAS, 186, 479

—. 1981, MNRAS, 194, 809

—. 1995, MNRAS, 272, 213

Levreault, R. M. 1988, ApJS, 67, 283

Looney, L. W., Mundy, L. G., & Welch, W. J. 2000, ApJ, 529, 477

—. 2003, ApJ, 592, 255

Looney, L. W., Wang, S., Hamidouche, M., Safier, P. N., & Klein, R. 2006a, ApJ, 642, 330

—. 2006b, ApJ, 642, 330

Luhman, K. L., Stauffer, J. R., Muench, A. A., Rieke, G. H., Lada, E. A., Bouvier, J., & Lada, C. J. 2003, ApJ, 593, 1093

Lynds, B. T. 1962, ApJS, 7, 1

Mac Low, M.-M. & Klessen, R. S. 2004, Reviews of Modern Physics, 76, 125

Megeath, S. T., Allen, L. E., Gutermuth, R. A., Pipher, J. L., Myers, P. C., Calvet, N., Hartmann, L., Muzerolle, J., & Fazio, G. G. 2004, ApJS, 154, 367

Meyer, M. R., Adams, F. C., Hillenbrand, L. A., Carpenter, J. M., & Larson, R. B. 2000, Protostars and Planets IV, 121

Meyer, M. R., Calvet, N., & Hillenbrand, L. A. 1997, AJ, 114, 288

Miao, Y., Mehringer, D. M., Kuan, Y.-J., & Snyder, L. E. 1995, ApJ, 445, L59

Morris, P. W., Noriega-Crespo, A., Marleau, F. R., Teplitz, H. I., Uchida, K. I., & Armus, L. 2004, ApJS, 154, 339

Muench, A. A., Lada, E. A., Lada, C. J., & Alves, J. 2002, ApJ, 573, 366

Muench, A. A., Lada, E. A., Lada, C. J., Elston, R. J., Alves, J. F., Horrobin, M., Huard, T. H., Levine, J. L., Raines, S. N., & Román-Zúñiga, C. 2003, AJ, 125, 2029

Nakajima, Y., Tachihara, K., Hanawa, T., & Nakano, M. 1998, ApJ, 497, 721

Palla, F., Testi, L., Hunter, T. R., Taylor, G. B., Prusti, T., Felli, M., Natta, A., & Stanga, R. M. 1995, A&A, 293, 521

Pfalzner, S., Olczak, C., & Eckart, A. 2006, astro-ph/0604018

Poetzel, R., Mundt, R., & Ray, T. P. 1992, A&A, 262, 229

Polomski, E. F., Woodward, C. E., Holmes, E. K., Butner, H. M., Lynch, D. K., Russell, R. W., Sitko, M. L., Wooden, D. H., Telesco, C. M., & Piña, R. 2005, AJ, 129, 1035

Pudritz, R. E. 2002, Science, 295, 68

Rho, J., Reach, W. T., Lefloch, B., & Fazio, G. G. 2006, ApJ, 643, 965

Ridge, N. A., Wilson, T. L., Megeath, S. T., Allen, L. E., & Myers, P. C. 2003, AJ, 126, 286

Rieke, G. H. & Lebofsky, M. J. 1985, ApJ, 288, 618

Robitaille, T. P., Whitney, B. A., Indebetouw, R., & Wood, K. 2007, ApJS, 169, 328

Robitaille, T. P., Whitney, B. A., Indebetouw, R., Wood, K., & Denzmore, P. 2006, ApJS, 167, 256

Rohlfs, K. & Wilson, T. L. 2000, Tools of radio astronomy (Tools of radio astronomy / K. Rohlfs, T.L. Wilson. New York : Springer, 2000. (Astronomy and astrophysics library,ISSN0941-7834))

Saito, H., Saito, M., Moriguchi, Y., & Fukui, Y. 2006, PASJ, 58, 343

Sault, R. J., Teuben, P. J., & Wright, M. C. H. 1995, in Astronomical Society of the Pacific Conference Series, Vol. 77, Astronomical Data Analysis Software and Systems IV, ed. R. A. Shaw, H. E. Payne, & J. J. E. Hayes, 433–+

Shu, F. H. 1977, ApJ, 214, 488

Simon, M. 1997, ApJ, 482, L81+

Skrutskie, M. F., Cutri, R. M., Stiening, R., Weinberg, M. D., Schneider, S., Carpenter, J. M., Beichman, C., Capps, R., Chester, T., Elias, J., Huchra, J., Liebert, J., Lonsdale, C., Monet, D. G., Price, S., Seitzer, P., Jarrett, T., Kirkpatrick, J. D., Gizis, J. E., Howard, E., Evans, T., Fowler, J., Fullmer, L., Hurt, R., Light, R., Kopan, E. L., Marsh, K. A., McCallon, H. L., Tam, R., Van Dyk, S., & Wheelock, S. 2006, AJ, 131, 1163

Störzer, H. & Hollenbach, D. 1999, ApJ, 515, 669

Strom, K. M., Strom, S. E., & Merrill, K. M. 1993, ApJ, 412, 233

Surace, J. A., Shupe, D. L., Fang, F., Lonsdale, C. J., Gonzalez-Solares, E., Baddedge, T., Frayer, D., Evans, T., Jarrett, T., Padgett, D. L., Castro, S., Masci, F., Domingue, D., Fox, M., Rowan-Robinson, M., Perez-Fournon, I., Olivier, S., Poletta, M., Berta, S., Rodighiero, G., Vaccari, M., Stacey, G., Hatziminaoglou, E., Farrah, D., Siana, B., Smith, H. E., Franceschini, A., Owen, F., Pierre, M., Xu, C., Afonso-Luis, A., Davoodi, P., Dole, H., Pozzi, F., Salaman, M., & Waddington, I. 2004, VizieR Online Data Catalog, 2255, 0

Tassis, K. & Mouschovias, T. C. 2005, ApJ, 618, 769

Testi, L., Palla, F., & Natta, A. 1998, A&AS, 133, 81

Tobin, J. J., Looney, L. W., Mundy, L. G., Kwon, W., & Hamidouche, M. 2007, ApJ, 659, 1404

van den Ancker, M. E., Blondel, P. F. C., Tjin A Djie, H. R. E., Grankin, K. N., Ezhkova, O. V., Shevchenko, V. S., Guenther, E., & Acke, B. 2004, MNRAS, 349, 1516

Velázquez, P. F. & Rodríguez, L. F. 2001, Revista Mexicana de Astronomia y Astrofisica, 37, 261

Vicente, S. M. & Alves, J. 2005, A&A, 441, 195

Wang, S. & Looney, L. W. 2007, in prep.

Wang, S., Looney, L. W., Brandner, W., & Close, L. M. 2008, ApJ, 673, 315

Waters, L. B. F. M. & Waelkens, C. 1998, ARA&A, 36, 233

Welch, W. J., Thornton, D. D., Plambeck, R. L., Wright, M. C. H., Lugten, J., Urry, L., Fleming, M., Hoffman, W., Hudson, J., Lum, W. T., Forster, J. . R., Thatte, N., Zhang, X., Zivanovic, S., Snyder, L., Crutcher, R., Lo, K. Y., Wakker, B., Stupar, M., Sault, R., Miao, Y., Rao, R., Wan, K., Dickel, H. R., Blitz, L., Vogel, S. N., Mundy, L., Erickson, W., Teuben, P. J., Morgan, J., Helfer, T., Looney, L., de Gues, E., Grossman, A., Howe, J. E., Pound, M., & Regan, M. 1996, PASP, 108, 93

Wilking, B. A., Lada, C. J., & Young, E. T. 1989, ApJ, 340, 823

Williams, J. P., de Geus, E. J., & Blitz, L. 1994, ApJ, 428, 693

Wu, Y., Zhang, Q., Chen, H., Yang, C., Wei, Y., & Ho, P. T. P. 2005, AJ, 129, 330

Yoshida, S., Kogure, T., Nakano, M., Tatematsu, K., & Wiramihardja, S. D. 1991, PASJ, 43, 363

—. 1992, PASJ, 44, 77

Zinnecker, H. & Yorke, H. W. 2007, ArXiv e-prints, 707